UCLA
UCLA Electronic Theses and Dissertations

Title
Plastic Scintillators for Pulse Shape Discrimination of Particle Types in Radiation Detection

Permalink
https://escholarship.org/uc/item/9dq7f30t

Author
HAJAGOS, TIBOR JACOB

Publication Date
2017

Peer reviewed|Thesis/dissertation

UNIVERSITY OF CALIFORNIA

Los Angeles

Plastic Scintillators for Pulse Shape Discrimination of Particle Types in Radiation

Detection

A dissertation submitted in partial satisfaction

of the requirements for the degree

Doctor of Philosophy in Materials Science and Engineering

by

Tibor Jacob Hajagos

2017

ABSTRACT OF THE DISSERTATION

Plastic Scintillators for Pulse Shape Discrimination of Particle Types in Radiation
Detection

by

Tibor Jacob Hajagos

Doctor of Philosophy in Materials Science and Engineering

University of California, Los Angeles, 2017

Professor Qibing Pei, Chair

Organic scintillators have a long history in the field of radiation detection, dating back to
some of the earliest studies of organic photophysics and optoelectronic properties. In partic-
ular, plastics have come to dominate the commercial market for organic scintillators, due to
their low cost and ease of use and manufacturing, and more notably in spite of their poorer
performance in many metrics. While there has been decades of active research since their
inception, little progress has been made to improve upon the now well established compo-
sitions of commercial plastics, a notable exception being the recent development of plastic
scintillators capable of *pulse shape discrimination* (PSD) of n/γ radiation, which is of partic-
ular interest among governments and industry for the detection of illicit nuclear material and
weapons. In recent years, much attention has been paid towards the study of luminescent
organic materials, in particular due to the invention and widespread adoption of organic light
emitting diode (OLED) based electronic devices, and the knowledge and lessons that have
been fundamental to such fields have recently begun to be adopted by the organic scintilator
community. In this work, new approaches to the design of both plastic scintillator compo-
nents, and of the materials as a whole, are described, with particular emphasis paid towards
the design and synthesis of small molecule scintillating dyes that are specifically tailored to-
wards the development of PSD-capable plastic scintilators. In the first of these approaches,
the design and synthesis of a highly soluble and polymerizable derivative of 9,10-diphenylan-
thracene is described, and the properties of plastic scintilators fabricated from this dye when

copolymerized with poly(vinyl toluene) were investigated. This particular approach was used to demonstrate a proof-of-concept of PSD in highly loaded plastics stabilized through copolymerization of the primary dye, a strategy conceived to address the particular shortcomings of the current generation of PSD plastics. The second general approach investigated is the application of the phenomenon of *thermally activated delayed fluorescence* (TADF) — most notably a key innovation among the latest developments in OLED technologies — to the enhancement of the performance of organic sicntillators. Several key observations about the potential and efficacy of TADF dyes as novel organic scintillators were made, including a demonstration of the profound effects the the TADF phenomenon can have on scintillation properties. These findings suggest that it is quite possible that TADF dyes could eventually enable an entirely new generation of high performance organic scintillators, and PSD-capable plastics in particular.

The dissertation of Tibor Jacob Hajagos is approved.

Yu Huang

Michael E. Jung

Qibing Pei, Committee Chair

University of California, Los Angeles

2017

Table of Contents

List of Figures

List of Tables

xiv

ACKNOWLEDGMENTS

Vita

2004	High School Diploma, North Monterey County High School, Castroville, California.
2009	B.S. (Chemistry), UCLA, Los Angeles, California.
2009–2010	Associate Chemist, Medtronic Inc., Northridge, California.

Publications

T. J. Hajagos, D. Kishpaugh, Q. Pei, Pulse shape discrimination properties of plastic scintillators incorporating a rationally designed highly soluble and polymerizable derivative of 9,10-diphenylanthracene, Nuclear Instruments and Methods in Physics Research Section A: Accelerators, Spectrometers, Detectors and Associated Equipment 825 (2016) 40–50. (DOI: 10.1016/j.nima.2016.04.029)

T. J. Hajagos, E. Garcia, D. Kishpaugh, Q. Pei, Plastic scintillators based on thermally activated delayed fluorescence dyes, 2017, in preparation for publication.

CHAPTER 1

Introduction

1.1 Overview of Radiation Detection Challenges

The accurate detection, identification, and quantification of radiation is of principal importance for many fields, including nuclear power, national security, medical imaging, high-energy physics, and astronomical discovery, to name a few. In particular, plastic scintillator materials are presently in wide use for passive detection of nuclear materials, primarily in the radiation portal monitors and/or hand-held detectors that are employed to scan vehicles and/or cargo containers at borders or other ports of entry to the United States. However, conventional (i.e., unsensitized) plastic scintillators do not provide any useful spectroscopic capabilities, and as such they have no inherent ability to distinguish special nuclear material (fissile material such as ^{233}U, ^{235}U, and Pu-isotopes), which is of particular importance in terms of national security interests, from other sources of radiation, such as medical or commercially important isotopes, or naturally occurring background radiation. High resolution spectroscopic detectors can be used to augment the plastic-based detectors, but the analysis requires the use of expensive and cumbersome detectors, which additionally require specialized training and knowledge to operate. For special nuclear material detection in particular, there is also need for the sensitive detection and discrimination of neutron radiation from other sources or background that may be present. Careful measurement of the energies of fast neutrons can offer additional information and/or insight into the identity of the material under investigation, but traditional scintillating plastics alone do not offer any spectroscopic information during neutron detection. As such, the development of a new generation of plastic materials that would be capable overcoming many of these short comings has for

some time been an active area of research in the field of radiation detection. Reconciliation of these often oppositional requirements requires entirely new approaches to the design and materials synthesis of new scintillating plastics. Furthermore, widespread deployment of a wholly new generation of plastic material will require that its manufacturing cost does not greatly exceed that of current commercially available materials, so that the material can be used within very large volume detectors such as radiation portal monitors.

1.2   Scintillation Detector Fundamentals[1]

In the most basic sense, a scintillator is any material that is capable of converting some of the energy of a high energy particle that passes through it into low energy photons, typically in the ultraviolet to visible range. Because the scintillation photons need to be able to escape the material in order to be detected, a scintillating material will need to be a homogeneous, transparent solid that does not significantly absorb the emitted photons. A key performance metric of any scintillator is its *light yield*, which is defined as:

$$\text{Light Yield} = \frac{\text{\# of scintillation photons}}{\text{energy of particle (MeV)}} \tag{1.1}$$

The detection of a high energy particle will typically only produce $\sim 10^3$–10^5 photons per event, and as such a high sensitivity photodetector, most commonly a photomultiplier tube, is needed to detect the scintillation light and convert it into an electrical signal that can be further processed into useful information. As such, a scintillation detector is constructed by optically coupling a piece of the scintillating material to the entrance window of a photomultiplier tube, and enclosing both components within a light-tight housing. Additionally, the sides of the scintillator not in contact with the photomultiplier tube window are usually clad with a diffuse reflective material to maximize the number of photons (which are emitted in all directions randomly) that are able to reach the photomultiplier tube.

   Figure 1.1 illustrates the operational principals of a typical scintillation detector when it interacts with a high energy particle. After the scintillating material converts some of the high energy particle's energy to low energy photons, these photons will eventually reach
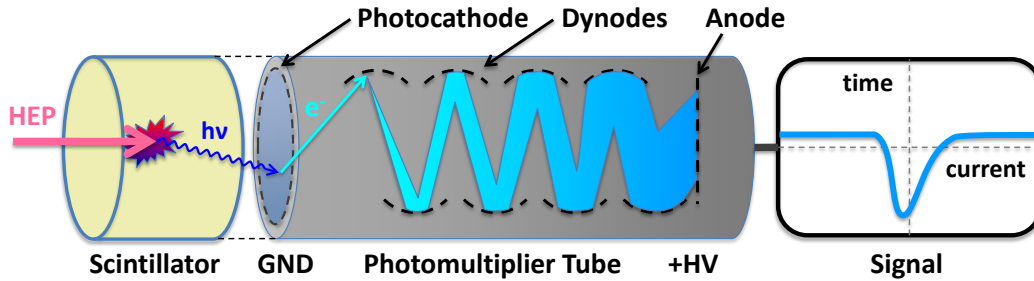
Figure 1.1: Exploded schematic overview of the operation principals of a typical scintillation detector.

the end window of the photomultiplier tube. Coated on the inside of the photomultiplier tube end window is photosensitive material that can absorb a photon and produce a free electron via the *photoelectric effect*, and this material is termed the *photocathode*. When a high voltage bias is applied between the photocathode and the anode at the opposite end of the tube, and successive intermediate voltages are applied at each dynode, the free electron produced at the photocathode will accelerate, first through a focusing grid (not shown in Figure 1.1) and hit the first dynode. Impact ionization due to the electron's kinetic energy will create additional free electrons, which will accelerate in a similar fashion to the next dynode. This process will continue down the dynode chain, with the number of electrons exponentially growing, until the electron cascade reaches the anode and can be conducted out of the tube to produce an electrical signal.

1.3   Materials for Scintillation Detectors[2]

Scintillating materials may be broadly grouped into organic and inorganic varieties. Inorganic scintillating materials tend to be composed of heavier elements, which makes them particularly suitable for detection and spectroscopy of γ-rays. Due to transparency requirements, the majority of inorganic scintillators are single crystalline, although there is a subcategory that consists of amorphous glasses. Of all the scintillating materials, inorganics tend to have the highest light yields and energy resolutions for γ-spectroscopy, but they are limited to small to medium detector volumes, on account of their high cost and the difficulty

3

of growing single crystals to relatively large diameters. Other challenges associated with inorganics is that many (in particular the halide salts) are hygroscopic and require hermetically sealed encapsulation to prevent rapid deterioration from atmospheric moisture. Thallium doped Sodium Iodide (Na(Tl)) is one of the most ubiquitous inorganic scintillators, and is widely considered as a benchmark for comparison not only for other scintillators but when comparing scintillation detectors for other detector technologies in general.

Organic scintillators primarily fall into three different subcategories, namely organic crystals, organic liquids, and plastic scintillators. Organic crystals are typically among the highest performers of all the organics, with the highest light yields. They can be grown from either solution or from the melt, however, they are very difficult to grow to sizes larger than a couple of inches. Moreover, they are quite fragile and difficult to machine and polish, and all of these factors have hindered wide-scale adoption other than for niche applications.

Liquid scintillators and plastic scintillators are in principle quite similar to one another, as they generally consist of an aromatic organic matrix, and one or more dissolved fluorescent dyes which enable light emission. Not surprisingly, the major difference between the two is that liquids use an aromatic solvent as the matrix, whereas plastics use an polymer containing aromatic functional groups. Both liquid and plastic scintillators can in principle be scaled to large volumes quite easily, but in practice, there are several factors that make large scale deployment of liquid scintillators problematic. These include flammability and toxicity of the aromatic solvents, and for the need to maintain strict oxygen-free conditions throughout the working lifetime of the detector. Plastics, on the other hand, are safe and non-toxic when fully cured, and oxygen-free conditions are only necessary during the curing stage. Of all the scintillating materials, plastics are generally the cheapest, easiest to machine, and easiest to scale to very large volumes, but their principal drawbacks are relatively low performance, and limited effective atomic number (effective-Z), which means they have low detection efficiencies for γ-rays and cannot provide any spectroscopic information about them, as will be discussed in Chapter 2 (which is also true for non-sensitized organics in general). Plastic scintillators, like other optical plastic materials, have been fabricated through various means, but by in large the most technologically significant of which for scintillators is the

4

solution casting method, which has the principle advantages of simplicity, scalability, and is a more viable option for plastic base materials like poly(vinyl toluene), which is the most commonly utilized matrix material in commercial plastic scintillators. Other aromatic plastics, like polystyrene have certain cost advantages (being that optical grade pellets are widely available and relatively cheap, unlike for poly(vinyl toluene)), and can be effectively processed through continuous processes like extrusion, but cannot match the performance of poly(vinyl toluene)-based scintillators.[3]

CHAPTER 2

Physics of Detector/Radiation Interactions[1]

2.1   Charged Particle Interactions

When a radiation or other high energy particle encounters the active material of a detector, the primary means through which energy is deposited within the active material is through ionization. For charged particles, such as fast electrons (β-rays), fast protons, α-particles, or heavier nuclei including fission fragments, electromagnetic interactions with the electrons and nuclei of the detector materials will result in direct ionization along the particle track. On the other hand, high energy neutral particles, such as photons (γ-rays) or fast neutrons, are unaffected by the charged electrons and nuclei of the detector material, and in addition to being far more penetrating, will tend to interact through the generation of additional high energy charged particles (Sections 2.2 and 2.3). Figure 2.1(a) depicts the main processes that can occur when a high-energy particle interacts within the detector material. Along the ionization track of a charged primary particle, electrons are scattered with sufficiently high energies (δ-rays) to enable further ionization away from the main track, to form secondary ionized regions known as spurs. If the volume of the active material is small in comparison to the penetration depth of the particle, there will be a high probability that the particle will exit the material without fully depositing its energy, but for larger volumes, continued scattering along the ionization track will eventually drain all its kinetic energy, and the particle will recombine with scattered ions to create a neutral atom.

A measure of the rate at which a charged particle loses energy in a material is known as the specific energy loss ($\frac{dE}{dx}$), which is a function of the the particle's energy. More precisely stated, it is the differential unit of energy lost as the particle moves a differential unit of
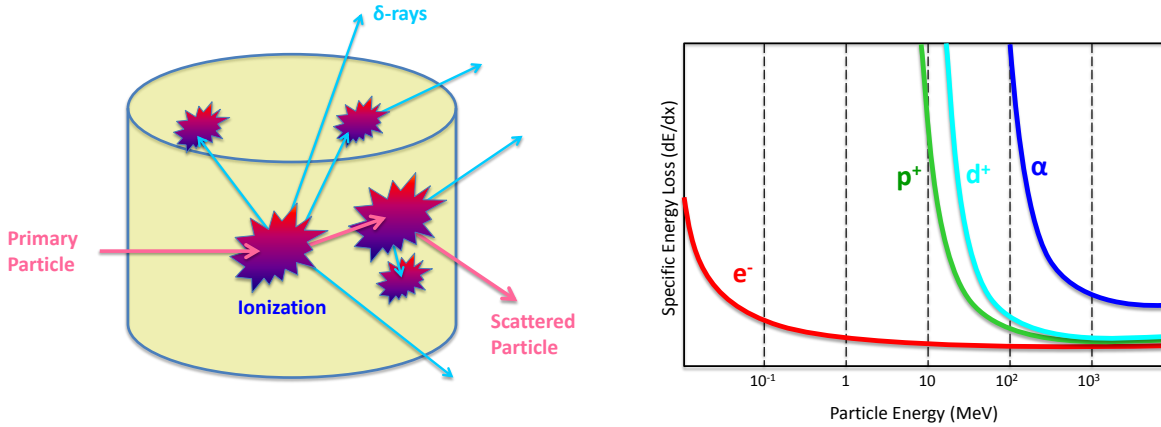
Figure 2.1: Left: Illustration of the various physical processes involved in interactions of high energy particles. Right: Schematic representation of the specific energy loss $\left(\frac{dE}{dx}\right)$ for various charged particles in an arbitrary material.

distance within the material. Figure 2.1(b) depicts how the values of specific energy loss increase with decreasing energy for various charged particles. Besides energy, the two other main factors controlling the magnitude of specific energy loss are the charge and mass of the particle. For a given unit of charge, a more massive particle will have a higher specific energy loss, as can be seen from the fact that for a given energy specific energy loss is increased going from a electron (e^-), to a proton (p^+), and in going from a proton to a deuteron (d^+). The highest specific energy loss shown in Figure 2.1(b) is that of an α-particle, which is both more massive and has a higher magnitude of charge than any of the other particles shown. Because specific energy loss is a spatial metric of the energy deposited by the particle, with increasing specific energy loss, the overall interaction is occurring within a smaller volume, leading to a higher ionization density.

2.2 γ-Ray Interactions

Despite a lack of net electrical charge, interactions of γ-rays with matter are still mediated via electromagentic forces, and for γ energies ≤1 MeV, interactions are principally with the electron cloud of the material. For detector materials, the two primary interactions that

7

(a) Photoelectric Effect   (b) Compton Scattering
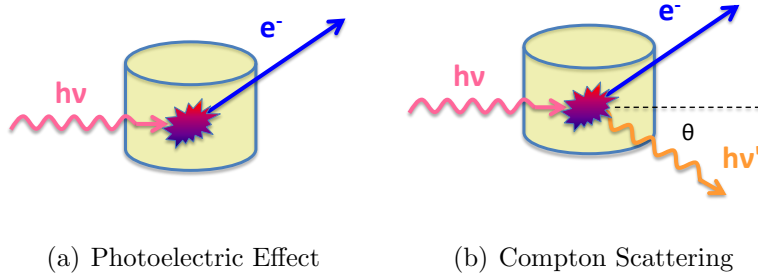
Figure 2.2: Schematic representations of the primary interactions of γ-rays with matter at energies ≤1 MeV.

occur in this energy range are via the photoelectric effect, and through Compton scattering, both of which are illustrated in Figure 2.2. When an electron from the detector material interacts with a γ-ray via the photoelectric effect (Figure 2.2(a)), all of the latter's energy is imparted to the electron, and its resulting kinetic energy is $h\nu - E_B$, where E_B is the binding energy of the electron. The probability of interaction via the photoelectric effect depends heavily on the effective atomic number (Z) of the material, and the overall dependence can be expressed as:

$$P_{PE} \propto \frac{Z^n}{E_\gamma^{3.5}}; \quad 4 < n < 5, \tag{2.1}$$

where the precise value of n depends on the actual γ-ray energy. Because of the power law relationship of the probability of photoelectron production with Z, it is an unproductive process for lighter elements. Compton scattering (Figure 2.2(b)), on the other hand, has a probability $P_{CS} \propto Z$ and is thus far more likely to occur for lighter elements, and indeed is the dominant scattering process in conventional organic materials. When a γ-ray undergoes Compton scattering with an electron, the γ-ray only looses a portion of its energy, and the resulting energy of the scattered γ-ray is:

$$h\nu' = \frac{h\nu}{1 + \frac{h\nu}{m_e c^2}(1 - \cos\theta)}, \tag{2.2}$$

where θ is the angle between the directions of the incident and scattered γ-ray's. For small values of θ, very little energy is imparted to the scattered electron, whereas when $\theta = 180°$ (backscattering), the γ-ray transfers the maximal amount of energy possible to the electron. Backscattering becomes disfavored as the γ-ray energy increases, but in general θ can take on

8

(a) Slow Neutron (<10 eV)   (b) Fast Neutron (≥1 MeV)
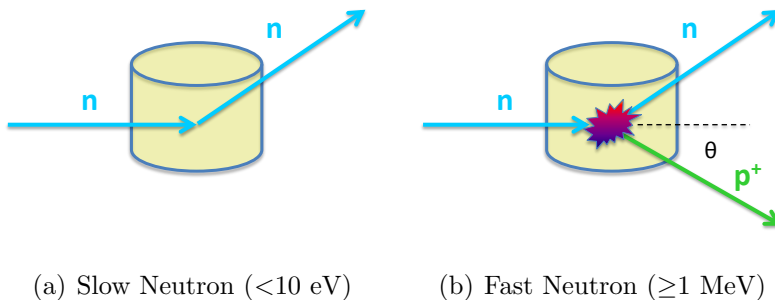
Figure 2.3: Schematic representations of the primary scattering interactions of slow and fast neutrons for organic materials.

any value from $0 - 180°$, and thus there will be a continual distribution of scattered electron energies up to the maximal value when $\theta = 180°$.

2.3   Neutron Interactions

Like γ-rays, neutrons are uncharged, but unlike γ-rays with energies ≤1 MeV, when passing through matter they primarily interact with and are scattered by nuclei. Neutrons are classified in terms of energy into many different categories and subcategories, among which include slow neutrons ($E < 10$ eV) and fast neutrons ($E \geq 1$ MeV), whose primary scattering processes are illustrated in Figure 2.3. Slow neutrons (Figure 2.3(a)) primarily undergo elastic scattering with nuclei, which does not produce ionization in the material, but does serve to dissipate excess kinetic energy with the surroundings. A special subset of slow neutrons are *thermal* neutrons ($E \sim 0.025$ eV), whose kinetic energies are fully equilibrated with the surrounding material, and whose cross sections for capture by nearby nuclei are particularly high. On the other hand, when a fast neutron (Figure 2.3(b)) is scattered by a nucleus, elastic scattering can transfer a significant portion of the neutron's energy, and the resulting positively charged recoil nucleus will produce further ionization as it dissipates this energy along its track. The energy of the resulting recoil nucleus (E_R) is given by:

$$E_R = \frac{4m_R/m_n}{(1 + m_R/m_n)^2}(\cos^2 \theta)E_n, \tag{2.3}$$

9

where m_n and m_R are the masses of the neutron and recoil nucleus, respectively. When the scattering nucleus is the proton of a hydrogen atom, m_n and m_R are essentially equal, and thus $E_R = 1$, meaning that the neutron is capable of transferring all of its energy to the recoil proton. Furthermore, the scattering cross section of hydrogen for fast neutrons is the highest of all the elements, and thus for organic materials, which are typically rich in hydrogen atoms, scattering by hydrogen and thus the production of recoil protons is the dominant process.

CHAPTER 3

Organic Scintillator Photophysics[2,4]

3.1   Energy Transfer, Radiative, and Non-Radiative Processes

The overall function of a scintillating material is to convert a portion of the incident parti-
cle's energy to low energy photons, typically in the ultraviolet to visible wavelength range,
which can be detected using a high sensitivity photodetector such as a photomultiplier tube.
Figure 3.1 depicts a summary of the overall scintillation process, and the primary processes
involved. In typical organic scintillator mixtures such as liquids or plastics, the conjugated
aromatic matrix does not by itself posses good emission properties, and highly fluorescent
dyes are added which are to be the actual emissive component. If the overall content of
these dyes is low (no more than a few wt.%), then it is a reasonable assumption to neglect
any direct excitation of these dyes by the ionizing particle, and instead all ionization and
subsequent relaxation to excited states occurs initially only on the matrix. When the energy
levels of the primary fluorescent dye are suitably matched to the matrix, there exists the
possibility of rapid non-radiative energy transfer from the matrix to the primary dye. In
order to ensure complete and efficient transfer of the excitation energy, primary dye loadings
are typically in the range of 1–5 wt.%, a level that for most dyes will result in significant
loss of the emitted photons due to self-absorption. To mitigate these losses, a secondary,
wavelength shifting dye is added, with much lower loading content (typ. 0.01–0.05 wt.%),
whose sole function is to absorb the photons emitted by the primary dye and re-emit them at
longer wavelengths than can be absorbed by the primary dye, thus maximizing the number
of out-coupled photons emitted from the material.

Figure 3.2 illustrates the various energy transfer and emission processes that are operative

11
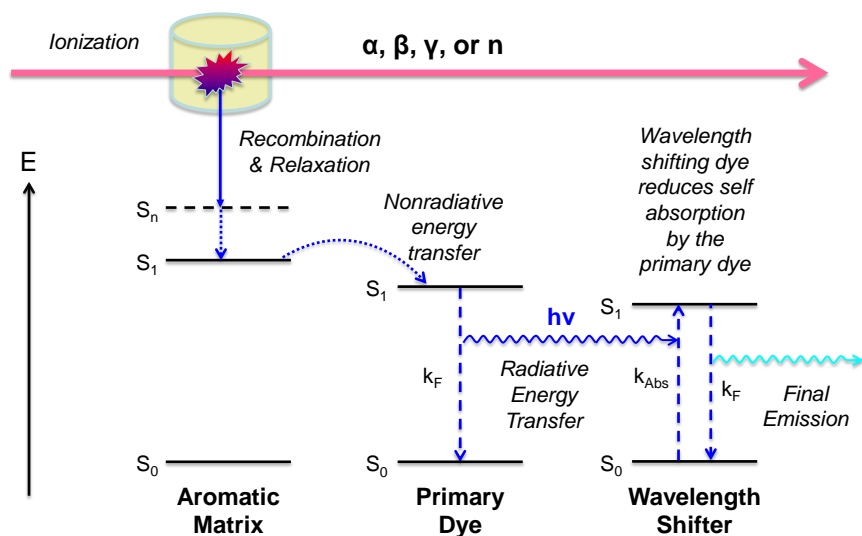
Figure 3.1: Summary of the major photophysical processes involved in the scintillation of organic materials.

for organic scintillators in detail. As was discussed in Chapter 2, the passage of a high energy particle through a scintillating material will result in the formation of ionized matrix molecules, which will eventually recombine with scattered electrons to form excited states. Due to spin statistics, 25% of the excited states that are formed from ion recombination will be singlet states (S_n), while the remaining 75% will be triplet states (T_n). It is also possible that the passage of the high energy particle (or its δ-rays) may result in direct excitation from the ground state to S_n states, a process that would not result in the formation of T_n states. Furthermore, because of the high density of excited states along the particle track, bimolecular reaction of higher excited states can occur, in a process known as *ionization quenching*. Ionization quenching is a very fast process, which will directly compete with internal conversion (IC) for relaxation of the S_n and T_n states to their lower first-excited state levels, S_1 and T_1, respectively, and important processes for ionization quenching should include:[5]

$$S_n + S_m \rightarrow S_0 + [I^+ + e^-] \tag{3.1a}$$

$$S_n \xrightarrow{E_{field}} I^+ + e^-, \tag{3.1b}$$
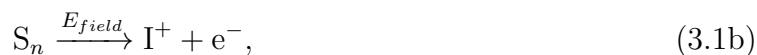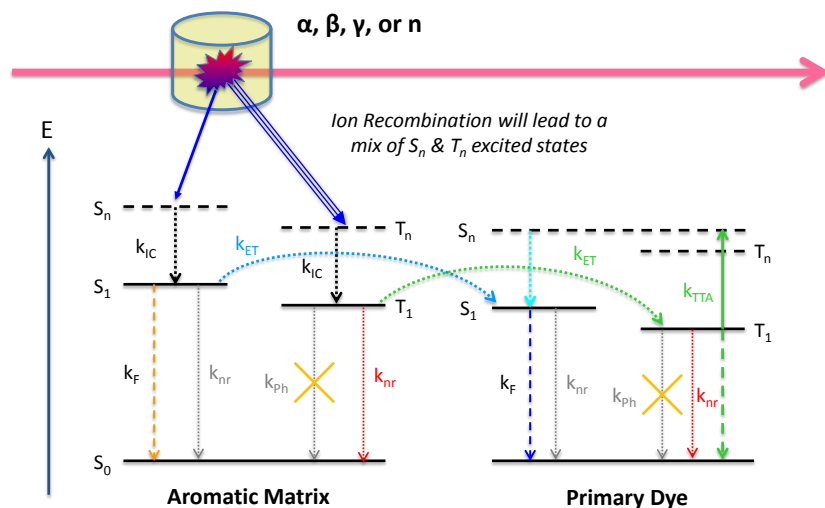
Figure 3.2: Schematic representation of the energy levels and processes responsible for energy transfer and photon emission within organic scintillators.

where E_{field} is the electric field due to the presence of nearby ionized matrix molecules. The magnitude of the ionization quenching will depend on the ionization density, which as discussed in Chapter 2 will depend on the specific energy loss of the high energy particle.[6] The T_n states formed from ion recombination will be less susceptible to ionization quenching, due to the slower nature of the recombination process.[7] The various factors will combine with the result that the final populations of S_1 and T_1 states in the matrix will deviate from the simple 3:1 ratio derived soley from spin statistics, and the precise ratio will be determined by the particle's specific energy loss.

In the absence of a primary dye, the relaxation of S_1 states would proceed either radiatively (fluorescence), or non-radiatively. For T_1 states, radiative relaxation (phosphorescence) is a spin-forbidden transition, and under regular conditions excitations that end up in the T_1 state relax primarily via non-radiative pathways.[8] However, in the presence of a suitable primary dye, fast energy transfer can compete with radiative and non-radiative relaxation to populate S_1 and T_1 states of the primary dye. Primary dyes are typically selected to have quantum yields of fluorescence (Φ_F) close to unity, which results in a high probability of emission for any S_1 state transfered to the primary dye. While the majority of transfered T_1 states will also relax non-radiatively (like for the matrix), due to the high den-

sity of T_1 states along the high energy particle track, bimolecular annihilation of T_1 states (i.e., *triplet-triplet annihilation* (TTA)) becomes a productive process, which is capable of producing additional S_1 states with the overall process:[5]

$$T_1 + T_1 \xrightarrow{k_{\mathrm{TTA}}} S_0 + S_1 \tag{3.2}$$

From spin statistics, generation of an overall singlet state ($S_0 + S_1$) from the combination of two T_1 states will occur only $1/9^{\mathrm{th}}$ of the time, and other possible combinations will lead simply to quenching of the triplet states.[8]

3.2   Kinetics of Scintillation Processes

High energy particles generally move at (γ-rays) or close to the speed of light as they deposit energy along their track. As such the rates associated with the primary ionization processes are extremely fast compared to photophysical processes, and the ionization can be approximated as occurring instantaneously. Because the rate constant for fluorescence (k_{F}) is typically much less than the rate constant for internal conversion (k_{IC}), the generation of all of the S_1 states can also be approximated as occurring instantaneously, at least in terms of the time scale for fluorescent emission. If the matrix was also the primary emissive material (which is the case for single crystal scintillators), the rise time of the scintillation pulse would be well approximated as a step function, with an instantaneous rise to maximum intensity. However, when energy is being transfered to a primary dye, the rate constant for energy transfer (k_{ET}) is typically less than k_{F}, but cannot be neglected entirely, and thus the rise time for scintillation pulses from mixed systems will be finite and is typically characteristic of k_{ET}. On the other hand, the decay of the scintillation pulse is typically characteristic of k_{F}, and with rate constants for fluorescence from organic dyes typically $\sim 10^9$ s^{-1}, corresponding fluorescence lifetimes (τ_F) are $\sim 10^{-9}$ s. As such, typical decay times for pulses generated by organic scintillators is a few nanoseconds, making them particularly suitable for fast timing applications. However, besides the prompt fluorescence corresponding to emission from S_1 states transfered from the matrix, there is an additional delayed fluorescence, since the generation of S_1 states via triplet-triplet annihilation is governed by the respective rate constant
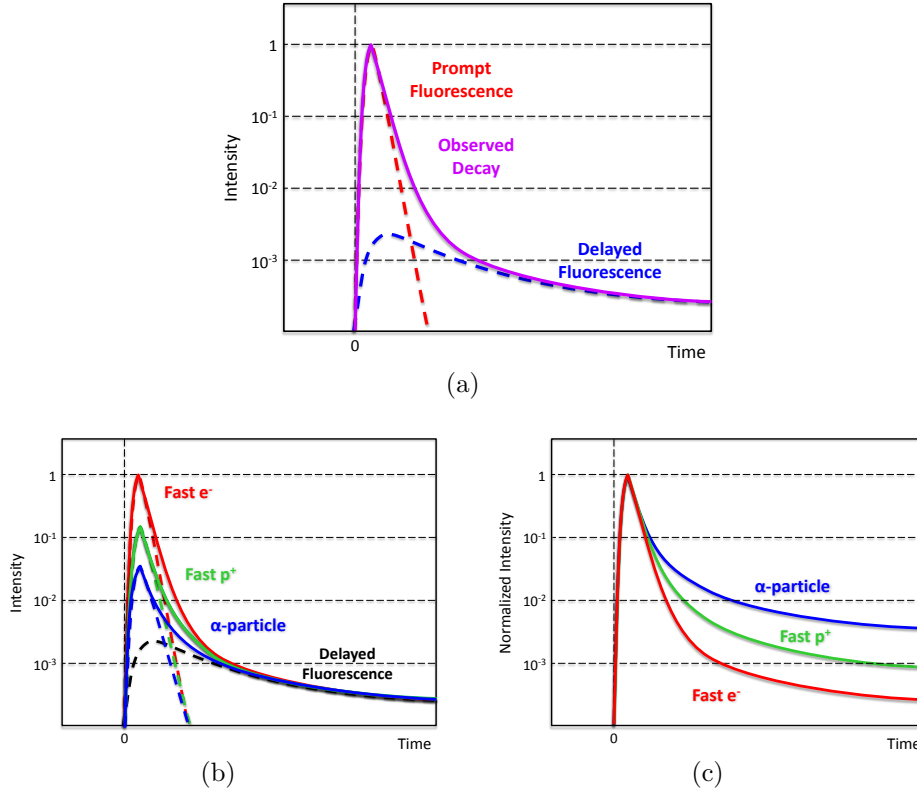
Figure 3.3: Schematic representations of (a) the prompt and delayed components of scintillation decay, (b) the change in decay profile with changing specific energy loss, and (c) the corresponding change in profile when normalized to the peak intensity.

k_{TTA}. Since triplet-triplet annihilation is a bimolecular process, the overall triplet-triplet annihilation rate is $k_{\text{TTA}}[\text{T}_1]^2$, which means that the delayed fluorescence component decays non-exponentially, which is in contrast to the exponential decay of the prompt fluorescence component. Figure 3.3(a) illustrates the contributions of each fluorescence component towards the overall scintillation decay. Because of the strong influence of the specific energy loss of the high-energy particle on the magnitude of ionization quenching of S_n states, while simultaneously having little impact on the T_n states, when the specific energy loss of the high-energy particle is increased (while keeping incident energy unchanged), the absolute intensity of the prompt fluorescence component is correspondingly decreased, as is shown in Figure 3.3(b). Since the intensity of the delayed fluorescence component does not appreciably change with specific energy loss, the end result is that with increasing specific energy loss,

15

the delayed fluorescence component will make up a greater fraction of the *total* emission, which is clearly seen when the decay curves are normalized to the pulse peak, as is shown in Figure 3.3(c). Measurement of the change in the delayed component with changing specific energy loss is the basis for the technique of *pulse shape discrimination* (PSD), which can distinguish between different types of incident particles.

CHAPTER 4

Scintillation Measurements[1,2]

While Chapters 2 and 3 dealt with the mechanisms responsible for the characteristics of a scintillation pulse generated via the interaction of a single high-energy particle, actual scintillation measurements typically require the measurement of a large number of individual events, from which statistical distributions can be derived. To achieve this, specialized electronics and/or signal processing chains are needed that can facilitate the processing of individual pulses, and aggregate the results into an overall measurement. In traditional nuclear electronics, nearly all of the pulse processing is carried out using analog techniques, and analog-to-digital conversion is implemented only at the very end of the signal processing chain, when building up the final probability distributions. However, in recent years, the rise and continual reduction in cost of fast analog-to-digital converters and corresponding digital signal processing capability has lead to increased adoption of entirely digital pulse processing approaches, where analog-to-digital conversion happens as close to the detector as possible. Advantages of this approach are greater stability and reproducibility of the signal processing chain, and ease of use of signal processing techniques that have no corresponding analog equivalent. Furthermore, when digital processing is carried out using field programmable gate arrays (FPGAs), the entire signal processing chain can be rapidly upgraded or reconfigured without the need to replace any physical hardware component, which can drastically increase the potential longevity of signal processing hardware.[9]
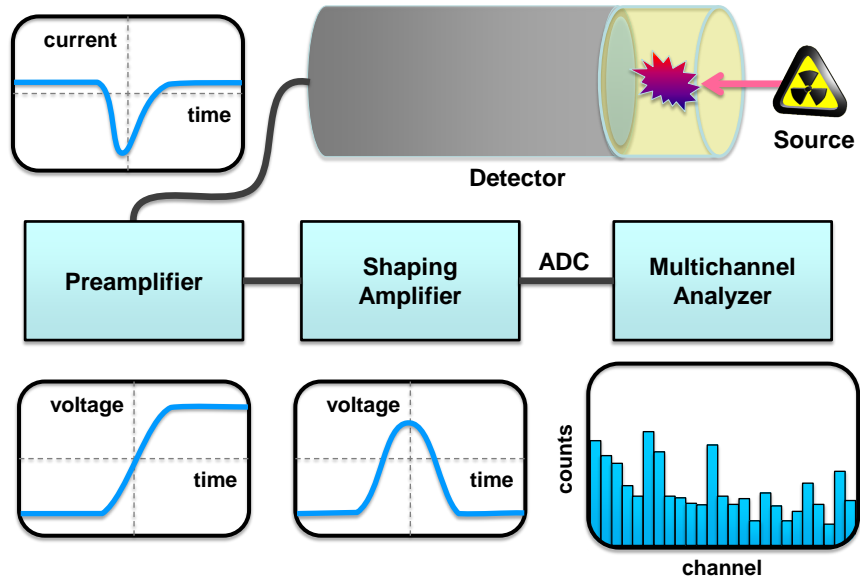
Figure 4.1: Schematic representation of the signal processing chain for pulse height analysis measurements.

4.1 Pulse Height Analysis

When measuring the energy spectrum of a radiation source, the most commonly employed technique is that of *pulse height analysis*, the overall process of which is outlined in Figure 4.1. Fundamentally, the signal produced by a photomultiplier tube upon detection of scintillation photons is a brief pulse of current that (from the formal definition of current) flows from the anode to the photocathode. In an idealized sense, the total amount of charge that is flowing during this current pulse is directly proportional to the number of photons emitted by the scintillator, which in turn depends on the amount of energy that a high-energy particle deposits during an interaction. However, in reality, there are many random processes involved that for any given pulse can lead to deviation from exact proportionality, which include: 1) variation in the number of photons emitted by the scintillator for a particular energy of the exciting particle, 2) variation in the number of photons that reach the photocathode, 3) variation in the actual number of photons that are converted to photoelectrons at the photocathode, and 4) variation in the multiplication factor for the photoelectrons when they impact the first dynode. There will continue to be variability in the multiplication factor

for individual electrons impacting the successive dynodes, but the impact that this variation contributes to the overall variation will be substantially less than that of the first dynode, since far fewer electrons are involved for the latter. In any case, the useful information to be obtained from the pulse is the total amount of charge, but since conventional analog-to-digital conversion requires a voltage signal, conversion of the current pulse to a voltage signal that is easily digitized is required. To accomplish this, the raw signal from the photomultiplier tube is first passed through a *charge-sensitive preamplifier*, which integrates the pulse current to produce a step-like voltage signal where the step-height corresponds to the total charge collected. If the output of the charge-sensitive preamplifier was a purely integrated signal, the voltage level would continue to rise after each successive pulse to unmanageable levels, and thus real charge-sensitive preamplifiers are designed to allow the initial step-like pulse to slowly decay back to baseline with a time constant much longer than the original current pulse (not shown in Figure 4.1). The pulse tail introduced by the charge-sensitive preamplifier is undesirable, especially with higher count rates, and is removed through the use of a *shaping amplifier*, which retains the peak pulse height as the encoded information. The pulse heights are then digitized by a *multichannel analyzer*, which functions identically to a histogram, where the counts accumulated within a single channel (i.e., bin) depends on the number of pulses whose height falls within the channel's range. The final result is the spectrum of histogrammed counts per channel, where increasing channel number corresponds to increasing pulse height.

Pulse height analysis is quite commonly applied to the measurement of the energy spectrum of γ-ray sources, as the energy of a γ-ray is characteristic of the decay of the specific isotope that produced it. In Section 2.2, the details of energy deposition via the photoelectric effect (full energy deposition) and Compton scattering were discussed, and for the latter, it was noted that the precise energy deposited during a particular event is a random process ranging from zero up to a maximum value, which is always less than full energy deposition. Figure 4.2(a) depicts the spectrum of a ≤1 MeV γ-ray source as it would appear according to an idealized scenario where only the statistics of photoelectron production and Compton scattering were taken into account (which also uses a simplifying assumption that the prob-
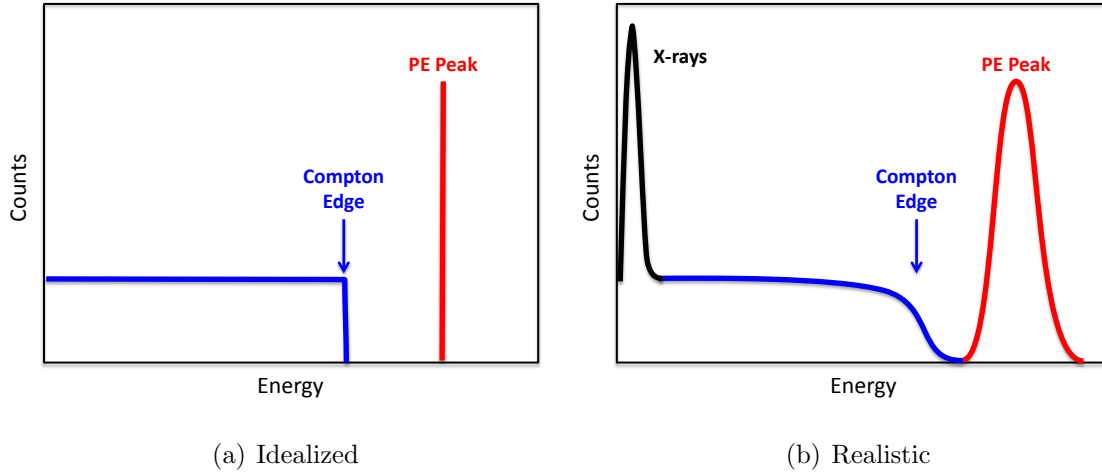
Figure 4.2: Schematic illustrations of the appearances of (a) idealized and (b) realistic γ-ray pulse-height spectra of a typical high-Z scintillator.

ability distribution for Compton scattering is a constant function of the scattering angle θ, which in reality is not the case). In this idealized spectrum, the counts due to Compton scattering make up a continuous distribution in energy up to the maximal allowed energy, which is referred to as the *Compton edge*, and a δ-function peak corresponding to photoelectron generation. It is also assumed for this spectrum that the scintillating material in question has a sufficiently high effective-Z to enable photoelectron production at appreciable rates. For the realistic spectrum depicted in Figure 4.2(b), the variation in pulse height due to the random processes discussed previously has been taken into account, which acts to broaden the ideal distribution and give a finite width to the photoelectron peak. This spectrum also includes a peak at the low energy range that is attributable to detection of X-rays that are generated as a result of X-ray fluorescence from external γ-ray interactions with the surrounding materials, and which accumulate as an artifact. There are additional characteristic features of γ-ray spectra that are not explicitly shown in Figure 4.2(b), but it does serve as a good approximation of the overall appearance of γ-ray spectra of monoenergetic γ-ray sources. Both of the spectra in Figure 4.2 can be calibrated in terms of γ-ray energies from the position of the photoelectron peak, assuming the identity of the γ-ray source is known. However, if γ-ray spectra are acquired with low effective-Z materials such as typical organic scintillators, no photoelectron peak will be detectable, and the Compton distribution will the
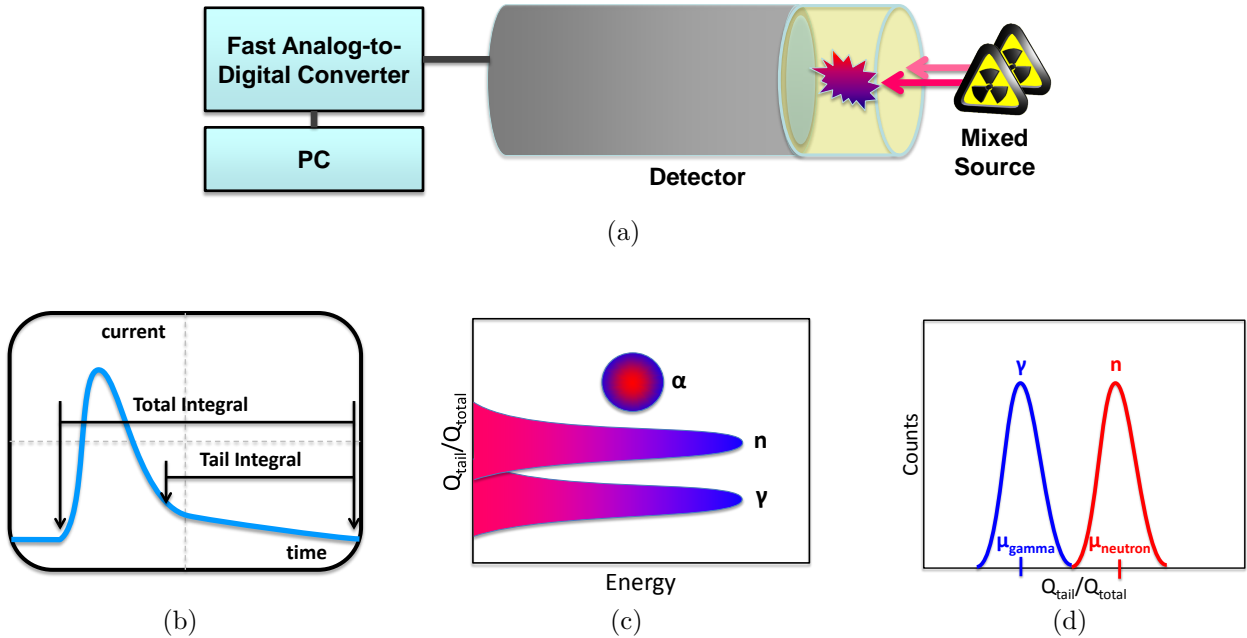
Figure 4.3: Schematic representations of (a) an experimental set-up for PSD measurements, (b) integration windows for processing of digitized pulses, (c) the overall appearance of PSD 2D-histogram plots, and (d) plotting of 1D-historgam data for determination of PSD figure-of-merit.

the principle feature of the spectrum. But since the energy of the Compton edge is always less than the photoelectron peak by a fixed amount, the position of the Compton edge alone can be in such cases used for spectral calibration.

4.2   Pulse Shape Discrimination

Like pulse height analysis, pulse shape discrimination (PSD) measurements can be performed using either analog[10–12] or digital signal processing chains,[13,14] however due to the rather different processing approaches, the appearance and interpretation of data obtained by different means can be quite different.[15,16] In recent years, one of the most popular digital PSD methods has been the *digital charge comparison* method, which is schematically outlined in Figure 4.3. In this approach, the raw signal from the scintillation detector is immediately digitized using a fast analog-to-digital converter, and can either be stored directly

21

to a computer (Figure 4.3(a)),[17,18] or can be processed directly using dedicated digital signal processing hardware.[19,20] In either case, a processing algorithm is applied to each digitized pulse that integrates the pulse over two regions: 1) over the entire pulse (i.e., the *total integral*), and 2) starting at a fixed time after the pulse peak, till the end of the pulse (i.e., the *tail integral*) (Figure 4.3(b)). The ratio of the tail over the total integral (Q_{tail}/Q_{total}, also known as the *PSD result*) is calculated, and a 2D-histogram of Q_{tail}/Q_{total} versus the total integral (i.e., energy) is plotted. Since the delayed fluorescence component for particles with higher specific energy loss ($\frac{dE}{dx}$) makes up a higher proportion of the total fluorescence, a higher specific energy loss will result in a larger tail integral and a higher value of Q_{tail}/Q_{total}. Figure 4.3(c) shows a schematic plot for a hypothetical mixed α/n/γ-source, where each respective particle type is monoenergetic. As discussed in Sections 2.2 and 2.3, interactions of monoenergetic neutrons and γ-rays produce high-energy protons and electrons, respectively, with a continuous range of energies. In Figure 4.3(c), this can be seen as a continuous band for both the neutron and γ-ray distributions. On the other hand, α-particles are charged, and thus capable of depositing their energy directly, and thus only a single peak appears in Figure 4.3(c) for the distribution due to a monoenergetic α-particle source. All of the features in the spectra are shown broadened in a manner similar to that discussed for pulse height analysis, due to the effects of the random nature of photon collection and multiplication.

Calibration of resulting 2D-histogram of a PSD plot can be carried in a similar manner to simple pulse-height spectra of plastics scintillators, i.e., using the position of the Compton edge of the γ-distribution to establish a known energy reference point. Strictly speaking, this only serves to calibrate the energies of pulses due to incident γ-rays, since heavier particles with greater magnitudes of specific energy loss will correspondingly have a greater degree of quenching in the total luminescent output. As such, energies reported for pulses of other particle types are typically reported in units of *energy equivalents*, typically abbreviated in a manner such as "eV-ee".

In order to establish a quantitative evaluation of the discrimination performance of materials relative to one another, a widely used metric is the *PSD figure-of-merit* (FOM), which

is defined as:[21]

$$\text{FOM} = \frac{S}{\delta_{neutron} + \delta_{gamma}}, \tag{4.1}$$

where S is the separation between the neutron and gamma peaks, and $\delta_{neutron}$ and δ_{gamma} are the full widths at half maximum of the neutron and gamma peaks, respectively. The simplest approach for a PSD analysis is to set a cutoff level for the Q_{tail}/Q_{total} PSD result, above which pulses are classified as neutron by the detection algorithm, and then replot the data in a 1D-histogram of counts versus Q_{tail}/Q_{total} (Figure 4.3(d)). For the charge comparison method, Q_{tail}/Q_{total} is higher for the neutron peak, and when the peaks are fit to a Gaussian distribution (characterized by a mean position (μ) and standard deviation (σ)) the FOM equation becomes:

$$\text{FOM} = \frac{\mu_{neutron} - \mu_{gamma}}{2.355 * (\sigma_{neutron} + \sigma_{gamma})} \tag{4.2}$$

In order to ensure that the individual peaks are separated by at least $3(\sigma_{neutron} + \sigma_{gamma})$, a minimum FOM of ≥ 1.27 is required for the material, the value of which establishes a baseline threshold of discrimination performance for usability in real-world applications.

CHAPTER 5

Pulse Shape Discrimination Properties of Plastic Scintillators Incorporating a Rationally Designed Highly Soluble and Polymerizable Derivative of 9,10-Diphenylanthracene[22]

5.1   History of PSD Capable Plastic Scintillators

In contrast to inorganic scintillators, which are among the best materials for γ-ray detection and spectroscopy, organic materials are among the most widely used materials for PSD applications,[1] a primary example of which is the use of PSD based detection methods for fast-n/γ discrimination, which is of particular interest for the detection of special nuclear material. The PSD properties of organic scintillators have a long history dating back to the 1950's.[2] Organic crystals are among the highest performing materials for n/γ PSD, with single crystal *trans*-stilbene being readily considered as having the best known PSD performance.[2,23] On the other hand, PSD is readily achievable in conventional liquid scintillator solutions, which have distinct advantage over organic crystals in terms of cost, scalability, and ease of manufacture and handling. There are some distinct disadvantages of organic liquids, including concerns over toxicity, flammability, the potential for leaks, and the necessity of maintaining strict oxygen free conditions of the solution throughout its life, all of which are even more problematic in the context of very large detector sizes. Despite these shortcomings, liquid scintillator solutions are among the most widely used detector materials for fast neutron spectroscopy and n/γ discrimination.

For other types of detection, plastic scintillators offer many distinct advantages over

organic or even inorganic crystals and liquid scintillator solutions, most notably low cost, very good scalability, and great ease of use and handling, with complex geometries being readily attainable due to the good machinability of typical plastic formulations. Despite all these advantages, plastic materials have until only recently long been regarded as unsuitable for PSD applications due to their inferior discrimination properties. A notable exception to this, however, is the development by Brooks et al. in 1960 of a PSD capable plastic scintillator dubbed as "Plastic 77" by the authors,[24] whose commercialization was attempted under the trade name NE-150 but which was eventually abandoned due to issues with the material's long-term stability.[25] Only in last few years has the demonstration of commercial plastic scintillators with efficient PSD properties been fully realized. The recent breakthrough was made in 2012 when Zaitseva et al. first reported the use of polyvinyltoluene based scintillators with a high loading ($\geq$30%) of 2,5-diphenyloxazole (PPO) as the first plastic scintillator since Brooks' that was capable of achieving efficient n/γ discrimination.[21] The necessity for a high primary dye loading in plastic scintillators was hinted at in their previous work, which established the requirement in PSD capable mixed crystals of a high concentration of primary solute states in order to facilitate triplet-triplet annihilation leading to emission of delayed fluorescence.[26] Since then, the material has been developed into two different commercial materials from Eljen Technology, EJ-299-33A, which has better performance but is relatively soft for a scintillating plastic, and EJ-299-34, which has better mechanical properties but decreased discrimination performance.[27] The mechanical properties of the all these materials are directly related to the high dye loading that enables them to be efficient at pulse shape discrimination. With such high loadings, the dye molecules act as effective plasticizing agents, rendering the resulting material softer than either the base plastic alone or conventional plastic scintillator formulations. Martinez et al. have shown that substitution of of the aromatic polymer matrices with a non-aromatic material such as poly(methyl methacrylate) (PMMA) can be advantageous due to its higher hardness, but the discrimination performance was again diminished.[28]

Another potential problem arising from the use of high primary dye loading is the long term stability of the material, which is a principal issue needing to be addressed with regards

to the current generation of PSD capable plastics. The failure of Brook's "Plastic 77" to be fully realized as the NE-150 commercial material was largely due to the dramatic loss of transparency and whitening which took place over time,[25] presumably due to precipitation of the highly loaded dye components. Blanc et al. have experimented further with the Plastic 77 composition and demonstrated that both incorporating polymerizable additives and cross-linking of the polymer matrix were effective means of preventing precipitation of the dye components.[29] In general, with no other means of fundamentally preventing dye crystallization, a high dye loading will quite likely lead to precipitation, either during fabrication or upon aging, since it will be quite likely that the dye will be above its solubility limit in the cured plastic. The reason for this is at the elevated polymerization temperature with which plastics are typically cured, the dye will typically have a significantly higher solubility than in the monomer at room temperature. If a plastic is cured with a dye content at or near the high temperature solubility limit, upon cooling to room temperature there will be a significant degree of supersaturation of the dye, which can lead to precipitation either during the cooling itself, leading to an opaque material, or slowly over time, leading to a gradual loss of transparency. Additionally, the thermodynamic solubility limit of the dye in a polymer may be fundamentally lower than in the liquid monomer at any given temperature, which again would lead to a situation of supersaturation of the dye in the cured plastic. Lower dye loadings can be utilized to improve long term stability of the material, but not without some sacrifice in PSD performance (at least for presently known PSD-capable dyes). As such, development of new approaches to stabilization of high dye loadings remains a key objective for the development of new PSD capable plastics.

5.2   Materials Challenges for PSD Capable Plastics

There are several key factors to the design of novel primary dyes that can specifically address all of the issues associated with the high dye loading method. First and foremost is the need for a primary dye with high solubility to achieve loadings capable of effecting good PSD performance, but without leading to precipitation of the dye or loss of mechani-

cal properties, especially at timescales corresponding to the expected useful lifetime of the material. While 2,5-diphenyloxazole has been shown to be a PSD capable dye in plastic scintillators, it is anticipated that there are a number of other possible candidates, some of which may be able to achieve significantly better performance than even the best commercial PSD plastic. However, there are very few if any efficient and common scintillating dyes other than 2,5-diphenyloxazole or its derivatives that have solubilities in aromatic solvents high enough to achieve decent PSD performance.[21,30] With all this in mind, the approach taken in this work was to identify a candidate scintillating dye with overall good properties and good PSD performance, and then functionally derivatize the parent molecule to overcome the shortcoming of solubility and stability in the final plastic. To achieve the former, the introduction of long, flexible, and/or branched alkyl chains can greatly enhance solubility while simultaneously lowering the compounds melting point, while for the latter, the introduction of polymerizable groups can allow for direct bonding of the dye to the polymer backbone, eliminating the ability of the dye to precipitate from the plastic upon cooling. It is worth noting that at least one previous attempt has been made, albeit unsuccessfully, to directly incorporate a scintillating dye via copolymerization into a PSD-capable plastic. In their report, O'Bryan et al. demonstrated PMMA-based plastic scintillators loaded up to 30 wt.% with a polymerizable *trans*-stilbene derivative, but the resulting material failed to demonstrate any performance for n/γ PSD.[31]

5.3   Design, Synthesis, and PSD Properties of a Polymerizable Derivative of 9,10-Diphenylanthracene

All of the factors addressed in Section 5.2 were taken into account for the design and synthesis of an entirely new primary dye to address and fulfill each of these key requirements. The specific approach is based upon the derivatization of 9,10-diphenylanthracene (DPA), a scintillating dye known in single crystal form to posses both good PSD and overall scintillator performance,[32–34] and Figure 5.1 details the chemical structure of the proposed primary dye (DPA-DHS, where DHS='dihexylstyrene'). Functionalization of the 9,10-diphenylanthra-

DPA-DHS   **DMPA**
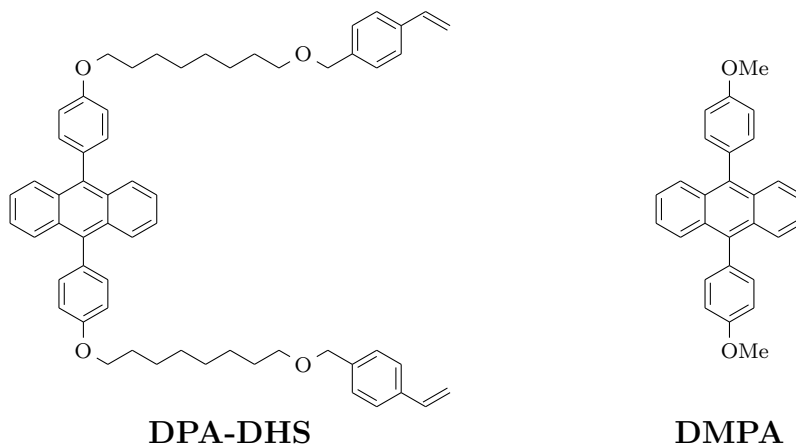
Figure 5.1: Structure of (left) the DPA-DHS dye monomer and (right) a synthetic interme-
diate also utilized for comparative spectral studies.

cene core by introduction of aryl ether linkages onto the pendant phenyl rings introduces the
flexible hexyl spacer groups, whose primary intended function is to enhance the solubility
of the dye while simultaneously lowering its melting point, both of which are critical factors
in allowing for the required high loading content. At the distal end of the spacer chains
are styrenyl groups, which are purposefully included in the proposed structure over other
potential polymerizable groups in an attempt to achieve optimal incorporation of the dye into
the overall polymer matrix. In addition, the presence of two polymerizable groups per dye
molecule was intended to allow the dye to simultaneously act as a cross-linker for the matrix,
and since high loadings are sought after, such a high degree of cross-linking would lead to
a material that is quite hard and tough, potentially more so than the current generation of
PSD plastics.

5.4   Spectral and Electronic Properties of the DPA-DHS Monomer

The absorbance and photoluminescence spectra of 9,10-diphenylanthracene, DPA-DHS, and
the intermediate compound 9,10-bis(4-methoxyphenyl)anthracene, are shown in Figure 5.2(a)
and Figure 5.2(b), respectively. In these spectra, the effects that the introduction of the ether
linkage to the 9,10-diphenylanthracene core have on the electronic structure of 9,10-bis(4-
methoxyphenyl)anthracene and DPA-DHS can readily be observed. In Figure 5.2(a), a very
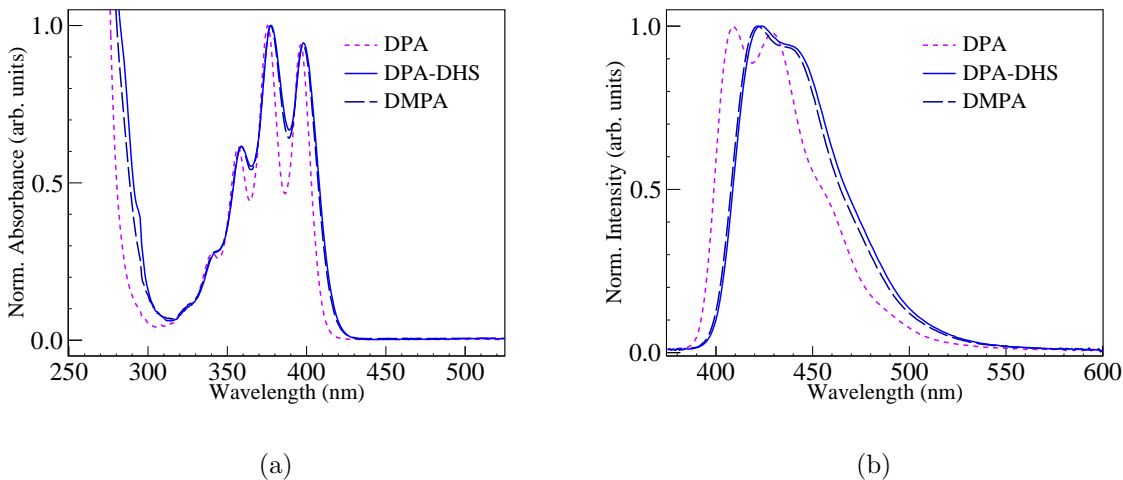
Figure 5.2: (a) Absorbance spectra of 9,10-diphenylanthracene (DPA), DPA-DHS, and 9,10-bis(4-methoxyphenyl)anthracene (DMPA) as dilute solutions in CHCl$_3$, (b) Photoluminescence Spectra of 9,10-diphenylanthracene, DPA-DHS, and 9,10-bis(4-methoxyphenyl)anthracene as dilute solutions in toluene.

slight red shifting ($\sim$2 nm) of the absorbance maxima of 9,10-bis(4-methoxyphenyl)anthracene and DPA-DHS is observed relative to 9,10-diphenylanthracene, and there is additional broadening of the vibronic sublevels for the former compounds. In Figure 5.2(b), the redshifting of the 9,10-bis(4-methoxyphenyl)anthracene and DPA-DHS emission spectra relative to 9,10-diphenylanthracene is more prominent ($\sim$10 nm), and again broadening of the vibronic sublevels is observable. Given that the value of the redshifting is much smaller for the absorbance spectrum, it is reasonable to conclude that the main effect of the introduction of the alkoxy substituents onto the electronic properties of 9,10-bis(4-methoxyphenyl)anthracene and DPA-DHS is to introduce additional stabilization to their respective S$_1$ states relative to that of 9,10-diphenylanthracene, while leaving the transition energies at the corresponding ground state geometries relatively unchanged from one another. Additionally, the extra degrees of freedom to the vibrational modes introduced via the alkoxy substituents is a likely factor controlling the increased broadening of the vibronic sublevels of the spectra of 9,10-bis(4-methoxyphenyl)anthracene and DPA-DHS. Overall, 9,10-bis(4-methoxyphenyl)-anthracene and DPA-DHS have virtually identical spectra to one another, which is indicative that increasing the length of the alkyl chain attached to the aryl ether linkage has little if

29

any effect on the electronic properties of the 9,10-diphenylanthracene core. The photoluminescence quantum yields (Φ_{PL}) of 9,10-bis(4-methoxyphenyl)anthracene and DPA-DHS in toluene were measured to be 0.84 and 0.95, respectively. The photoluminescence quantum yield measured for 9,10-bis(4-methoxyphenyl)anthracene is noticeably higher than a previously reported value of 0.59,[35] although the authors do not specify whether the measurements were performed on deoxygenated solutions, which could account for the observed discrepancy. Overall, the modification of the 9,10-diphenylanthracene core to obtain the final structure of DPA-DHS, especially given the latter's high photoluminescence quantum yield, does not appear to significantly disrupt its potential performance as a scintillating dye, at least in terms of its molecular emission.

5.5 Fabrication and Photoluminescence of DPA-DHS Based Plastic Samples

The DPA-DHS monomer obtained from our synthetic efforts was found to be quite amenable to processing through standard solution casting methods. A large reduction in melting point on account of the structural modifications was observed for DPA-DHS (~120 ℃) as compared to 9,10-diphenylanthracene (~250 ℃). While loadings of ≤10 wt.% could dissolve in methylstyrene at room temperature, heating the undissolved mixture to the curing temperature of 80 ℃ along with gentle agitation was able to achieve full dissolution of loadings as high at 50 wt.%. Higher loading may even be possible but become very difficult to achieve practically; as the DPA-DHS content is increased, the dye/monomer solution becomes very viscous, and with the high degree of cross-linking, the solution begins to rapidly gel within a few minutes, after which further mixing becomes impossible. The rapid gelation of the DPA-DHS based plastic samples (due to the cross-linking nature of its multiple polymerizable end-groups) is in direct contrast to 9,10-diphenylanthracene based plastic samples with 9,10-diphenylanthracene content ranging from 0.5–2.5 wt.% fabricated for comparative purposes, for which noticeable gelation was observable only after a few hours into the curing.

The obtained plastic scintillator samples were found to have good clarity, with no signs of

phase separation, cloudiness, or precipitation of the primary dye. As a qualitative assessment of the outcome of the copolymerization, samples of DPA-DHS based plastic along with cast poly(vinyl toluene) obtained through the same polymerization procedure but with no added dye were subjected to swell tests in dichloromethane. After several hours, which was an adequate amount of time to achieve full dissolution of the cast poly(vinyl toluene), the DPA-DHS based plastic samples showed varying degrees of swelling, with the lowest loading of DPA-DHS tested (3 wt.%) showing a significant volume expansion, and the highest loading (50 wt.%) demonstrating only minimal volume expansion). Thus, the degree of crosslinking (i.e., resistance to swelling) is directly dependent on the loading of the DPA-DHS, which is a direct indicator of incorporation of the crosslinking DPA-DHS monomer into the polymer matrix (which is otherwise non-crosslinking). Additionally, some residual amount of unreacted or oligomeric DPA-DHS monomer was evidenced via the fluorescence of the swelling solution at the end of the tests, which is not unexpected given that residual monomer is commonly observed for the bulk polymerization of plastics.[36,37] All of the DPA-DHS containing samples prepared were found to be mechanically robust and easily polished, as is to be expected from their crosslinking. DPA-DHS based plastic samples with no added wavelength shifter ranged from nearly colorless at low DPA-DHS content to a pale yellow in color at the highest DPA-DHS concentrations.

Additional DPA-DHS based plastic samples were prepared with 0.05 wt.% of Coumarin 6 added to act as a wavelength shifter; Coumarin 6 was chosen for this role on account of the good matching of its absorbance spectrum to the molecular emission spectrum of DPA-DHS, which is illustrated in Figure 5.3. Wavelength shifters employed in most commercial plastics (e.g., 1,4-bis(5-phenyloxazol-2-yl) benzene (POPOP)) are typically blue to violet emitters themselves, and their absorbance spectrums do not match well with the emission spectrum of DPA-DHS. In addition, the Stokes-shift for a wavelength shifter can not be excessively small (i.e., in an attempt to shorten the emission wavelength), as this would cause too much overlap of the shifters absorption/emission spectra, and would lead to excessive self absorption by the shifting dye, defeating its intended purpose. As such, the use of a green emitting wavelength shifter such as Coumarin 6 is necessary for the DPA-DHS based plastic system to

31
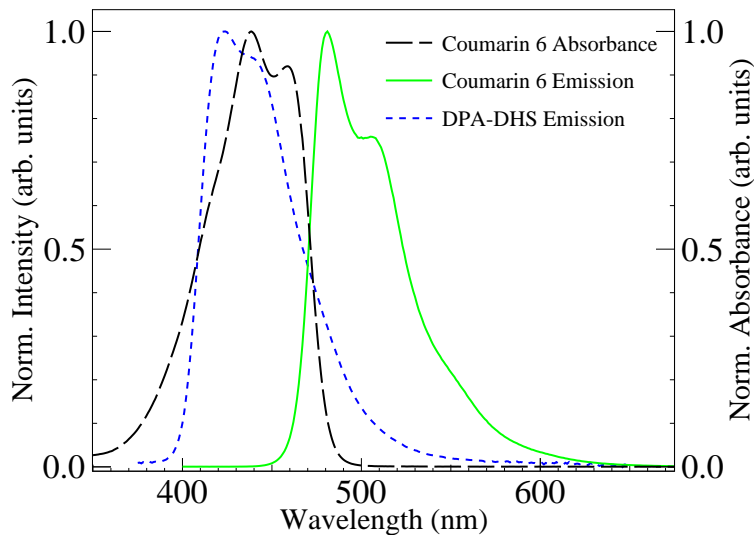
Figure 5.3: Emission/Absorbance spectra of Coumarin 6, overlaid with the emission spectrum of DPA-DHS, all as dilute solutions in toluene.

maximize the number of out-coupled photons, although the primary consequence will be that the longer wavelength photons will have a lower detection efficiency by typical blue-sensitive photomultiplier tubes (which is factored out from the measurements through spectral sensitivity correction as is described in Appendix B). Samples wavelength shifted with 0.05 wt.% of Coumarin 6 were bright yellow-green in color, and representative photographs of the unshifted and shifted DPA-DHS samples along with EJ-299-34 for comparison are shown in Figure 5.4. The emission spectra of the commercial EJ-299-34, unshifted 50 wt.% DPA-DHS based plastic, and Coumarin 6 shifted 50 wt.% DPA-DHS based plastic scintillator samples is shown in Figure 5.5, along with a plot of the photo detection efficiency of a typical blue sensitive photomultiplier tube photocathode (Hamamatsu R878). The emission for the unshifted samples was bright blue in color, with emission maxima centered around 450 nm. This is slightly longer in wavelength than the commercial EJ-299-34 plastic, with an emission maximum centered at 425 nm. Samples wavelength shifted with Coumarin 6 displayed bright green emissions with their maxima around 510 nm.

(a) Visibile Illumination   (b) UV Illumination
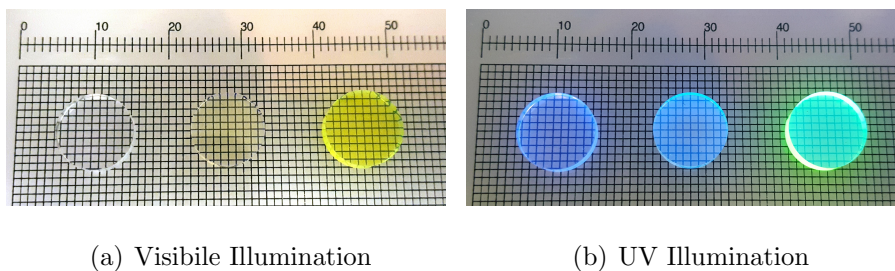
Figure 5.4: Photographs of (left) EJ-299-34, (middle) unshifted 50 wt.% DPA-DHS based plastic, and (right) Coumarin-6 shifted 50 wt.% DPA-DHS based plastic.
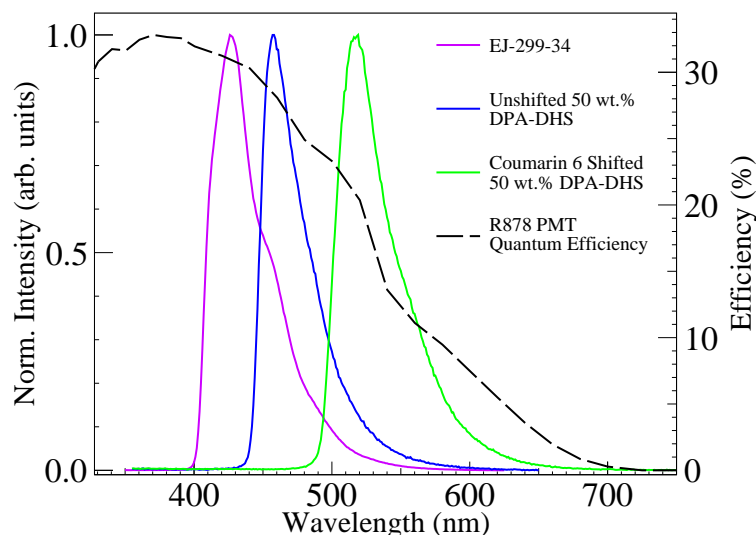
Figure 5.5: Emission Spectra of EJ-299-34, unshifted 50 wt.% DPA-DHS based plastic, and Coumarin 6 shifted 50 wt.% DPA-DHS based plastic.

5.6 γ Light Yields of DPA-DHS Based Plastic Samples

Figure 5.6 plots the measured ^{137}Cs light yields as a function of DPA-DHS content for DPA-DHS based plastic samples with both no added wavelength shifter, and shifted with 0.05 wt.% of Coumarin-6. Additionally, Figure 5.6 also plots the light yields for a series of comparative 9,10-diphenylanthracene based plastic samples with no added wavelength shifter, and prepared with 9,10-diphenylanthracene concentrations ranging from 0.5 to 2.5 wt.%, which serve as an additional means of comparing the scintillation properties of the DPA-DHS monomer to that of unfunctionalized 9,10-diphenylanthracene. When the primary
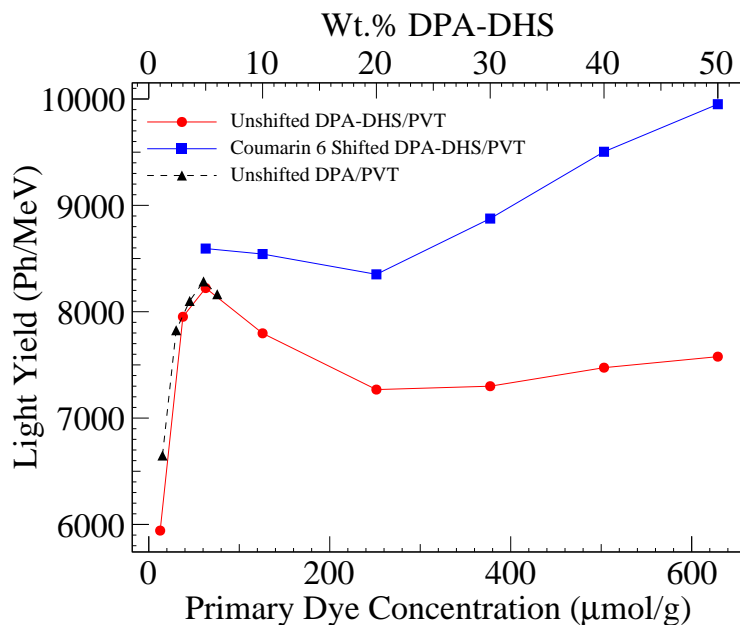
Figure 5.6: Light yields of unshifted DPA-DHS based plastic (DPA-DHS/PVT) samples (top & bottom axis), Coumarin 6 shifted DPA-DHS based plastic samples (top & bottom axis), and unshifted 9,10-diphenylanthracene based plastic (DPA/PVT) reference samples (bottom axis only).

dye contents are compared on a concentration basis, it can clearly be seen that at least in the measurable range (for 9,10-diphenylanthracene) of lower dye loading, the light yields of the unshifted 9,10-diphenylanthracene based plastic and unshifted DPA-DHS based plastic are nearly identical to one another, with the 9,10-diphenylanthracene based plastic slightly outperforming the DPA-DHS based plastic samples. This slightly higher performance is in all likely hood directly attributable to the slightly higher photoluminescence quantum yield of 9,10-diphenylanthracene compared to DPA-DHS. The close correspondance of the light yields of 9,10-diphenylanthracene based plastic and DPA-DHS based plastic is a strong indicator that, at least in the lower concentration range, the scintillating properties of the two primary dyes are functionally equivalent to one another, and that copolymerization with the poly(vinyl toluene) matrix does not lead to quenching of the DPA-DHS dye. For both shifted and unshifted DPA-DHS based plastic, the samples with a loading of 20 wt.% split the plots into two distinct regions. Below 20 wt.%, the light yield in the unshifted samples

is strongly rising up to a maximum of 8200 photons/MeV at 5 wt.%, and then again falling down to a local minimum of 7300 photons/MeV at 20 wt.%. A similar behavior is also seen in the data for the shifted samples, although the light yield at 5 wt.% loading is a slightly higher 8600 photons/MeV but falls much more slowly to a minimum of only 8350. Above 20 wt.%, the light yields of the unshifted samples remain largely unchanged, except for a slight positive trend up to 7600 photons/MeV at 50 wt.% loading, but for the shifted samples, a strong positive trend is evident up to 9950 photons/MeV, which is the highest for any of the samples DPA-DHS samples tested.

It is well known that 9,10-diphenylanthracene is relatively immune to the effects of concentration quenching, due to steric interaction of the phenyl rings at the 9,10-positions preventing the formation of excimer excited states.[32,38–41] In addition, the γ light yield for high quality single crystal 9,10-diphenylanthracene has been reported by van Loef et al. as 16,000 photons/MeV[34]. If one assumes that these basic properties are approximately the same for the diphenylanthracene cores in the DPA-DHS plastic, then the trends observed in our light yield data can be explained as follows. At a DPA-DHS content around 5 wt.%, the concentration is high enough to ensure efficient transfer of excitation energy from the poly(vinyl toluene) matrix (although this efficiency is quite likely less than unity), and yet the concentration is still low enough that effects of self absorption by DPA-DHS are still low enough that the overall light yield is maximized in this region. As the DPA-DHS content is increased up to 20 wt.%, the efficiency of energy transfer from host to dye is relatively unchanged, but the increasing concentration of DPA-DHS is leading to a greater contribution of self absorption by DPA-DHS. For the unshifted samples, with no means of preventing loss due to self absorption, the light yield is falling in this region much faster than for the shifted ones. Above 20 wt.%, the same effects of an ever increasing contribution of DPA-DHS self absorption is still present, but at concentrations this high, it is no longer a valid assumption that primary excitation is occurring only on the poly(vinyl toluene) host, since at this point a significant volume fraction of the material is occupied by the diphenylanthracene cores. Direct excitation of the cores by the passage of the high energy particle is expected to be a more efficient luminescent process, since no transfer of excitation energy needs to take
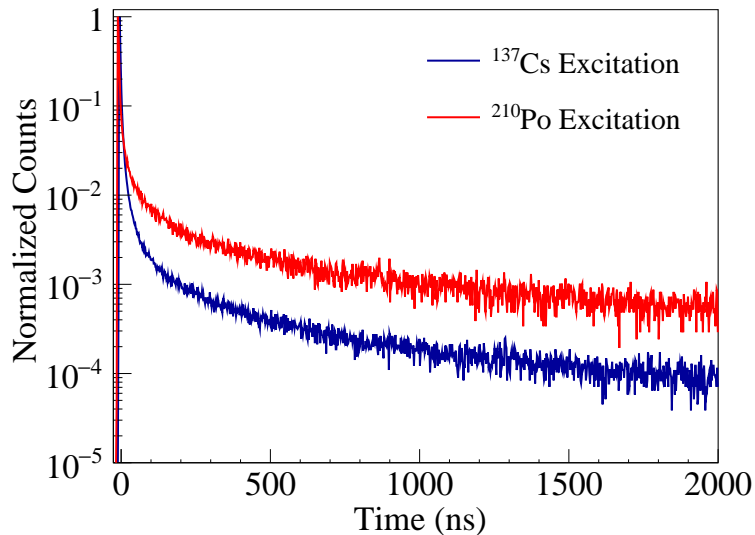
Figure 5.7: Scintillation Decay of EJ-299-34 under α- & γ-irradiation.

place, and thus the luminescent efficiency for direct excitation depends only on the quantum yield of the dye. As the DPA-DHS content is increased up to 50 wt.%, a greater proportion of excitation is occurring directly on the diphenylanthracene cores, and thus the overall scintillation efficiency (before factoring in the effects of self absorption) is increasing. For the unshifted samples, the increasing efficiency and the increasing effect of self absorption are directly competing to keep the light yield relatively unchanged, whereas for the shifted samples, the strong effect of the increasing efficiency is directly observable.

5.7 γ- and α-Scintillation Decays of EJ-299-34 and DPA-DHS Based Plastic Samples

Figure 5.7 compares the peak-normalized scintillation decay of the EJ-299-34 commercial plastic under both α- and γ-irradiation, while Figure 5.8 plots the corresponding data for both unshifted and Coumarin 6 shifted DPA-DHS samples at loadings of both 10 wt.% and 50 wt.% of primary dye.

The decay curves obtained for EJ-299-34 typify the behavior expected for a material with good PSD performance, as there is a substantial increase in the fraction of light emitted as
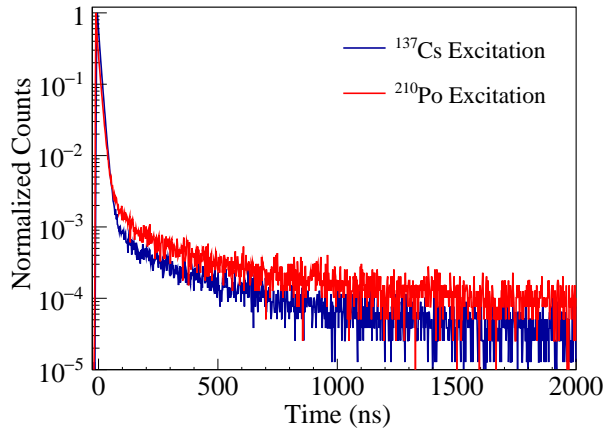
(a) 10 wt.% DPA-DHS (unshifted)
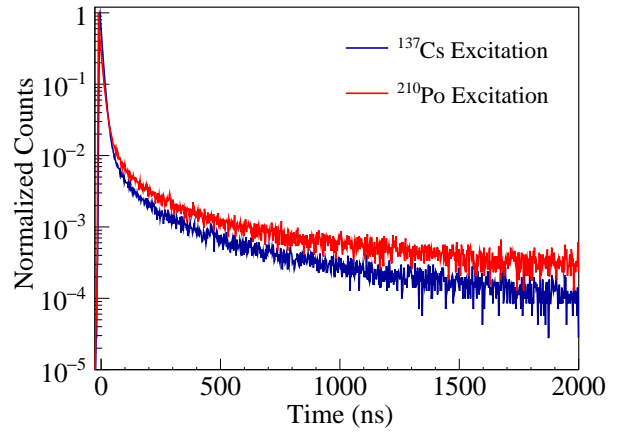
(b) 50 wt.% DPA-DHS (unshifted)
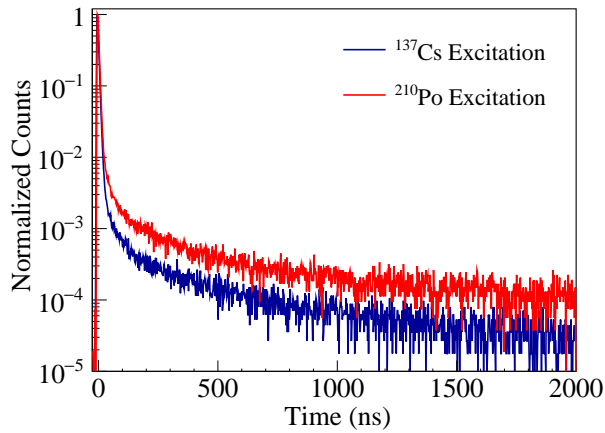
(c) 10 wt.% DPA-DHS (Coumarin 6 shifted)
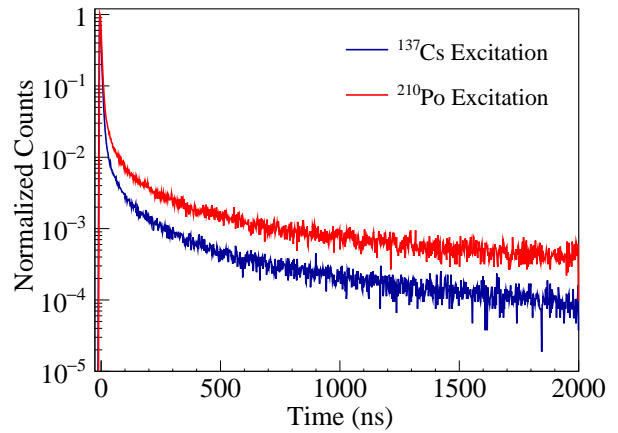
(d) 50 wt.% DPA-DHS (Coumarin 6 shifted)

Figure 5.8: Comparison of Scintillation Decays of DPA-DHS based plastic Samples.

part of the decayed component upon going from γ- to α-excitation. While the decay curves of the unshifted and Coumarin 6 shifted 50 wt.% DPA-DHS samples (Figure 5.8(b) and Figure 5.8(d)) do show increases in the delayed light component upon α-excitation, the relative changes are noticeably less that that observed for EJ-299-34. The relative change in the fraction of delayed light is higher for the Coumarin 6 shifted sample as compared to the unshifted one. From the α-decay data, it can be observed that at a time of 1 μs, the emission for all three of these samples has decayed to approximately the same value, nominally 0.1% of the peak value. However, the main difference in these samples lies in the proportion of delayed emission in the decay curves under γ-excitation. At 500 ns, the

37

emission from EJ-299-34 has decayed to ∼0.05% of the peak value, while at 1 µs, the emission has decayed to just above 0.01%. For both the shifted and unshifted 50 wt.% DPA-DHS samples, the emission at these time points is noticeably higher, and for the unshifted sample in particular the emission at 500 ns has decayed to just under 0.1% of the peak value, and to ∼0.02% at 1 µs. This greater proportion of delayed emission under γ-excitation is the primary factor that is causing the decreased change in delayed emission observed for these samples. The decay curves of the unshifted and Coumarin 6 shifted 10 wt.% DPA-DHS samples (Figure 5.8(a) and Figure 5.8(c), respectively) have significantly lower proportions of delayed light as compared to EJ-299-34 or the 50 wt.% DPA-DHS samples. For instance, at a time of 1 µs, the emission under α-excitation for both of these samples has decayed to a value just above 0.01% of the peak value. This is to be expected, since the primary dye content at this loading level is inadequate to allow for efficient triplet migration and subsequent annihilation. Furthermore, there is little difference in either sample between the fraction of delayed light between γ- and α-excitation.

The scintillation decay data also serves to provide additional evidence for the role that self-absorption plays in the difference in performance between the unshifted and Coumarin 6 shifted DPA-DHS based plastic samples. Table 5.1 summarizes the values of the fast scintillation decay components of the tested samples that were obtained from fits of the lifetime data. From these values, it can clearly be seen that significantly longer prompt decay times were observed for both the 10 wt.% and 50 wt.% loadings of the unshifted samples (∼10 ns) as compared to the shifted (∼5 ns), despite the equivalent DPA-DHS content between the two groups. It is known that the observed lifetimes of organic scintillators depend both on the thickness and degree of self absorption within the material, since fluorescence photons absorbed by the sample may still be re-emitted, but the timing of this secondary emission is still governed by the molecular fluorescence decay lifetime.[42] Given this fact, it can be clearly seen that this increase in prompt decay time for the unshifted samples is directly attributable to their higher degree of self absorption. A further example of this can be seen in the Coumarin 6 shifted samples, where the 50 wt.% sample was found to have slightly longer prompt decay times than the 10 wt.% sample, which would suggest that at the highest

Sample	DPA-DHS Content	Source	Fast Decay (ns)
EJ-299-34	–	^{137}Cs	3.3
		^{210}Po	3.5
Unshifted DPA-DHS	10 wt.%	^{137}Cs	9.9
		^{210}Po	10.1
	50 wt.%	^{137}Cs	9.6
		^{210}Po	10.5
Coumarin 6 Shifted DPA-DHS	10 wt.%	^{137}Cs	4.7
		^{210}Po	5.0
	50 wt.%	^{137}Cs	5.4
		^{210}Po	6.2

Table 5.1: Fast Scintillation Decay Components of Tested Samples.

DPA-DHS concentrations, the self absorption begins to directly compete with the much more efficient absorption by the wavelength shifting dye.

5.8 α/γ PSD Properties of DPA-DHS Based Plastic Samples

Figure 5.9 plots the 2D histograms of the PSD result (Q_{tail}/Q_{total}) versus energy for data acquired for the commercial EJ-299-34 material, while Figures 5.10 and 5.11 plot the same results for unshifted DPA-DHS based plastic samples and samples shifted with 0.05 wt.% Coumarin 6, respectively. The PSD figure of merit (FOM), defined as the separation between the two particle peaks over the sum of each respective FWHM, was measured as 2.43 using a 100 keV threshold energy for the EJ-299-34 data. This value is well above the threshold criterion for useful PSD performance established by Zaitseva et al. as a value of 1.27.[21] The data shown in Figure 5.9 also supplements the results reported by Nyibule et al. for the α/γ PSD properties of the original EJ-299-33 plastic formulation.[43] Figure 5.12 plots the FOM results for both unshifted and shifted DPA-DHS based plastic samples plotted as a
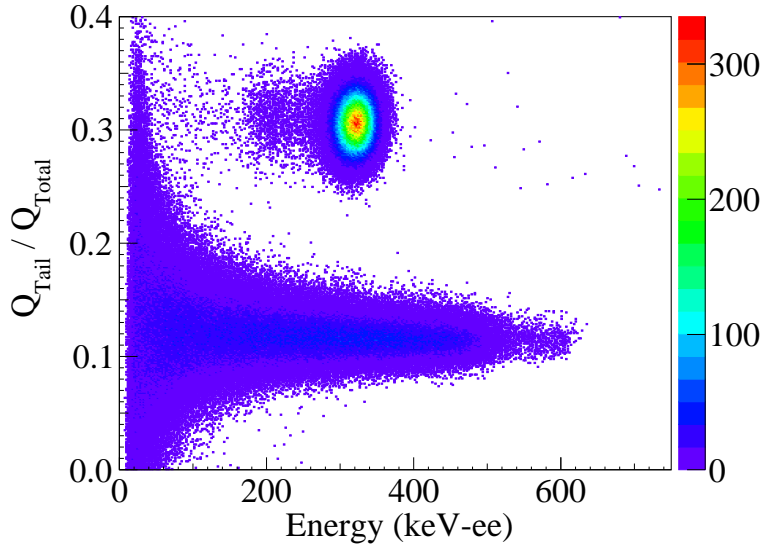
Figure 5.9: ^{210}Po/^{137}Cs PSD plot of commercial EJ-299-34 plastic.

function of primary dye content, using the same 100 keV threshold energy. For the unshifted samples, while there is some increase in the FOM as the content is increased above 10 wt.%, the FOM trends toward a decrease above 20 wt.% and never is higher than 0.7. In contrast, the wavelength shifted samples show an approximately linear trend towards increasing FOM values, with the 50 wt.% sample displaying the highest obtained FOM value of 1.05, a value which is close to but less than the 1.27 threshold criterion. This is visually observable in Figure 5.11 that the α distribution is not cleanly separated from the γ branch, with a slight degree of overlap between the two. The significantly poorer performance of the unshifted samples can, like the light yield results, be largely be attributed to the self absorption by the DPA-DHS dye, although some of the effect is also directly attributable to the differences in the decay curves shown in Figure 5.8. Since the charge comparison method relies on the measurement of relatively low light levels in the tail of the pulse, any decrease of detectable photons attributable to self absorption will have a significant and detrimental effect on the achievable PSD performance of the material. This is further evidenced by the large decrease in apparent α energy that is observed with increasing dye content. For the 10 wt.% sample, the apparent energy of the alpha peak is less then that of EJ-299-34, with approximate values of 260 keV-ee and 320 keV-ee, respectively, and decreases down to approximately 170 keV-ee
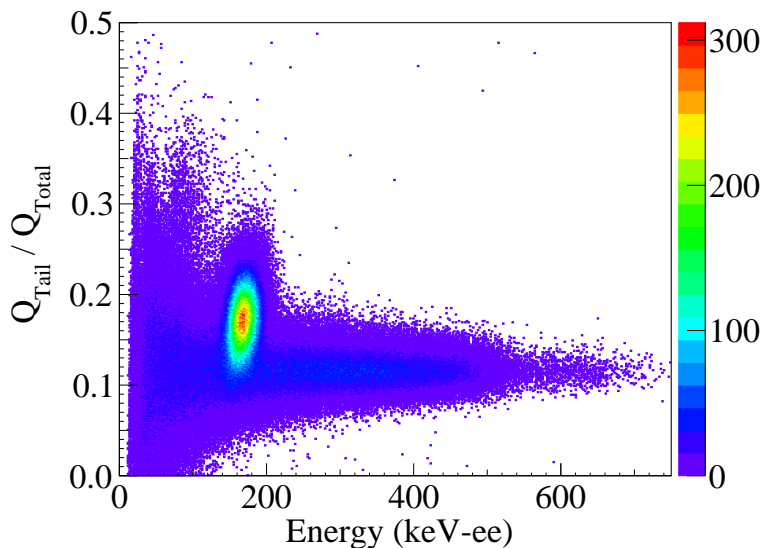
Figure 5.10: ^{210}Po/^{137}Cs PSD plot of unshifted 50 wt.% DPA-DHS based plastic.

for the 50 wt.% sample. Since all of the energy of the incident α-particles is absorbed within a thin surface layer on the face of the samples opposite of the photomultiplier tube, the emitted light must travel the maximal distance through the samples and is thus will experience a large and uniform degree of loss due to self absorption, as compared to excitation across the entire volume of the sample in the case of incident γ-particles. On the contrary, the apparent alpha energy of the wavelength shifted samples is largely unchanged as the content of DPA-DHS is increased, decreasing slightly from 250 keV-ee to 235 keV-ee for the 10 and 50 wt.% samples, respectively.

There are potentially several factors that can contribute to the fact that the Coumarin 6 shifted samples do not match the performance level of the commercial EJ-299-34 plastic. From the photoluminescence spectra shown in Figure 5.5, it is obvious from the longer wavelength emission of the Coumarin 6 samples that the overall detection efficiency by the R878 photomultiplier tube for scintillation photons is significantly lower as compared to EJ-299-34. Thus while the light yields of EJ-299-24 and the shifted 50 wt.% DPA-DHS are approximately the same, overall fewer photons are detected for the latter, which will result in loss of precision in terms of quantifying the relatively small amounts of delayed light emitted by the sample. However, given that the relative change in the slow component
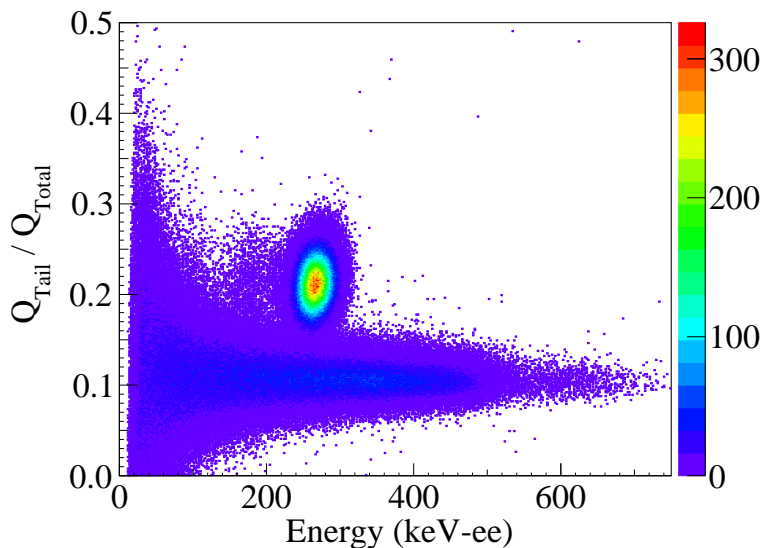
Figure 5.11: ^{210}Po/^{137}Cs PSD plot of Coumarin-6 shifted 50 wt.% DPA-DHS based plastic.

(going from γ to α excitation) of the scintillation delay for the 50 wt.% DPA-DHS sample was considerably less than that for EJ-299-34, as is shown in Figure 5.7 and Figure 5.8, the relative photomultiplier tube response alone is not enough to explain the poorer performance. As the emission of delayed fluorescence photons depends on the triplet-triplet annihilation process, which in turn depends on the diffusivity of triplet excitons within the material,[5,44] it is possible that a significant difference in triplet diffusivity may be one of the factors responsible for the decreased PSD performance. Given that crystalline 9,10-diphenylanthracene is known to have good PSD performance,[32–34] it is reasonable to presume that if a difference in triplet diffusivity is indeed responsible for the diminished performance, the structural modifications and/or polymer matrix of the DPA-DHS based plastic material are directly involved. Since the time scale for energy transfer from matrix to dye of triplet excitons should be much faster than the diffusion/annihilation process, non-radiative energy transfer to and from diphenylanthracene cores should be the primary mechanism for triplet migration. In this sense, the polymer matrix, as well as the flexible linking groups that bind the diphenylanthracene cores will combine to increase the average diphenylanthracene core spacing, which in general should have the effect of decreasing the efficiency and overall rate of energy transfer, leading to an overall decreased triplet diffusivity. If this hypothesis is
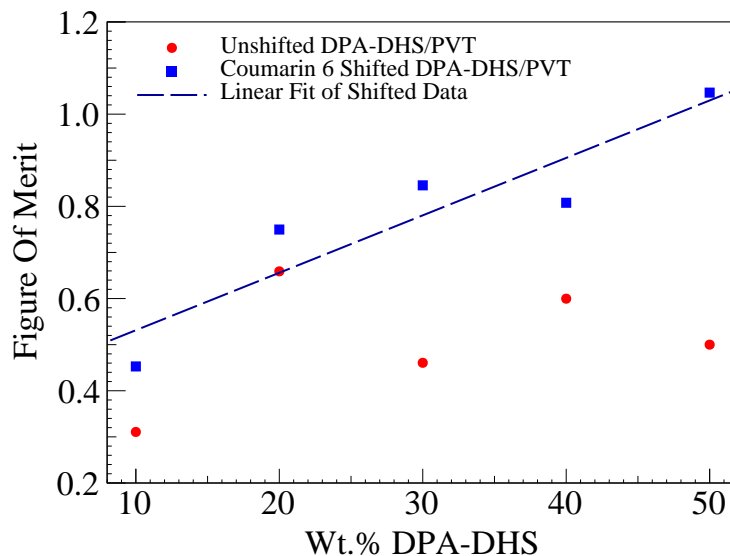
Figure 5.12: PSD figure of merits of both unshifted and Coumarin 6 wavelength shifted samples with DPA-DHS content from 10-50 wt.%.

correct, then it is expected that both a further increase in diphenylanthracene core content, as well as a reduction in the linking group chain length could lead to a significant increase in PSD perfomance. However, both of these measures are problematic in terms of sample preparation; in particular, reduction of the linking group chain length will surely lead to both lower solubility and higher melting point of the dye monomer, making fabrication of such a plastic with even higher loadings even more problematic, if not impossible.

5.9   Conclusions

A novel, highly soluble, and polymerizable diphenylanthracene-based dye (DPA-DHS) was successfully synthesized, and plastic scintillator samples fabricated using this dye monomer were found to be hard, durable, and highly transparent. Dye concentrations of at least 50 wt.% when copolymerized with poly(vinyl toluene) were found to be readily achievable. Of all of the DPA-DHS based plastic compositions tested, the Coumarin 6 wavelength 50 wt.% DPA-DHS was found to have the best performance, albeit notably less than the commercial EJ-299-34 plastic. While the unshifted DPA-DHS based plastic samples did show PSD

properties, the strong effects of self-absorption led to significant loss of performance at the highest DPA-DHS concentrations. While the ultimate performance of the DPA-DHS based plastic material was just below the threshold limit for usability in real detectors, it does serve as a proof-of-concept for the possibility of highly loaded plastics stabilized via copolymerization, the lessons from which can be utilized in the design and synthesis of entirely new classes of dyes for PSD capable plastic scintillators. In doing so, it will be particularly important to focus on the design and synthesis of PSD-capable monomers that have shorter wavelength emission than the DPA-DHS monomer, so that they are compatible with traditional blue/violet emitting wavelength shifters, which is critical to achieving good spectral matching to typical photomultiplier tube photocathodes.

CHAPTER 6

Thermally Activated Delayed Fluorescence Materials for Pulse Shape Discrimination

6.1 Background of Thermally Activated Delayed Fluorescence Dyes

Scintillating dyes currently employed in commercial plastics are conventional fluorescent compounds, which are incapable of harvesting triplet excited states generated by the passage of an incident high energy particle. In the field of organic light emitting diodes (OLEDs), several different approaches have been explored to go beyond the 25% internal quantum efficiency limit of conventional fluorescent dopants, which is imposed by the lack of ability for harvesting triplet excitons. One of the more notable examples is the use of phosphorescent organoiridium complexes in achieving near 100% internal quantum efficiency,[45,46] where the enhanced spin-orbit coupling of the heavy iridium center enables both rapid intersystem crossing from the lowest excited singlet (S_1) to lowest excited triplet (T_1) excited state and direct emission (phosphorescence) from the T_1 state. One of the most popular of such complexes, bis[2-(4,6-difluorophenyl)pyridinato-C^2,N](picolinato)iridium(III) (FIrpic), has also been utilized as a triplet harvesting dye in plastics scintillators, both with and without added γ-sensitizers, and was found to have improved light yield versus comparable samples fabricated with a standard fluorescent scintillating dye.[47] However, because the intersystem crossing from S_1 to T_1 is much faster than direct emission from S_1 (fluorescence), the decay kinetics of typical phosphorescent organoiridium complexes consists of a single lifetime which is totally characteristic of emission from the T_1 state (and is correspondingly on the order of μs's). Consequently, the prospects for use of phosphorescent organoiridium complexes for PSD plastics is severely hindered by the lack of distinct fast and slow decay components.

45

Additionally, iridium is a relatively expensive platinum group element, whose use in plastic scintillators would adversely affect their otherwise low cost. Some effort has been made to overcome these limitations and achieve PSD through the use of quite low phosphorescent dye loadings in conjunction with either host [48] or additional dye emission, [49] but at very low dye loading, energy transfer from the matrix to the emissive dye will be hindered, and correspondingly the light yield of the material will be compromised.

In recent years, there has been a rapidly emerging area of research into 100% internal quantum efficiency organic light emitting diodes, through the use of materials that possess the property of *thermally activated delayed fluorescence* (TADF), also known as "E-type" delayed fluorescence. [50,51] While earlier efforts on developing TADF organic light emitting diodes utilized organometallic complexes of transition metals such as copper, more recent generations of TADF materials have been developed that are completely metal free and have been shown to be capable of near 100% internal quantum efficiency in devices, [52,53] and to have emission wavelengths tunable throughout the entire visible spectrum. [54]

6.2   Application of TADF Dyes to Organic Scintillators

What makes TADF materials particularly attractive for use in plastic scintillators is not only the possibility for enhanced light yield due to triplet harvesting, but that the fluorescence decay of TADF dyes is characterized by two distinct exponential components, a fast component, which is prompt fluorescence directly from the S_1 state and for which lifetimes are on the order of 1-10 ns, and a slow decay component, which originates from T_1 excited states, and whose lifetimes can vary over a wide range but are typically on the order of 1 µs to 1 ms. The presence of two different decay components that are directly related to the respective populations of S_1 and T_1 excited states suggests that TADF could be a highly effective means of achieving good PSD performance.

Figure 6.1 illustrates the energetic levels and overall photophysical processes that occur for both a typical fluorescent dye and a typical TADF dye. The mechanism for triplet harvesting in TADF materials arises from the presence of a small energy difference between
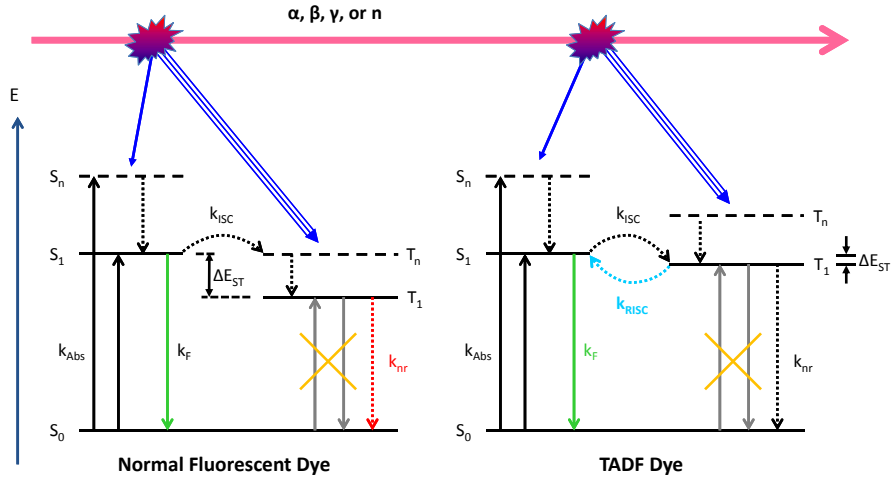
Figure 6.1: Schematic comparison of the energy levels and photophysical processes involved in scintillation from fluorescent and TADF dyes.

the S_1 and T_1 states (ΔE_{ST}), which is typically around $\sim$0.1 eV or less. The small singlet-triplet splitting results in a fast intersystem crossing (ISC) and reverse intersystem crossing (RISC) between the S_1 and T_1 states, which results in their efficient interconversion according to the following equations:

$$S_1 \xrightarrow{k_{ISC}} T_1 \tag{6.1a}$$

$$T_1 \xrightarrow{k_{RISC}} S_1 \tag{6.1b}$$

The presence of a small singlet-triplet splitting does not result in an increased probability of phosphorescence from the T_1 state, and thus all of the emission from the dye is due to the fluorescence from the S_1 state. However, repopulation of S_1 states from the T_1 level is an endothermic process with an activation energy of ΔE_{ST}, and consequently the rate constant for reverse intersystem crossing (k_{RISC}) is considerably less than that of fluorescence (k_F) and non-radiative recombination (k_{nr}), which results in the slow decay lifetime that is characteristic of TADF materials. A key feature of the TADF mechanism is that conversion of triplet to singlet excitons is a unimolecular process, which is in direct contrast to the triplet-triplet annihilation process of the conventional high dye loading approach for achieving PSD

47

in plastics. This is quite promising, as it suggests that in principle good PSD behavior may be achieved via TADF without the need for a high dye loading, and instead dye loading can be kept within a range that will maximize the light yield of the material.

In order for a TADF dye to be useful as a scintillating dye, several criteria not necessarily held in place for organic light emitting diode dyes must also be met. As was mentioned in Chapter 5, scintillating dyes with blue to violet emission color are needed to ensure optimal matching to the spectral response of typical photomultiplier tubes. Since most organic light emitting diode materials are designed with display applications in mind, there are fewer examples of truly deep blue or violet emission, where typical photomultiplier tube quantum efficiencies are greatest. In addition, it will be critical to ensure that the slow decay component lifetime be not more than a few microseconds, otherwise the dye will be effectively unsuitable for use in actual materials, since the long pulse tails would lead to excessive pulse pile-up, severely limiting the useful count rates in real-world detection scenarios. Finally, photoluminescence quantum yields (Φ_{PL}) for TADF materials tend to be notably lower than traditional scintillating dyes (with near unity fluorescence quantum yields), which is a problem that is inherent to the design and properties of TADF dyes.[51] Since high photoluminescence quantum yield is a critical factor in achieving good light yields, and in turn good PSD performance, identification of TADF dyes that can simultaneously satisfy all of these criteria is especially challenging.

6.3 Design and Synthesis of Candidate TADF Dyes for Plastic Scintillators

Of the various broad structural categories of blue emitting TADF dyes, derivatives of diphenyl sulfone are of particular interest, primarily due to strongly electron withdrawing nature of the sulfone moeity. Table 6.1 lists some of the basic photophysical properties of diphenyl sulfone and corresponding derivatives whose use as TADF dyes have been reported in literature. Diphenyl sulfone itself (Entry 6.1-B) has a fairly large HOMO-LUMO gap, as evidenced by the short wavelength absorption and emission that is only marginally red-shifted from

the lowest absorbance and fluorescence peaks of benzene (Entry 6.1-A). This is a beneficial property for designing TADF dyes with large HOMO-LUMO gaps, since introduction of the sulfone moeity does not result in any significant increase in conjugation length, at least for the electron withdrawing segment.

By far the most common means of connecting an electron donating group to the parent diphenyl sulfone moeity in literature compounds is via aromatic amines, typically either diphenylamine or carbazole and their respective derivatives, and all of TADF dyes shown in Table 6.1 employ either the Donor-Acceptor (D-A) or Donor-Acceptor-Donor (D-A-D) design motif. From Entry 6.1-E and Entry 6.1-G, it can be seen that introduction of these aromatic amines significantly decreases the HOMO-LUMO gap as compared to unfunctionalized diphenyl sulfone, which is not surprising given that the absorption and emission wavelengths of the parent amines, triphenylamine (Entry 6.1-C) and phenylcabazole (Entry 6.1-D), respectively, have notably longer emission wavelengths as compared to diphenyl sulfone. Triphenylamine has both shorter absorption and longer emission wavelengths as compared to phenylcarbazole, the former of which can be accounted for due to longer conjugation length of the carbazole moeity, while the latter is likely due to the increased flexibility of triphenylamine, which allows for greater geometrical relaxation before emission. The diphenyl sulfone derivatives substituted with these amines, Entry 6.1-E and Entry 6.1-H, both have emission maxima around 400 nm, which is roughly the lower limit of the TADF dyes listed in Table 6.1, although the addition of *tert*-butyl groups to the diphenylamine moeities somewhat raised the emission of Entry 6.1-F, presumably due to the electron donating ability of the *tert*-butyl side-groups. Notably, monosubstitution of the diphenyl sulfone core, such as in Entry 6.1-I and Entry 6.1-J does not lead to any notable reduction in the respective HOMO-LUMO gaps, which would suggest that the overall magnitude of the HOMO-LUMO gap in these systems is mediated by both the presence of the arylamine moeity, as well as the electron withdrawing effect exerted on it by the arylsulfone acceptor group. Another noticeable trend is that there is a slight increase in the HOMO-LUMO gap when the arylamine is substituted at the *meta*-position relative to the sulfone, such as for Entry 6.1-J and Entry 6.1-K, as compared to their *para*-substituted counterparts (Entry 6.1-I and Entry 6.1-

Table 6.1: Structures and spectral/photoluminescence data of diphenylsulfone-based TADF dyes selected from literature, along with their corresponding parent compounds for comparison; except where indicated, all data listed were obtained by the respective authors as dilute solutions in toluene.

Entry	Structure	λ_{Abs} (nm)	λ_F (nm)	Φ_{PL}	τ_{slow} (μs)	ΔE_{ST} (eV)	Ref.
6.1-A		268[a,b]	271[a,b]	0.07[b]	–	–	55
6.1-B	DPS	270[a,c]	285[a,b]	0.10[b]	–	–	56
6.1-C		300[a,b]	355[a,b]	0.03[b]	–	–	55
6.1-D	PhCz	340[a,b]	344[a,b]	0.37[b]	–	–	55
6.1-E		–	402	0.57	90	0.54	56
6.1-F		–	419	0.65	140	0.45	56
6.1-G		345,[a,d] 340[a]	405,[a,d] –	–	–	–	57, 58
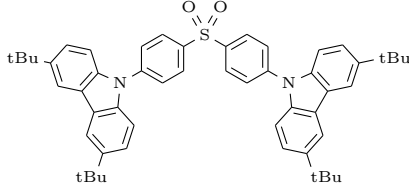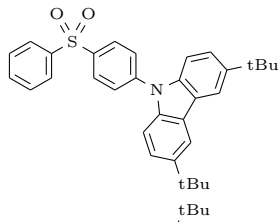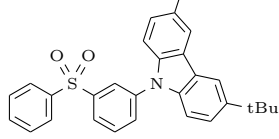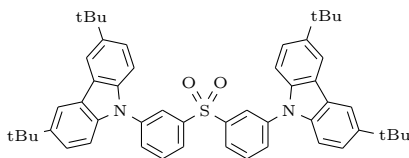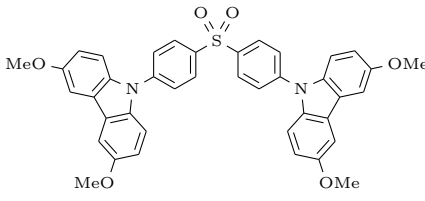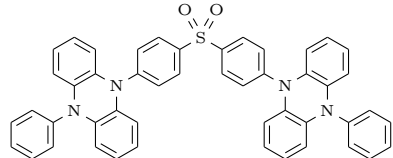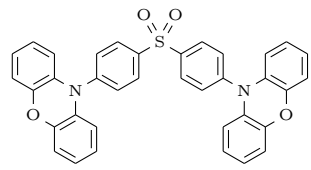
[a]Approximated from a spectral plot.
[b]Dilute solution in cyclohexane.
[c]Dilute solution in ethanol.
[d]Thin film.
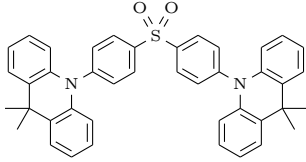
Table 6.1 — continued from previous page

Entry	Structure	$\lambda_{\mathbf{Abs}}$ (nm)	$\lambda_{\mathbf{F}}$ (nm)	$\Phi_{\mathbf{PL}}$	τ_{slow} (µs)	$\Delta E_{\mathbf{ST}}$ (eV)	Ref.
6.1-H	**DTC-DPS**	–, 345	404	0.69	270, 250	0.32, 0.33[e]	56, 59
6.1-I		344	406	0.59	234	0.39[e]	59
6.1-J		342	414	0.51	258	0.24[e]	59
6.1-K		342	422	0.66	285	0.32[e]	59
6.1-L	**DMOC-DPS**	370	445	0.56	93	0.24	60
6.1-M	**PPZ-DPS**	510	580	0.03	0.28	0.09	61
6.1-N	**PXZ-DPS**	454	507	0.81	2.5	0.08	61

[e]DFT/TD-DFT calculated.

Table 6.1 — continued from previous page

Entry	Structure	$\lambda_{\mathbf{Abs}}$ (nm)	$\lambda_{\mathbf{F}}$ (nm)	$\Phi_{\mathbf{PL}}$	τ_{slow} (µs)	$\Delta\mathbf{E_{ST}}$ (eV)	Ref.
6.1-O	DMAC-DPS	413	460	0.80	7.1	0.09	61

H, respectively). The major consequence of the roughly 400 nm lower limit on emission wavelength is that while the diphenylsulfone/arylamine systems can yield dyes with deep blue to violet emission, the eventual need for wavelength shifting to maximize photon collection efficiency in actual detectors will result in further redshifting of the plastic's emission maximum outside the optimal range for readout with conventional photomultiplier tubes.

Many of the same factors that can be seen to influence the magnitude of the HOMO-LUMO gaps in the compounds listed in Table 6.1 also have important effects on the key parameter for a TADF dye, namely its singlet-triplet splitting. Substitutional patterns can have some effect on the singlet-triplet splitting, as can be seen from the (density-functional theory calculated) lower singlet-triplet splitting of *meta*-substituted Entry 6.1-J as compared to its *para*-substituted isomer Entry 6.1-I, but this relation does not hold true when comparing the calculated singlet-triplet splittings of Entry 6.1-H and Entry 6.1-K, which are approximately equal. The electron donating ability of the donor groups can be seen to have a much more profuound effect on the observed singlet-triplet splittings. The greater electron donating ability of the methoxy groups in Entry 6.1-L results in a reduced singlet-triplet splitting as compared to the *tert*-butyl groups of Entry 6.1-H, and the reduction in singlet-triplet splitting is even greater for the highly electron donating 5,10-dihydro-5,10-diphenylphenazine (PPZ), 10*H*-phenoxazine (PXZ), and 9,10-dihydro-9,9-dimethylacridine (DMAC) donor groups which are present in Entry 6.1-M (PPZ-DPS), Entry 6.1-N (PXZ-DPS), and Entry 6.1-O (DMAC-DPS), repsectively. These last three TADF dyes additionally possess the fastest slow-decay lifetimes of any of the compounds listed in Table 6.1; all three are less than 10 µs (a plausible range for scintillation applications), and PPZ-DPS in particular has

Para-*t*Butyl-Dye   **Meta-*t*Butyl-Dye**
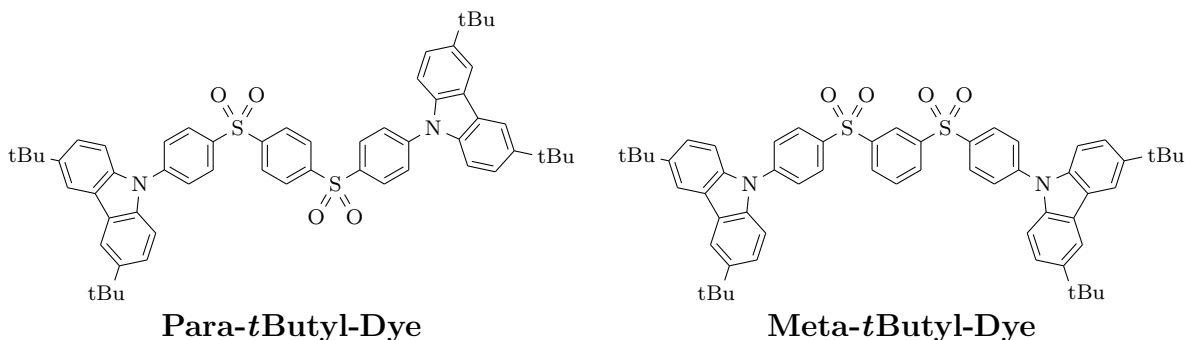
Figure 6.2: Structures of an isomeric pair of bis(phenylsulfonyl)benzene-based TADF dyes found to have optimal spectral and electronic properties for potential scintillator applications.[62]

Compound	λ_{Abs} (nm)	λ_{F} (nm)	Φ_{PL}	τ_{slow} (µs)	ΔE_{ST} (eV)
Para-*t*Butyl-Dye	295, 363	446	0.563[a]	1.23[b]	0.05[c]
Meta-*t*Butyl-Dye	293, 348	422	0.693[a]	1.16[b]	0.24[c]

[a]Dilute solution in chloroform. [b]Thin film in bis[2-(diphenylphosphino)phenyl]ether oxide (DPEPO). [c]Dilute solution in dichloromethane.

Table 6.2: Reported spectral and photophysical properties of the bis(phenylsulfonyl)benzene-based TADF dyes depicted in Figure 6.2; except where indicated, all data listed were obtained by the respective authors as dilute solutions in toluene.[62]

a remarkably short, sub-µs slow-decay lifetime, however, both its red emission and very low photoluminescence quantum yield rule out any practical use for this dye. Both PXZ-DPS and DMAC-DPS have photoluminescence quantum yields close to 0.8, significantly better than PPZ-DPS, and while the slow-decay lifetime of PXZ-DPS is faster than DMAC-DPS, its green emmision color also hinders its suitability as a scintillating dye.

Recently, Liu et al. have reported a pair of isomeric TADF dyes based on central bis-(phenylsulfonyl)benzene acceptors,[62] whose structures are shown in Figure 6.2, and whose key spectral and photophysical properties are summarized in Table 6.2. Both of these dyes possess a number of the desired physical properties detailed in Section 6.2, namely deep blue

emission color, moderately high photoluminescence quantum yields, very fast $\tau_{slow} \sim 1$ µs, and small singlet-triplet splittings. The key structural difference between these dyes and those listed in Table 6.1 is the bis(phenylsulfonyl)benzene acceptor core, which while larger than a simply diphenyl sulfone acceptor core, does not result in a substantial increase in the HOMO-LUMO gaps of the dyes in Table 6.2. This lack of large increase in the HOMO-LUMO gaps is due to the fact that the tetrahedral sulfone groups electronically isolate the aromatic fragments from one another, preventing a large increase in effective conjugation length that would dramatically reduce the HOMO-LUMO gap (this is the same reason that the HOMO-LUMO gaps of benzene (Entry 6.1-A) and diphenyl sulfone Entry 6.1-B are very similar to one another). The two isomers vary structurally from one another via the substitutional pattern of the central benzene ring by the flanking sulfone groups; the isomer with the two sulfones in a 1,4-relation (i.e., *para*) to one another is abbreviated as Para-*t*Butyl-Dye, while the isomer with the sulfones in a 1,3-relation (i.e., *meta*) is abbreviated Meta-*t*Butyl-Dye. As can be seen from comparison with Entry 6.1-H, the largest increase in HOMO-LUMO gap is for Para-*t*Butyl-Dye (~ 40 nm), and the increase is less so for Meta-*t*Butyl-Dye (~ 20 nm), which also possesses a greater photoluminescence quantum yield and shorter slow-decay lifetime than its isomer, Para-*t*Butyl-Dye, although the values are still relatively close to one another for both of these later two properties. In fact for scintillation applications, Meta-*t*Butyl-Dye is a seemingly better TADF dye candidate in all regards, except for the fact that Para-*t*Butyl-Dye posses a markedly smaller singlet-triplet splitting.

Due to their advantageous spectral and photophysical properties (especially when compared to the other TADF dyes listed in Table 6.1), the Para-*t*Butyl-Dye/Meta-*t*Butyl-Dye dye pair was readily chosen as an ideal candidate TADF system to determine the applicability of TADF dyes and their corresponding photophysical processes towards scintillator applications. While these dyes do possess some shortcomings in terms of an ideal scintillating dye, most notably their less than ideal photoluminescence quantum yields (conventional fluorescent scintillating dyes typically have $\Phi_{PL} \sim 1$), their capability for TADF and their very fast slow-decay lifetimes make them among the only known TADF materials that are plausible candidates for use as scintillating dyes. In addition, the marked (but not excessive) difference

Para-Octyl-Dye   **Meta-Octyl-Dye**
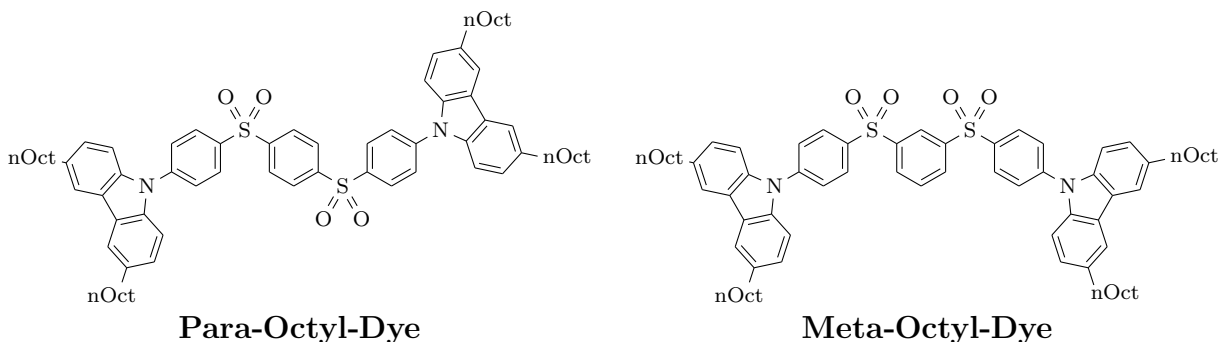
Figure 6.3: Structures of the bis(phenylsulfonyl)benzene-based TADF dyes modified with long octyl chains for enhanced solubility in scintillating plastics.

in singlet-triplet splitting between the two dyes allows for assessment of the impact of this key TADF parameter on the ultimate scintillation performance. With these factors in mind, quantities of both Para-*t*Butyl-Dye and Meta-*t*Butyl-Dye were synthesized, but ultimately it was determined that neither dye possessed sufficient solubility in typical scintillating plastics (i.e., poly(vinyl toluene)) or the corresponding liquid monomers to allow for sample fabrication. As such, the structures of both dyes were modified via replacement of the pendant *tert*-butyl groups with long octyl chains to enhance overall solubility. The structures of the modified dyes are shown in Figure 6.3, and the synthesis of both the *tert*-butyl and octyl variants of each respective isomer is detailed in Appendix A. For these new structures, the *para*-isomer is correspondingly abbreviated Para-Octyl-Dye, while the *meta*-isomer is abbreviated as Meta-Octyl-Dye. Both of these enhanced-solubility dyes as-synthesized were found to be foamy (possibly amorphous) solids which were found to be highly soluble in various organic solvents, and were easily purifiable via flash chromatography.

6.4 Spectral and Photophysical Properties of the TADF Scintillating Dyes

In order to fully assess the effects of the structural modifications on the optoelectronic properties of the TADF scintillating dyes detailed in Section 6.3, detailed studies of the absorbance and photoluminescence spectra of these dyes within a wide range of different

media and conditions were carried out. In general, the majority of the spectral properties for the enhanced solubility dyes (Meta-Octyl-Dye and Para-Octyl-Dye) demonstrated only minor differences as compared to their unmodified forms (Meta-tButyl-Dye and Para-tButyl-Dye, respectively), but some notable differences were identified. However, for the most part the absorbance and photoluminescence spectra of a given octyl-substituted dye closely match its unmodified counterpart, which indicates that replacement of the $tert$-butyl groups for the longer octyl chains has very little impact to the overall electronic properties of the dye molecule. This is not surprising, since while a $tert$-butyl group has slightly more electron donating character than a straight alkyl chain, the overall difference is quite low, and any observed change is more likely to due to steric and/or solvent interaction effects, which could lead to alteration of the equilibrium geometry of the aromatic core structures, which in turn would affect the relative energies of the HOMO/LUMO orbitals.

The spectral properties of the TADF dyes were generally found to be strongly influenced by the surrounding chemical environment. In particular, all of the dyes demonstrated marked positive solvatochromic behavior, which can easily be seen for both of the pairs of the $meta$- and $para$-substituted isomers that are shown in both Figure 6.4 and Figure 6.5. For one of the solvents, cyclohexane, Para-tButyl-Dye was found to be soluble only in exceedingly trace amounts, preventing spectral measurements, and thus the data in Figure 6.5 shows only that of its solubilized counterpart, Para-Octyl-Dye. While the solvatochromic effects are most dramatic in the photoluminescence spectra (Figures 6.4(b) and 6.5(b)), more subtle shifts are still observable in the absorbance spectra (Figures 6.4(a) and 6.5(a)), particularly for the onsets of the $S_0 \rightarrow S_1$ absorption bands. Comparison of the spectra in non-polar solvents such as cyclohexane and toluene shows little change in their absorption onsets, whereas more polar solvents such as chloroform or tetrahydrofuran (THF) show noticeable shifts. Interestingly, while the hypsochromic shifts observed in tetrahydrofuran solutions are easily accounted for due to the increased stabilization of the polar sulfone groups in the ground state of the dye molecules dissolved in a polar solvent, leading to a larger $S_0 \rightarrow S_1$ transition energy, the bathochromic shift observed in chloroform solutions would seemingly indicate that the dye ground states in this solvent are actually destabilized somewhat relative to
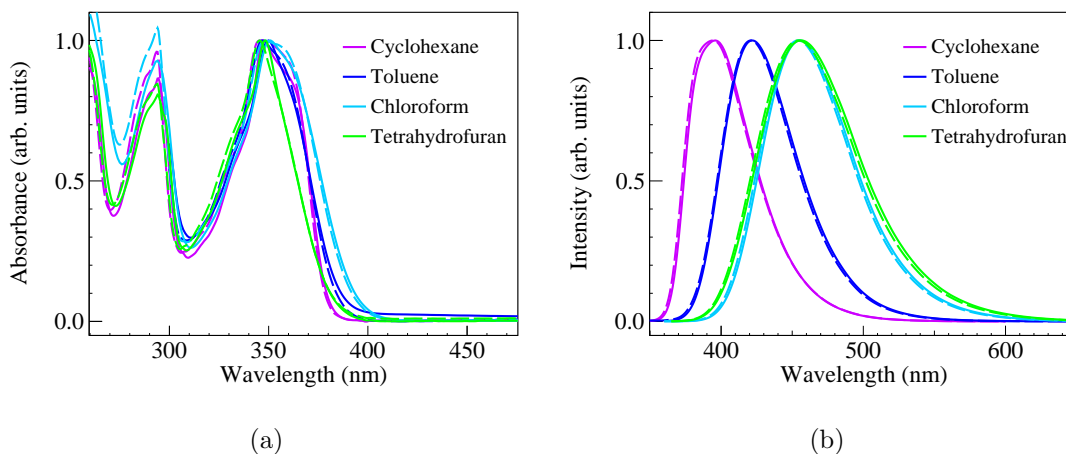
Figure 6.4: Overlaid comparisons of the (a) absorbance and (b) photoluminescence spectra of dilute solutions of Meta-*t*Butyl-Dye (dashed) and Meta-Octyl-Dye (solid).
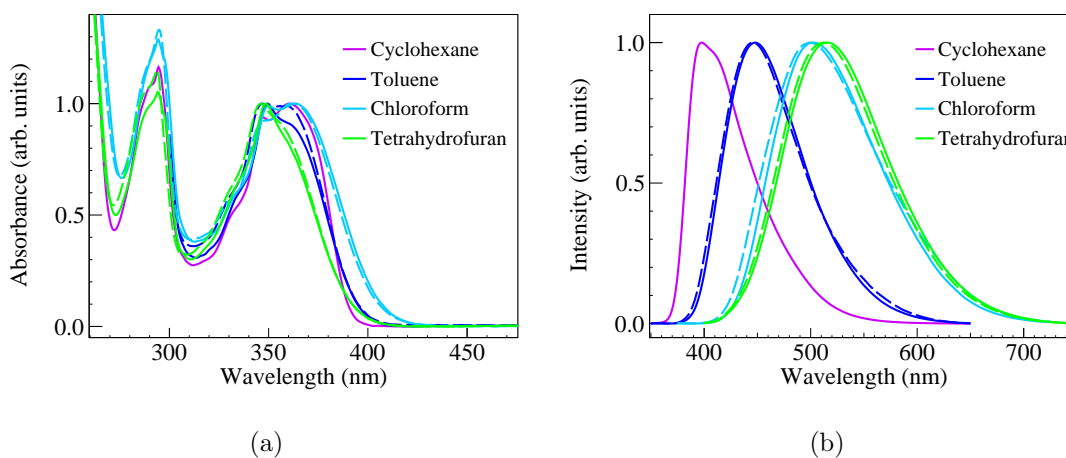
Figure 6.5: Overlaid comparisons of the (a) absorbance and (b) photoluminescence spectra of dilute solutions of Para-*t*Butyl-Dye (dashed) and Para-Octyl-Dye (solid).

the non-polar solvents. This latter observation would suggest that factors other than simply solvent polarity alone are involved in determining the overall solvated ground state energy for these dyes. From a practical standpoint, however, the shifts observed in the absorption bands with changing solvent are relatively minor, and would not be expected to have much impact in determining their overall suitability as scintillating dyes in various media, especially since the emission characteristics of the dyes are affected to a much greater extent. Unlike the absorption spectra, the photoluminescence spectra all show significant bathochromic shifts

in the dye emission with increasing solvent polarity. Given that the excited states of TADF molecules are highly charge transfer in nature,[51] the excited states should posses a high degree of dipolar character which can be stabilized by solvent interaction in polar media. The bathochromic shift is less pronounced for the *meta*-substituted dyes (Figure 6.4(b)), whose emission shifts over the range from ca. 390–460 nm, with very little additional shift observed going from mildly polar chloroform to more polar tetrahydrofuran, although the emission band in the later solvent is further broadend. The *para*-subsituted dyes (Figure 6.5(b)), on the other hand, display a much larger bathochromic shift over the range from ca. 400–520 nm, which would indicate a markedly higher degree of dipolar character for the S_1 excited states of these dyes.

Since the TADF mechanism critically depends on the value of the singlet-triplet splitting of a given dye, it is important to fully assess the effect that the solvent enviroment — the polarity in particular — may have in establishing the precise singlet-triplet splitting of the TADF dye within the overall dye/matrix system. The literature values of 0.24 and 0.05 eV for the singlet-triplet splitting of Meta-*t*Butyl-Dye and Para-*t*Butyl-Dye, respectively (as listed in Table 6.2) were recorded by the authors as solutions in dichloromethane,[62] which has a markedly greater degree of dipolar character than a nonpolar aromatic plastic such as poly(vinyl toluene). Thus, better determination of the electronic properties of the TADF dyes dissolved in a range of solvent polarities is useful to understanding the impacts of solvent environment on the magnitude of the observed singlet-triplet splitting values for the particular dyes in question, and to better assess the true singlet-triplet splitting value for non polar aromatic media such as poly(vinyl toluene). Figure 6.6 and Figure 6.7 show the measured low temperature (77K) fluorescence and phosphorescence spectra obtained for three solvents, methylcyclohexane, toluene, and 2-methyltetrahydrofuran (2-MeTHF), which approximately span the same polarity range as the room temperature fluorescence spectra of Figures 6.4 and 6.5. Like for the case of Figure 6.5, only the spectra for Para-Octyl-Dye is given in Figure 6.7(a), due to the lack of solubility of Para-*t*Butyl-Dye in methylcyclohexane. Unlike the room temperature emission spectra, the low temperature fluorescence and phosphorescence spectra showed significantly more dramatic shifts and/or differences in the

(a) Methylcyclohexane

(b) Toluene

(c) 2-Methyltetrahydrofuran
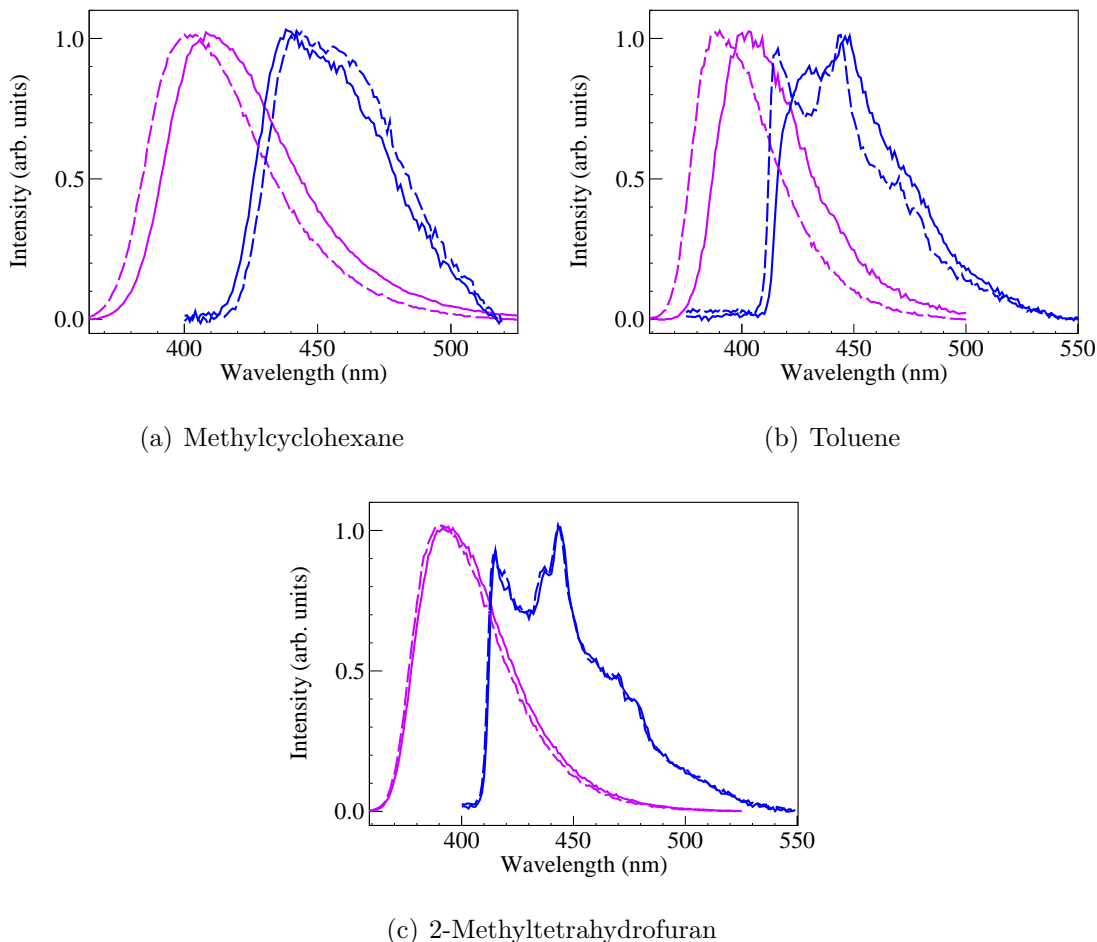
Figure 6.6: Low temperature (77 K) fluorescence (violet) and phosphorescence (blue) spectra of dilute solutions of Meta-tButyl-Dye (dashed) and Meta-Octyl-Dye (solid) in the indicated solvents.

position and population of vibronic sublevels between the *tert*-butyl- and octyl-substituted counterparts. In addition, the direction and magnitude of these shifts was not found to neatly correspond to that expected for effects solely attributable to solvatochromic behavior. A generally consistent observation was that the low temperature fluorescence spectra of the octyl-substituted dyes were redshifted at least to some degree compared to their *tert*-butyl-substituted counterparts, which as discussed was also observed to a small degree in the room temperature data of Figures 6.4(b) and 6.5(b), but specific low temperature examples such as Figures 6.6(a), 6.6(b) and 6.7(b) show larger shifts in the range of 4–12 nm. Like the room temperature spectra, these are likely attributable to increased solvent interaction

(a) Methylcyclohexane

(b) Toluene

(c) 2-Methyltetrahydrofuran
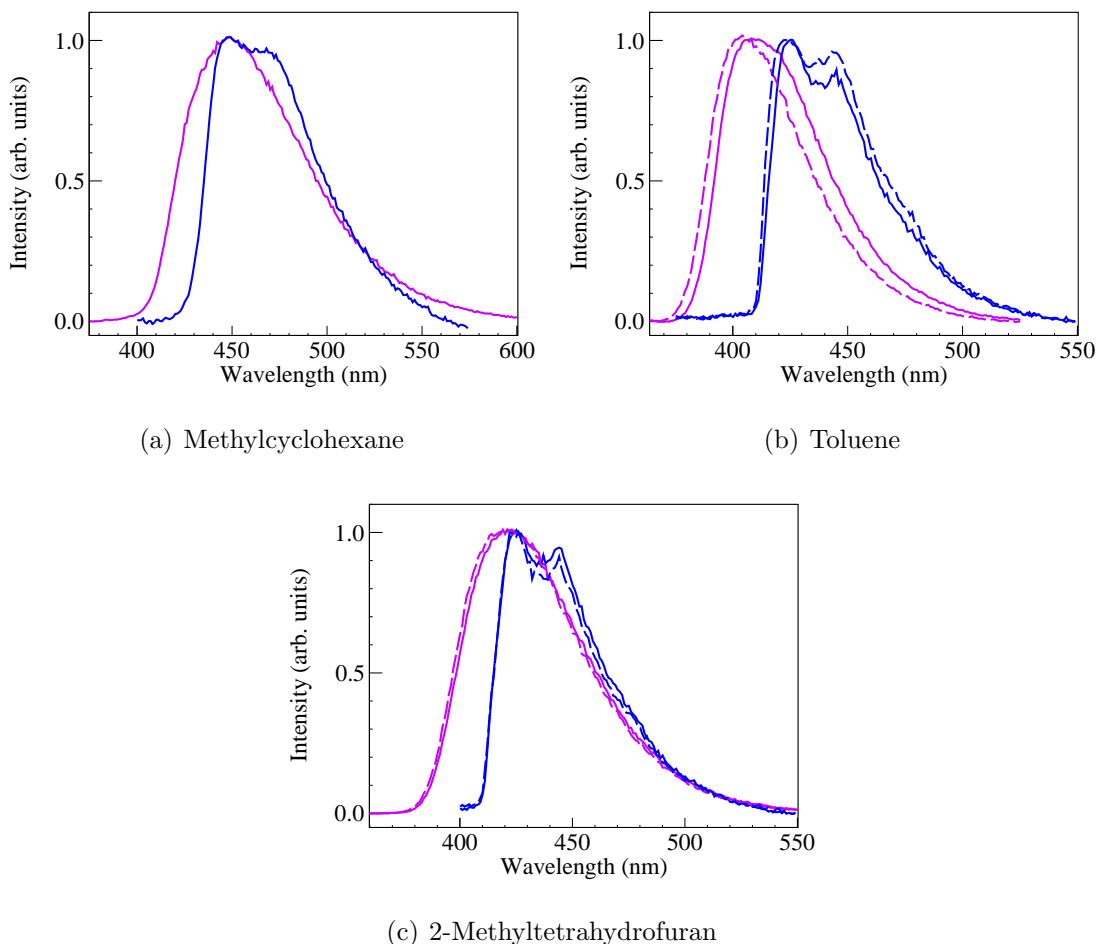
Figure 6.7: Low temperature (77 K) fluorescence (violet) and phosphorescence (blue) spectra of dilute solutions of Para-tButyl-Dye (dashed) and/or Para-Octyl-Dye (solid) in the indicated solvents.

of the octyl side chains, which is enhanced to a degree at lower temperatures, possibly due to entropic and/or steric factors. On the other hand, the spectra in the more polar 2-methyltetrahydrofuran showed very little shift in the low temperature fluorescence between the *tert*-butyl- and octyl-subsituted dyes, which would suggest that the dipolar interactions influencing the relaxation of the S_1 states are the dominant factors in more polar solvents. In addition, less obvious is any discernible trend in observable shifts in the phosphorescence spectra between the *tert*-butyl- and octyl-subsituted dyes. Some redshifting of the phosphorescence is seen for Meta-Octyl-Dye in methylcyclohexane (Figure 6.6(a)), however, in toluene (Figure 6.6(b)) the Meta-Octyl-Dye phosphorescence is actually blue shifted relative

to Meta-*t*Butyl-Dye. In addition, no net shift is seen in the phosphorescence of Para-Octyl-Dye in Figure 6.7(c), which did display redshifting of its low temperature fluorescence at least in toluene (Figure 6.7(b)).

The emission wavelengths of the fitted $0 \to 0$ sub-bands and the corresponding calculated singlet-triplet splitting values from all of the low temperature spectra shown in Figures 6.6 and 6.7, along with a summary of all of the important data obtained from the room temperature solution spectra presented in Figures 6.4 and 6.5, and additional photoluminescence quantum yield (Φ_{PL}) measurements are listed in Table 6.3. The photoluminescence quantum yields for all of the TADF dyes were measured in toluene, in order to closely simulate the polarity and electronic character of a scintillating plastic such as poly(vinyl toluene). Overall, very little difference in the measured photoluminescence quantum yield values was observed between the *tert*-butyl- and octyl-substituted variants of each dye pair, with the *meta*-subsituted dyes having $\Phi_{PL} \simeq 0.7$ and the *para*-subsituted dyes having $\Phi_{PL} \simeq 0.6$. The photoluminescence quantum yield values are in good agreement with the literature photoluminescence quantum yields reported for solutions of the *tert*-butyl-substituted variants in chloroform that are listed in Table 6.2. The fact that no major change in photoluminescence quantum yield was observed for either dye pair upon replacement of the side-chains further indicates that replacement of the *tert*-butyl groups in these dyes led to minimal perturbation of their photophysical properties.

On account of shifts in the positions of the $0 \to 0$ bands for both the low temperature fluorescence and phosphorescence spectra, the obtained values of the singlet-triplet splittings listed in Table 6.3 for a given dye do show some variance with solvent, but the combined individual effects from each emission spectrum do not result in any discernible trend in the singlet-triplet splitting values with solvent polarity. On the other hand, two notable trends can be gleamed from the singlet-triplet splittings presented in Table 6.3, the most obvious being that the *para*-substituted isomers of the dyes in all solvents demonstrated lower singlet-triplet splittings as compared to their *meta*-substituted variants, as was the case for the literature singlet-triplet splitting values listed in Table 6.2 for the *tert*-butyl-substituted dyes in dichloromethane. The second notable observation is that for every solvent tested,

Table 6.3: Summary of the measured photophysical data for dilute solutions of the TADF scintillating dyes investigated in this work. For absorbance and photoluminescence measurements taken at 300 K, λ_{Abs} and λ_F are defined as the maxima of the spectral bands corresponding to the $S_0 \rightarrow S_1$ and $S_1 \rightarrow S_0$ transitions, respectively. For photoluminescence measurements taken at 77 K, λ_F and λ_{Ph} are defined as the peak wavelengths of the $0 \rightarrow 0$ vibrational sub-bands obtained via fitting of the spectral bands corresponding to the $S_1 \rightarrow S_0$ and $T_1 \rightarrow S_0$ transitions, respectively, which are used to calculated the listed values of ΔE_{ST}. Abbreviations for solvents are: MeCy = Methylcyclohexane, THF = Tetrahydrofuran, 2-MeTHF = 2-Methyltetrahydrofuran.

Compound	Solvent	Temp. (K)	λ_{Abs} (nm)	λ_F (nm)	λ_{Ph} (nm)	Φ_{PL}	ΔE_{ST} (eV)
Meta-tButyl-Dye	Cyclohexane	300	347	394	–	–	–
	MeCy	77	–	392	434	–	0.33
	Toluene	300	347	421	–	0.680	–
		77	–	383	415	–	0.25
	Chloroform	300	348	454	–	–	–
	THF	300	346	454	–	–	–
	2-MeTHF	77	–	381	414	–	0.26
Meta-Octyl-Dye	Cyclohexane	300	348	396	–	–	–
	MeCy	77	–	400	435	–	0.25
	Toluene	300	350	422	–	0.708	–
		77	–	396	418	–	0.17
	Chloroform	300	351	456	–	–	–
	THF	300	348	457	–	–	–
	2-MeTHF	77	–	382	414	–	0.25

Table 6.3 — continued from previous page

Compound	Solvent	Temp. (K)	λ_{Abs} (nm)	λ_F (nm)	λ_{Ph} (nm)	Φ_{PL}	ΔE_{ST} (eV)
Para- tButyl-Dye	Toluene	300	347	446	–	0.604	–
		77	–	394	415	–	0.16
	Chloroform	300	362	500	–	–	–
	THF	300	346	512	–	–	–
	2-MeTHF	77	–	404	418	–	0.10
Para-Octyl- Dye	Cyclohexane	300	361	398	–	–	–
	MeCy	77	–	425	441	–	0.11
	Toluene	300	350	448	–	0.590	–
		77	–	397	415	–	0.14
	Chloroform	300	364	502	–	–	–
	THF	300	349	516	–	–	–
	2-MeTHF	77	–	404	415	–	0.08

the singlet-triplet splitting values measured for the octyl-subsituted dyes were lower than their *tert*-butyl-subsituted counterparts. Given the fact that at least some redshifting of fluorescence was observed in virtually every case for the octyl-substituted dyes, it can be clearly seen that the redshift in the fluorescence is the major contributing factor to the reduction in the singlet-triplet splitting for the octyl-substituted dyes. Moreover, since this redshifting in some cases was noticeably enhanced at low temperature, it does remain an open question whether the lower singlet-triplet splitting values measured for the octyl-subsituted dyes are indeed valid for solutions at room temperature, where the overall redshifting due to the difference in sidechains is minimized, especially if the redshifting of the fluorescence is primarily attributable to molecular reorganization driven by entropic and/or steric effects due to the flexible octyl side chains that are enhanced at low temperature. On the other hand, the rigid environment of a plastic matrix to some extent resembles the frozen solvent in the low temperature solution, and thus its not unreasonable to view the singlet-triplet

splitting values of the toluene solutions listed in Table 6.3 as good approximations of the true singlet-triplet splitting values for the octyl-subtutued dyes in a typical scintillating plastic such as poly(vinyl toluene).

The fact that the wavelengths of the photoluminescence from these TADF dyes are so strongly influenced by the polarity of their dissolved medium suggests that the exact nature of the chemical environment when dissolved in typical scintillating plastics could have a discernible effect on the overall scintillation performance. More specifically, as the TADF dyes themselves possess a fair degree of polar character due to their constituent sulfone groups, it would be expected that shifts in the emission wavelengths would occur due to varied degrees of polar interactions with neighboring dye molecules, as would be the case when the overall dye content is varied within the total composition of the plastic. Primary scintillating dyes are typically employed at loadings in excess of 1 wt.% in the bulk plastic, and at these concentrations, the average spacing between neighboring dye molecules could presumably be short enough to allow for intermolecular electrostatic interaction in a similar fashion to solvent-solute interaction, which for a polar solute molecule has the net effect of increasing somewhat the net bulk dipole moment felt by an individual dye molecule. In monolithic samples used in actual scintillation testing, the effects of self absorption (especially at higher dye loadings) significantly complicate the determination of the true molecular emission properties of the dye within a given plastic composition. As such, drop-cast films of Meta-Octyl-Dye and Para-Octyl-Dye dispersed in poly(vinyl toluene) were prepared and kept sufficiently thin to achieve close approximation to the true molecular absorption and emission, and the corresponding spectra are shown in Figure 6.8 and Figure 6.9, respectively.
The loading ranges used for the thin film studies was chosen to directly correspond to the monolithic scintillator samples whose fabrication and spectral properties are discussed in Section 6.5. Little if any shift in the $S_0 \rightarrow S_1$ absorption bands of the Meta-Octyl-Dye in poly(vinyl toluene) and Para-Octyl-Dye in poly(vinyl toluene) films with changing dye content can be seen in Figure 6.8(a) and Figure 6.9(a), respectively. The most notable feature of the absorbance spectra of these films is a moderate broadening of the the $S_0 \rightarrow S_1$ absorption band for the Para-Octyl-Dye in poly(vinyl toluene) samples, and this increases
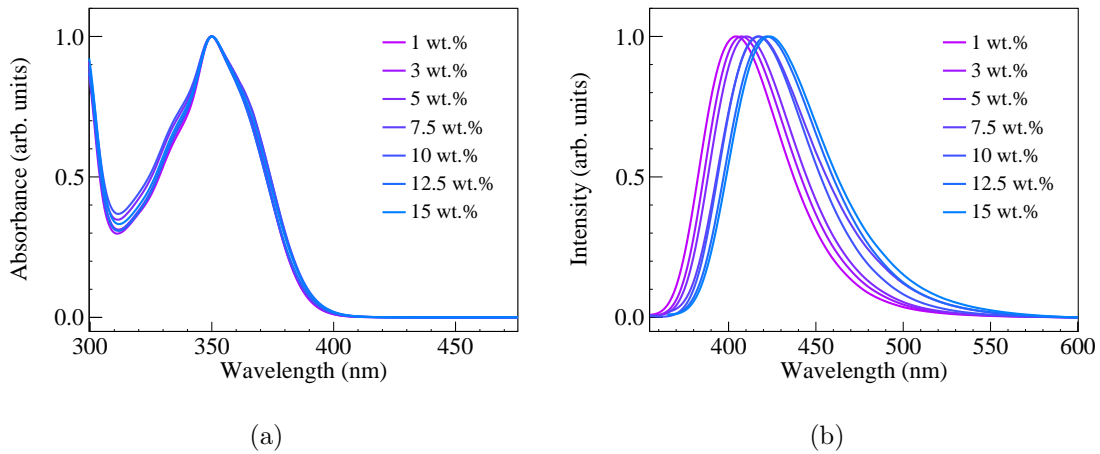
Figure 6.8: (a) UV/Vis absorbance and (b) photoluminescence spectra of thin films of 1-15 wt.% Meta-Octyl-Dye in poly(vinyl toluene).
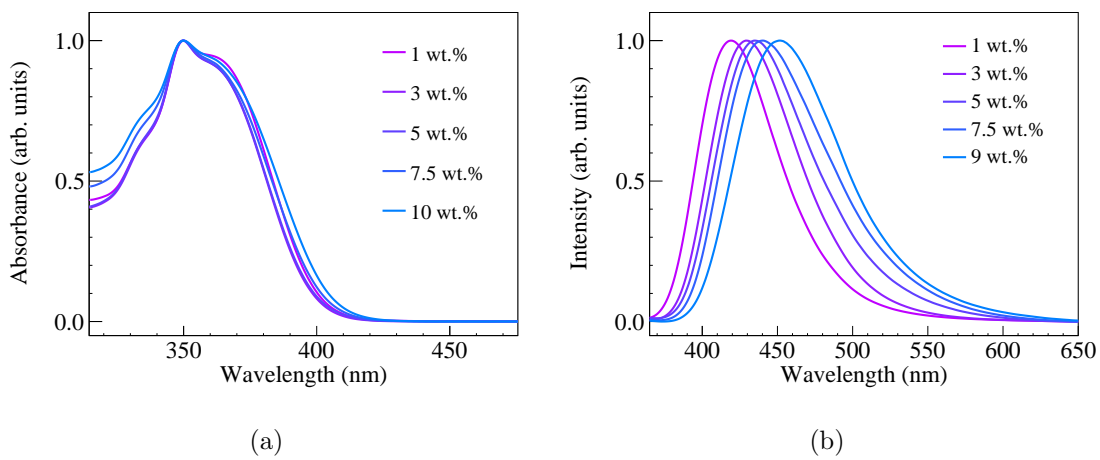
Figure 6.9: (a) UV/Vis absorbance and (b) photoluminescence spectra of thin films of 1-9 wt.% Para-Octyl-Dye in poly(vinyl toluene).

somewhat the relative amount of absorption at wavelengths greater than 400 nm, which will likely effect the observed coloration of monolithic Para-Octyl-Dye in poly(vinyl toluene) samples at higher dye loadings. It should be noted that in comparison, Meta-Octyl-Dye in poly(vinyl toluene) films demonstrated much lower absorbance at wavelengths greater than 400 nm, although there is some finite absorbance which is able to contribute to coloration in the monolithic samples.

The primary observances of solvatochromic effects in these films are found in the photolu-

minescence spectra, and similarly to the solution based data shown in Figures 6.4 and 6.5, the spectra of Meta-Octyl-Dye in poly(vinyl toluene) films (Figure 6.8(b)) overall display less pronounced solvatochromic effects as compared to Para-Octyl-Dye in poly(vinyl toluene) films (Figure 6.9(b)). The total bathochromic shift in the Meta-Octyl-Dye in poly(vinyl toluene) emission is 20 nm with increased loadings from 1–15 wt.%, while a larger 32 nm shift is observed over the smaller loading range of 1–9 wt.% tested for Para-Octyl-Dye in poly(vinyl toluene) films, which is again indicative of the greater degree of solvatochromic effects that are observed for the *para*-substituted isomers of these dyes. Overall, the magnitude of these solvatochromic shifts is much lower than is observed over the range of solvents shown in Figures 6.4(b) and 6.5(b), which indicates that while increased dye loading does increase the average polarity of the resulting solid, the overall shift is still lower when compared to solutions in mildly polar solvents such as chloroform. Another striking feature of both Figures 6.8(b) and 6.9(b) is that the emission from either dye at the lowest loadings in poly(vinyl toluene) is of shorter wavelength than the same dye dissolved in toluene at room temperature, despite the analogous nature of dipolar and electronic properties of these two different media. In fact, the peak emissions from 1 wt.% samples of Meta-Octyl-Dye in poly(vinyl toluene) (404 nm) and Para-Octyl-Dye in poly(vinyl toluene) (419 nm) are both quite close to the maxima (403 and 409 nm, respectively) of their corresponding low temperature solutions in toluene that are shown in Figures 6.6(b) and 6.7(b). This indicates that the rigid environment of the solid films reduce the ability for vibrational relaxation of the S_1 excited states, leading to shorter wavelength emission in a fashion very similar to the low temperature, frozen solution spectra.

The shift in the emission spectra towards longer wavelengths with increasing dye content has several practical implications to take into account when considering use of these or similar TADF-based dyes for scintillation applications. Since their absorbance spectra are relatively unchanged with increased dye loading, this effectively increases the Stokes shift of the plastic with increased loading, which has the net effect of reducing self absorption and improving photon outcoupling, all other factors being equal. From Figure 6.8 the Stokes shift of Meta-Octyl-Dye in poly(vinyl toluene) films was determined to range from 54–75

nm (depending on primary dye content), while for the Para-Octyl-Dye in poly(vinyl toluene) spectra of Figure 6.9, the Stokes shifts ranged from 69–101 nm. However, increased emission wavelengths away from the optimal region for absorption by a photomultiplier tube photocathode will have a detrimental effect on the suitability for use with photomultiplier tube readout. As such the net combination of both these effects will need to be taken into account when determining the overall suitability of these types of plastics for use in real world detectors.

6.5   TADF Scintillator Sample Fabrication

To determine the actual suitability and performance of the TADF dyes for scintillation applications, monolithic plastic scintillator samples were prepared, using the commonly employed poly(vinyl toluene) as the aromatic matrix polymer. However, since the *tert*-butyl-substituted variants of the TADF dyes (Meta-*t*Butyl-Dye and Para-*t*Butyl-Dye) were found to be too insoluble in the poly(vinyl toluene) monomer (methylstyrene, a.k.a. vinyltoluene), scintillator samples were prepared via bulk polymerization using only the enhanced solubility octyl-substituted variants as primary dyes, namely either Meta-Octyl-Dye or Para-Octyl-Dye. In conjunction to these unshifted samples containing only primary dye, additional samples were prepared utilizing a secondary wavelength shifting dye, in this case 1,4-bis-[4-(di-*p*-tolylamino)styryl]benzene (DPAVB), which is a blue/green dye commonly used in organic dye/thin-film laser and organic light emitting diode applications.[63–65] As a solution in toluene, DPAVB was measured to have Φ_{PL} = 0.813, which while not quite as high as traditional deep blue wavelength shifters commonly employed in plastic scintillators, such as 1,4-bis(5-phenyl-2-oxazolyl)benzene (POPOP, Φ_{PL} = 0.93 in cyclohexane[55]) or 9,10-Diphenylanthracene (DPA, Φ_{PL} = 1.00 in cyclohexane[55]), is still high enough to be useful as a wavelength shifter for the TADF dyes. The structure and absorption/photoluminescence spectra of DPAVB are shown in Figure 6.10, along with a comparison with the photoluminescence spectra of Meta-Octyl-Dye and Para-Octyl-Dye. The emission from DPAVB is primarily in the range of 450–525 nm, with a peak emission at 464 nm, resulting in sky-blue
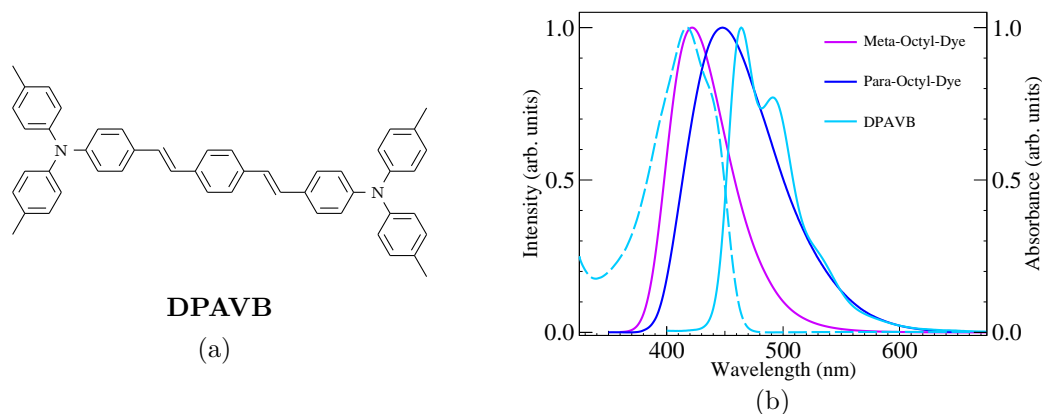
Figure 6.10: (a) Structure of 1,4-bis[4-(di-*p*-tolylamino)styryl]benzene (DPAVB) and (b) comparison of the absorption (dashed) and emission (solid) spectra of DPAVB with the emission spectra of Meta-Octyl-Dye and Para-Octyl-Dye in toluene.

emission color, and this emission range was deliberately chosen so that the final scintillation emission would still be reasonably within the photosensitive wavelength region of a typical bialkali photomultiplier tube photocathode. The DPAVB absorption peak at 418 nm is very close to the peak emission of Meta-Octyl-Dye in toluene (422 nm), which leads to very good spectral overlap between the two dyes. Para-Octyl-Dye, on the other hand, has a longer wavelength peak emission in toluene of 448 nm, and while there does exist a good degree of overlap with the absorbance of DPAVB, lower efficiency of the primary to secondary radiative energy transfer process is to be expected for the Para-Octyl-Dye/DPAVB dye combination. Finally, with DPAVB's Stokes shift of 46 nm, which is not high enough to achieve total separation of the absorbance and emission spectra, actual samples wavelength shifted with DPAVB are expected to have peak emission of their technical emission spectra further shifted into the green portion of the spectrum than would be suggested by the solution spectra shown in Figure 6.10(b) alone.

During sample preparation, both Meta-Octyl-Dye and Para-Octyl-Dye were found to be highly soluble (even at room temperature) in the methylstyrene monomer, at least for all of the primary dye concentrations tested. However, after initial heating and solution gelation, noticeable loss of transparency was observed for samples at the higher end of the

loading scales tested for each respective dye. Examination of the highest loaded samples via optical microscopy did not lead to observation of distinct phase microstructure or discern the presence of dye precipitates, although additional higher resolution microscopy was not performed. In any case, the slow loss of transparency observed towards the end of the sample curing would indicate that the dyes have significantly lower solubility in the poly(vinyl toluene) polymer as compared to the liquid monomer. A possible reason for this diminished solubility would be the polar sulfone groups, since these would have less favorable interactions with the non-polar poly(vinyl toluene) chains as compared to a completely non-polar dye. If one assumes that no crystallization of the dye occurred during the curing, towards the end of polymerization, the depletion of the remaining monomer needed to continue solvation of the polar dye would lead way to gradual exclusion of dye molecules to create separate dye-enriched and dye-depleted domains, the optical scattering from which would account for the loss of transparency of the bulk samples. If distinct precipitation and/or crystallization is instead occurring, a similar loss of transparency would also result, and it is conceivable that precipitate domains could remain on a scale small enough to be indistinguishable via optical microscopy. Because reduced transparency leading to poor photon outcoupling will lead to an overall loss of performance of a scintillator, the lowest primary dye loading that produced total loss of transparency was the upper limit of the dye concentration ranges that were examined.

Of the two octyl-substituted isomers, Meta-Octyl-Dye was found to be significantly more soluble in poly(vinyl toluene) that Meta-Octyl-Dye, with a loading of 15 wt.% of Meta-Octyl-Dye being the highest tested concentration before total loss of transparency. Figure 6.11 shows representative photographs of the appearance and emission color of Meta-Octyl-Dye in poly(vinyl toluene) scintillator samples over the range of 1–15 wt.% of primary dye, Figure 6.12 shows the transmission and photoluminescence spectra of the Meta-Octyl-Dye in poly(vinyl toluene) samples tested. At the low end of the Meta-Octyl-Dye loading range, the bulk plastic samples appeared visually to be totally colorless, with a violet to blue emission. At the highest Meta-Octyl-Dye loadings, a slight yellow color of the plastic was discernible, which can be faintly seen in Figure 6.11(a), which is attributable to the very slight extension

(a) Visible Illumination

(b) UV Illumination

Figure 6.11: Photographs of unshifted 1–15 wt.% Meta-Octyl-Dye in poly(vinyl toluene) scintillator samples.

(a)

(b)
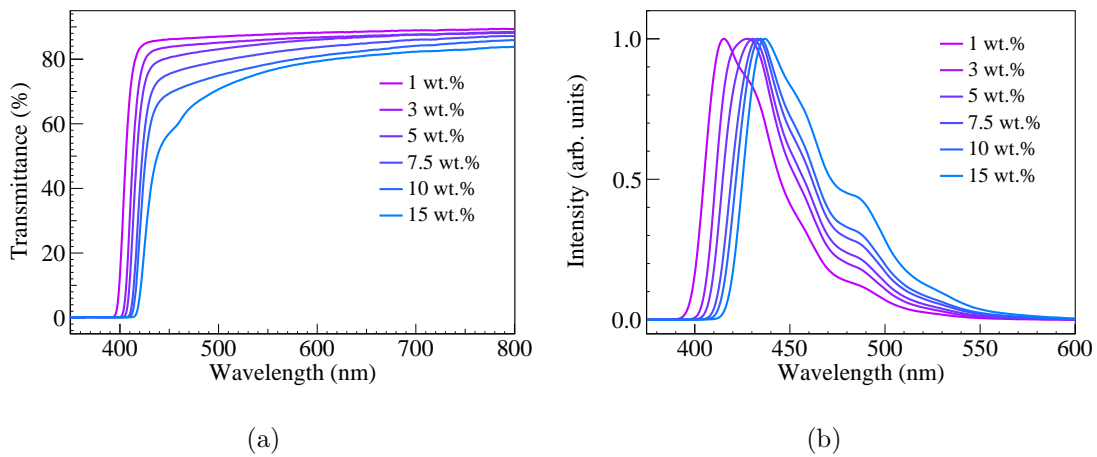
Figure 6.12: (a) UV/Vis transmission and (b) transmission-mode photoluminescence spectra of 3.5 mm thick samples of 1–15 wt.% Meta-Octyl-Dye in poly(vinyl toluene).

of the absorbance spectra of Meta-Octyl-Dye into the visible part of the spectrum ($>$400 nm) which can be seen in Figure 6.8(a). In Figure 6.12(b), the photoluminescence spectra are acquired in true transmission-mode, where the incident beam is largely absorbed on one of the circular faces of the cylinder, and the luminescence is sampled from the opposite circular face. In this fashion, all of the effects of self absorbance by the sample itself are preserved, and thus a transmission-mode photoluminescence spectrum represents the best approximation to the true *technical* emission spectrum that would be observed by a photomultiplier tube during actual scintillation testing.[2] These effects are clearly demonstrated in Figure 6.12(b) by the bathochromic shift of peak emission wavelength with increasing primary dye content,

going from 415 nm at a loading of 1 wt.% to 434 nm at 15 wt.%, a total shift of 19 nm over the whole concentration range. Furthermore, the absorption and re-emission processes create a biasing effect towards emission from longer wavelengths, which can clearly be seen in the fact that emission from the $0 \rightarrow n$ vibrational sub-bands contribute to a greater fraction of the total emission as the primary dye content is increased. As was mentioned in Section 6.4, the increasing shift in overall emission towards longer wavelengths will in the end have a net detrimental effect on the scintillation performance when used in conjunction with conventional bialkali photomultiplier tube photocathodes, since a greater proportion of the total emission is falling outside of the photomultiplier tube's' quantum efficiency range.

The transmission spectra in Figure 6.12(a) provide a quantitative measure of the loss of overall transparency with increasing Meta-Octyl-Dye content. At the lowest lading (1 wt.%), the transmission is relatively flat throughout the visual range, but as the loading content is increased up to the maximum tested (15 wt.%), loss of transmission is most severe in the 400–500 nm range, but there is still significant loss over the rest of the spectrum above 500 nm. While losses in the range below 450 nm can be largely attributable to absorptive loss, especially due to the tailing of the absorption spectrum of Meta-Octyl-Dye into the visible range, at longer wavelengths, the absorption of the primary dye alone cannot fully account for the transmissive losses. Instead, losses in this wavelength range are directly attributable to scattering due to the phase segregation as was previously discussed. Furthermore, the loss of transparency is decreasing with increased wavelength within this range, which is consistent with a Rayleigh scattering mechanism, and thus if this mechanistic assignment is correct, it would imply that the phase segregated domains are of nanometer scale in size. Rayleigh scattering by nanoscale phase domains is known to be an issue in terms of transmissive loss for plastic scintillators where a truly homogeneous nanostructure does not exist.[66–68]

Interestingly, as part of attempts to further increase the attainable primary dye loadings, it was found that addition of the crosslinking monomer divinylbenzene (DVB) at a level of 5 wt.%, to give a crosslinked poly(vinyl toluene) matrix polymer (XLPVT) was able to not only significantly improve the overall transparency of the resulting plastic, but higher loadings of Meta-Octyl-Dye were found to be possible than for the uncrosslinked

(a) Visible Illumination

(b) UV Illumination
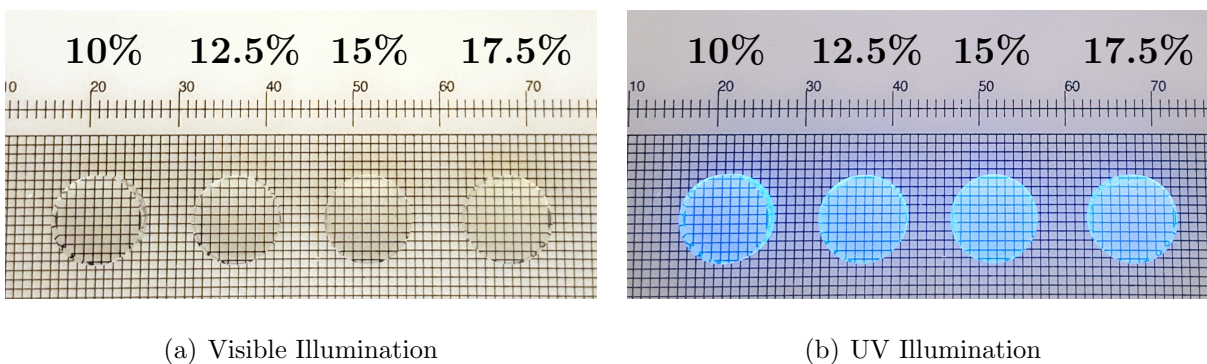
Figure 6.13: Photographs of unshifted 10–17.5 wt.% Meta-Octyl-Dye in crosslinked poly(vinyl toluene) scintillator samples.

(a)

(b)

Figure 6.14: (a) UV/Vis transmission and (b) transmission-mode photoluminescence spectra of 3.5 mm thick samples of 1–17.5 wt.% Meta-Octyl-Dye in crosslinked poly(vinyl toluene).

polymer. Figure 6.13 shows representative photographs of the appearance of Meta-Octyl-Dye in crosslinked poly(vinyl toluene) samples with Meta-Octyl-Dye loadings as high as 17.5 wt.%, which retain high clarity even at the increased loading ranges, while Figure 6.14 shows the transmission and photoluminescence spectra measured for the full loading range of Meta-Octyl-Dye in crosslinked poly(vinyl toluene) scintillator samples. It should be noted that although 17.5 wt.% was the highest Meta-Octyl-Dye loading tested for the crosslinked poly(vinyl toluene) matrix, it is fully expected that higher loadings are possible, due to the high solubility of the primary dye in the monomer solution and the lack of significant loss in transparency at the ranges tested. Additional Meta-Octyl-Dye in crosslinked poly(vinyl

toluene) samples with loadings higher than 17.5 wt.% were not prepared due to reasons to be addressed in Sections 6.6 and 6.8. From the transmission spectra in Figure 6.14(a), it can clearly bee seen that there is a substantial improvement in the transmission at wavelengths above 450 m for the Meta-Octyl-Dye in crosslinked poly(vinyl toluene) system, as compared to its uncrosslinked counterpart. Some coloration is still evident in the samples with the highest dye loadings, which is also evident in th transmission spectra for wavelengths below 450 nm, but this is again attributable to the residual absorption of the primary dye within the visible range. Unlike the transmission spectra, the photoluminescence spectra in Figure 6.14(b) for the Meta-Octyl-Dye in crosslinked poly(vinyl toluene) samples are very similar in appearance to the uncrosslinked spectra in Figure 6.12(b), which is unsurprising since the nonpolar aromatic crosslinker divinylbenzene is chemically similar to the methylstyrene monomer, and the resulting crosslinked matrix should be quite similar in its solvatochromic impact compared to that of uncrosslinked poly(vinyl toluene).

Figure 6.15 shows representative photographs of the appearance of Meta-Octyl-Dye in (uncrosslinked) poly(vinyl toluene), with an additional 0.05 wt.% of DPAVB as a secondary, wavelength shifting dye, while Figure 6.16 depicts transmission and photoluminescence spectra of the entire primary dye loading range of the wavelength shifted Meta-Octyl-Dye in poly(vinyl toluene) samples. Samples of wavelength shifted Meta-Octyl-Dye in poly(vinyl toluene) over the primary dye loading range from 1–10 wt.% were prepared, the upper limit of which was chosen for reasons to be elaborated further in Sections 6.6 and 6.8. All of the DPAVB shifted samples shown in Figure 6.15 are yellow in color, since DPAVB is strongly absorbing in the range below 475 nm, as shown in Figure 6.15(b). When visually observed, the effects of self-absorption in DPAVB shifted samples lead to a change in the apparent emission color from cyan under front side illuminaton (like the photographs in Figure 6.16(b)) to nearly fully green when viewed under transmission-mode conditions. The later of these conditions is best recognized in the photoluminescence spectra of Figure 6.16(b), with the peak emission for all samples being nearly 500 nm in wavelength, significantly higher than the peak emission of DPAVB (464 nm) in solution (Figure 6.10(b)). Since the content of DPAVB remains constant, the transmission and photoluminescence spectra in Figure 6.16

(a) Visible Illumination (b) UV Illumination
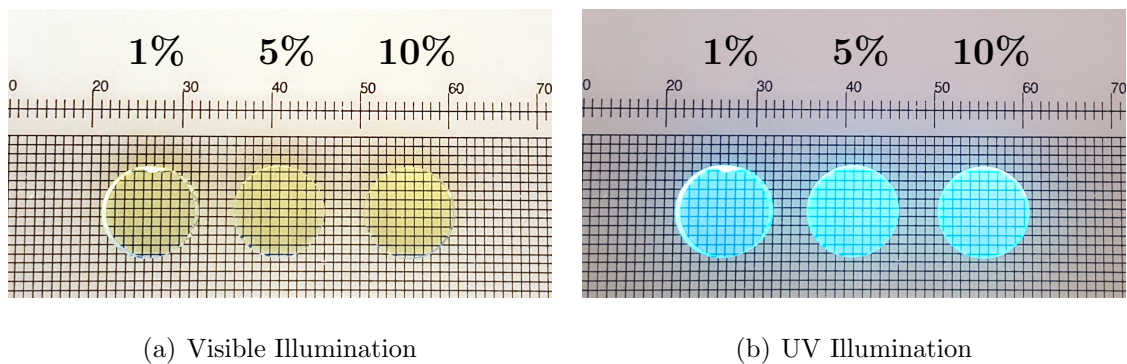
Figure 6.15: Photographs of 1–10 wt.% wavelength shifted Meta-Octyl-Dye in poly(vinyl toluene) scintillator samples.

(a) (b)
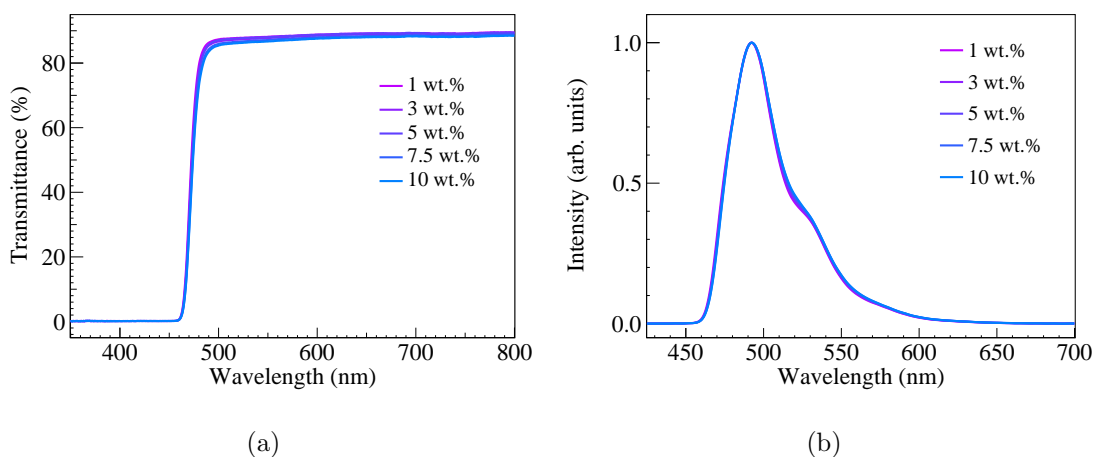
Figure 6.16: (a) UV/Vis transmission and (b) transmission-mode photoluminescence spectra of 3.5 mm thick samples of 1–10 wt.% wavelength shifted Meta-Octyl-Dye in poly(vinyl toluene).

remain essentially unchanged despite the varied primary dye loading, which is unsurprising given that it is the wavelength shifter that determines these characteristics in the final material.

On account of the overall lower solubility of Para-Octyl-Dye in poly(vinyl toluene), scintillator samples of Para-Octyl-Dye in poly(vinyl toluene) were prepared only in the primary dye loading range of 1–10 wt.%, and Figure 6.17 shows representative photographs of the appearance of Para-Octyl-Dye in poly(vinyl toluene) scintillator samples spanning this range, while Figure 6.18 displays the transmission and photoluminescence spectra for the full range of

(a) Visible Illumination   (b) UV Illumination
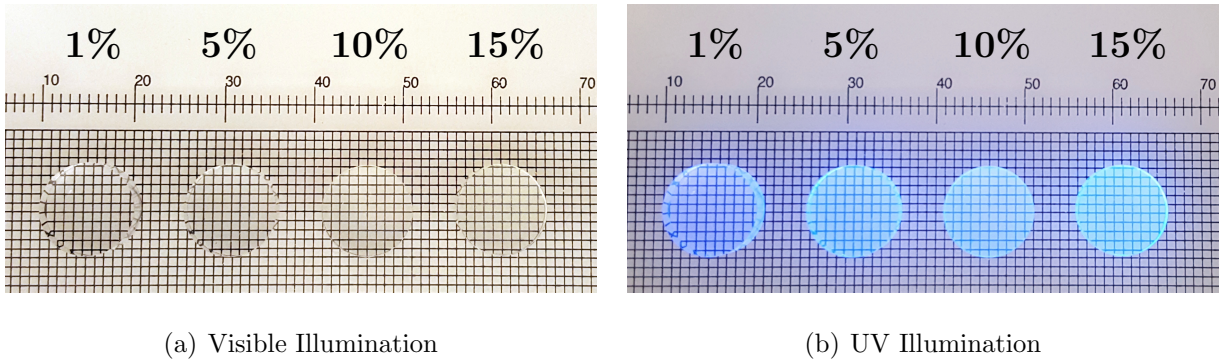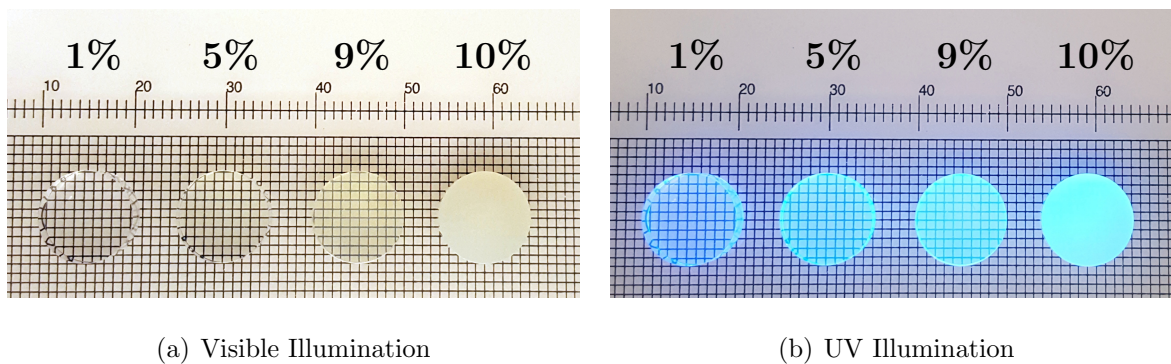
Figure 6.17: Photographs of unshifted 1–10 wt.% Para-Octyl-Dye in poly(vinyl toluene) scintillator samples.

(a)   (b)
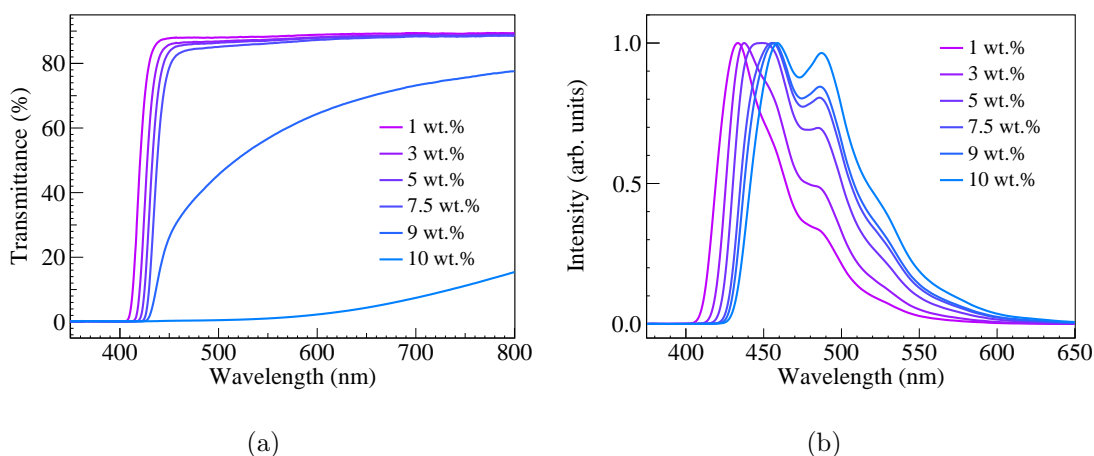
Figure 6.18: (a) UV/Vis transmission and (b) transmission-mode photoluminescence spectra of 3.5 mm thick samples of unshifted 1–10 wt.% Para-Octyl-Dye in poly(vinyl toluene).

Para-Octyl-Dye in poly(vinyl toluene) samples prepared. At the highest loading tested (10 wt.%), phase segregation and/or precipitation led to total loss of transparency, and the next lowest loading (9 wt.%) retained some transparency but has a noticeably hazy appearance. The appearance of yellow coloration in the Para-Octyl-Dye in poly(vinyl toluene) samples was apparent at considerably lower primary dye loadings as compared to Meta-Octyl-Dye in poly(vinyl toluene), which is due to the fact that not only do the absorbance spectra of Para-Octyl-Dye shown in Figure 6.9(a) display a greater degree of tailing into the visible range, but also the additional bathochromic shift of the absorption edge with increased Para-Octyl-Dye loadings, as was discussed in Section 6.4. From Figure 6.18(a), it is notable that the

loss of transparency is occurring over a considerably smaller primary dye loading range, with nearly all loss of transparency occurring within the range of 7.5–10 wt.%. For the 9 wt.% sample, the greater transmission loss at shorter wavelengths would still suggest a Rayleigh scattering mechanism, but at 10 wt.%, the totally opaque character of the sample in conjunction with the transmission data would suggest that the phase domains may have grown sufficiently large to render the Rayleigh scattering an inappropriate description of the optical transport properties of the material. The photoluminescence spectra in Figure 6.18(b) also display a bathochromic shift in peak wavelength, going from 433 nm at 1 wt.% loading to 460 nm at 10 wt.%, a considerably larger shift (27 nm) over a narrower concentration range as compared to Meta-Octyl-Dye in poly(vinyl toluene) samples. The more dramtic shift in Para-Octyl-Dye emission with primary dye loading observed in these samples is quite similar to the emission shifts discussed in Section 6.4 for the Para-Octyl-Dye in poly(vinyl toluene) thin film samples, as compared to the Meta-Octyl-Dye in poly(vinyl toluene) thin films (Figures 6.8(b) and 6.9(b)). As such, it can be seen that it is not only increased self-absorption due to increased primary dye content, but also the shift in the molecular emission spectra of the primary dye that are both major factors in determination of the overall appearance of the technical photoluminescence spectra for both of the (unshifted) Meta-Octyl-Dye in poly(vinyl toluene) and Para-Octyl-Dye in poly(vinyl toluene) systems.

Para-Octyl-Dye based samples were also prepared in poly(vinyl toluene) using DPAVB as a wavelength shifter, with the same 0.05 wt.% secondary dye loading as used for the wavelength shifted Meta-Octyl-Dye in poly(vinyl toluene) samples. Figure 6.19 shows representative photographs of the appearance of the wavelength shifted Para-Octyl-Dye in poly(vinyl toluene) samples, while Figure 6.20 displays the transmission and photoluminescence spectra obtained over the entire primary dye loading range of prepared samples. For this series, the upper limit of dye loading was kept at 9 wt.%, since the (unshifted) Para-Octyl-Dye in poly(vinyl toluene) samples demonstrated this to be the upper primary dye loading that would still yield some remaining transparency. In general, both the transmission and photoluminescence spectra are nearly identical in appearance to the spectra in Figure 6.16, which again is unsurprising since DPAVB is governing the spectral properties of the wave-

(a) Visible Illumination (b) UV Illumination
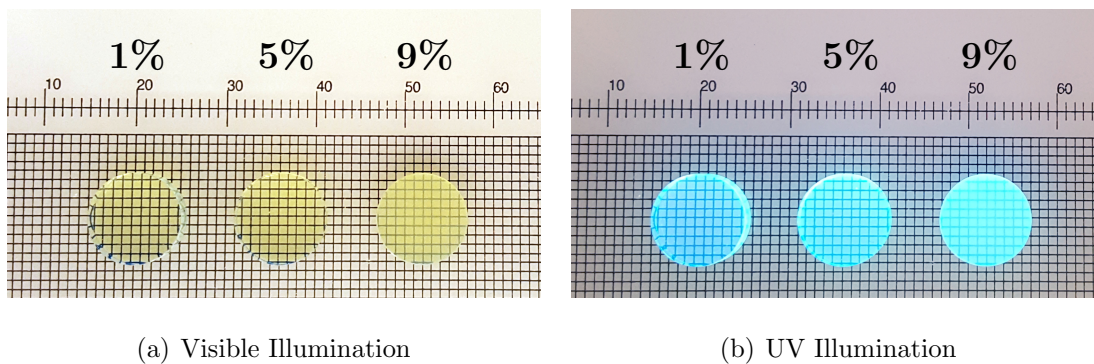
Figure 6.19: Photographs of 1–9 wt.% wavelength shifted Para-Octyl-Dye in poly(vinyl toluene) scintillator samples.

(a)   (b)
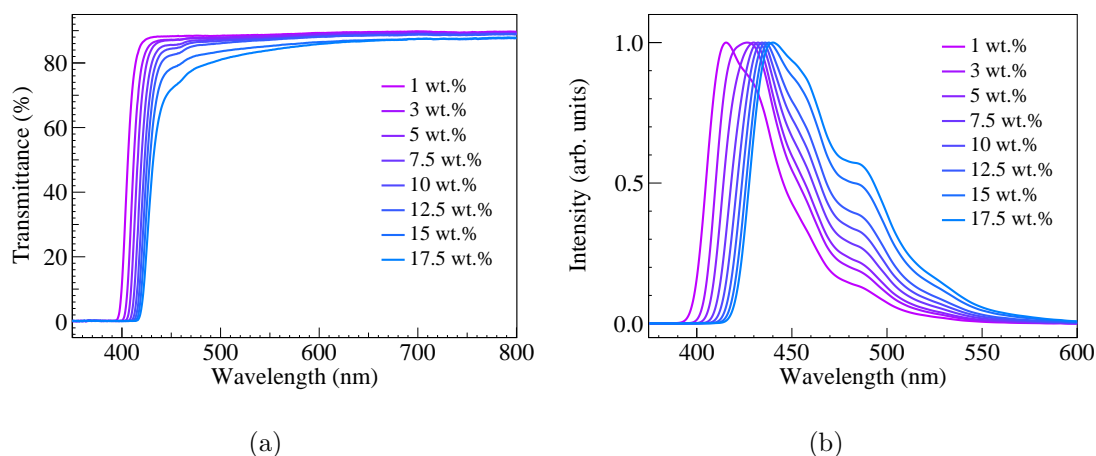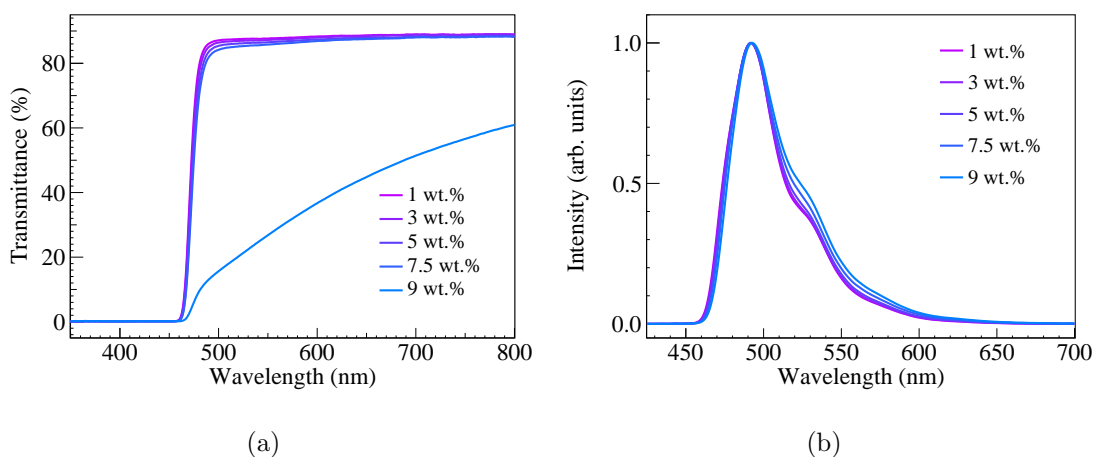
Figure 6.20: (a) UV/Vis transmission and (b) transmission-mode photoluminescence spectra of 3.5 mm thick samples of 1–9 wt.% wavelength shifted Para-Octyl-Dye in poly(vinyl toluene).

length shifted materials. The only major difference is the transmission spectrum for the 9 wt.% wavelength shifted Para-Octyl-Dye in poly(vinyl toluene) sample in Figure 6.20(a), for which the overall transparency is considerably lower to to the greater degree of scattering for this content of Para-Octyl-Dye as compared to the primary dye loading range shown in Figure 6.16.
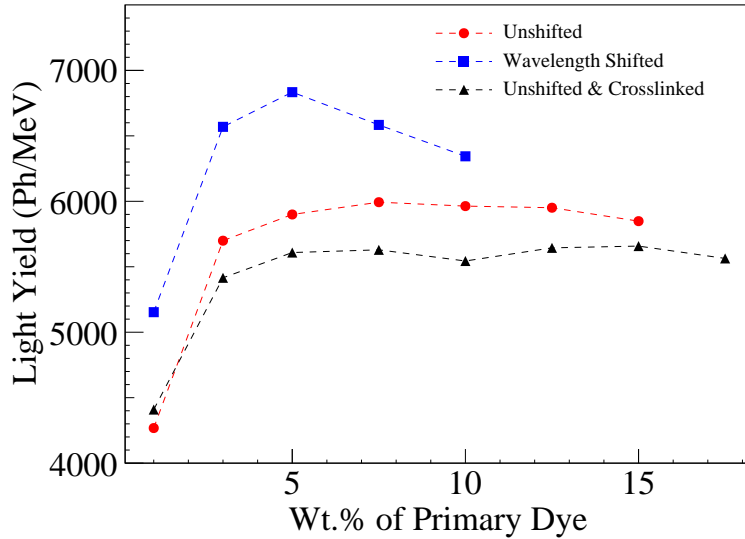
Figure 6.21: Scintillation light yields measured with ^{137}Cs γ-rays for Meta-Octyl-Dye in poly(vinyl toluene), Meta-Octyl-Dye in crosslinked poly(vinyl toluene), and wavelength shifted Meta-Octyl-Dye in poly(vinyl toluene) scintillator samples as a function of primary dye loading.

6.6   TADF Scintillator Light Yields

Figure 6.21 plots the combined ^{137}Cs light yields as a function of primary dye content for the Meta-Octyl-Dye in poly(vinyl toluene), Meta-Octyl-Dye in crosslinked poly(vinyl toluene), and wavelength shifted Meta-Octyl-Dye in poly(vinyl toluene) scintillator samples, which have been corrected to account both for the technical emission spectrum of the particular sample under examination, and the quantum efficiency data for the photomultiplier tube used during testing (Hamamatsu R878). For the Meta-Octyl-Dye in poly(vinyl toluene) samples, the light yield quickly rises from $\sim$4250 photons/MeV at a primary dye loading of 1 wt.% up to a maximum of $\sim$6000 photons/MeV at a loading of 7.5 wt.%, and only very slightly drops off to $\sim$5850 photons/MeV at 15 wt.%, the highest primary dye loading tested for this system. In a similar fashion, the light yields for the Meta-Octyl-Dye in crosslinked poly(vinyl toluene) samples rises from $\sim$4400 photons/MeV at a primary dye loading of 1 wt.% up to a maximum of $\sim$5625 photons/MeV at 7.5 wt.%, and remains roughly at this level before

finally being reduced to ∼5550 photons/MeV at the highest loading of 17.5 wt.%. The peak light yield at 7.5 wt.% of primary dye is a somewhat high loading content for a composition displaying maximal light yield, although this is likely due to the fact that the molecular weight of the Meta-Octyl-Dye is quite high, which lowers the actual concentration relative to traditional scintillating dyes which are lower in molecular weight. Given the degree of self absorption, it is not unreasonable to expect that addition of a suitable wavelength shifting dye to the formulation would result in marked improvement to the total light yield. While the overall shape of the light yield curves between the crosslinked and uncrosslinked samples is very similar, it is important to note that the crosslinked samples displayed consistently lower light yields as compared to the uncrosslinked samples for all loadings except the very lowest. This observation seems counterintuitive if one only considers the expectation that the crosslinked samples, with their lower scattering and increased transparency, should allow for greater efficiency in photon outcoupling and thus improved light over their uncrosslinked counterparts. However, it has been demonstrated that the presence of residual monomer in plastic scintillators can have a deleterious influence on the scintillation performance, since the residual monomer can act as a trap for excitons present on the aromatic polymer matrix, and thus potentially interfere with the overall scintillation processes.[69–71] Since the divinylbenzene crosslinker is a difunctional reagent, and since the increase in viscosity during bulk-polymerization of crosslinked polymers is very rapid, limiting further diffusion of unreacted monomers, it is reasonable to expect that a markedly higher fraction of unreacted vinyl groups would remain in the crosslinked samples, especially since the curing conditions (80 ℃ for 24 hours) were kept unchanged for all samples prepared throughout this investigation. What is additionally interesting about the data for the Meta-Octyl-Dye in poly(vinyl toluene) and Meta-Octyl-Dye in crosslinked poly(vinyl toluene) samples in Figure 6.21 is that there is not any strong decrease in the light yield for primary dye loadings greater than the maximal values observed for loadings of 7.5 wt.%. This observation serves to indicate two primary factors controlling the light yield in this upper concentration range, the first of which is that the lack of any observed strong decrease in light yield with further loading increase suggests that little if any concentration quenching of the primary dye is present

over the tested loading range. The second major factor controlling the light yield in this range is the effects of self absorption that are manifested due to the increased primary dye loading. In the absence of any other factors, an increase in primary dye loading beyond the level of peak scintillation efficiency will typically lead to a decrease in light yield due to an increased degree of self absorption by the primary dye. In the particular case of Meta-Octyl-Dye, there is an additional factor of the bathochromic shift in peak emission that is illustrated in the molecular photoluminescence spectra of Figure 6.8(b), which effectively leads to an increase in the Stokes shift of the primary dye with increasing concentration, thus reducing the overlap of the absorbance and photoluminescence spectra. As such, these two factors that govern the total magnitude of self-absorption in the samples are acting counter to one another, which explains the relatively unchanged light yield throughout the region of primary dye loading above 7.5 wt.% for the Meta-Octyl-Dye in poly(vinyl toluene) and Meta-Octyl-Dye in crosslinked poly(vinyl toluene) samples.

Interestingly, the light yields for the wavelength shifted Meta-Octyl-Dye in poly(vinyl toluene) samples that are also displayed in Figure 6.21 display somewhat different behavior as compared to their unshifted counterparts. Similarly, the light yields for the wavelength shifted Meta-Octyl-Dye in poly(vinyl toluene) samples quickly rise from a minimum of $\sim$5150 photons/MeV at the lowest primary dye loading of 1 wt.% up to a maximum of $\sim$6825 photons/MeV at a loading of 5 wt.%, which is at a lower primary dye content than the corresponding Meta-Octyl-Dye in poly(vinyl toluene) and Meta-Octyl-Dye in crosslinked poly(vinyl toluene) samples with peak light yields. Another significant difference is the behavior for primary dye loadings above 5 wt.%, which display a significantly steeper drop-off in light yield, down to $\sim$6350 photons/MeV at the maximum loading tested, 10 wt.%. Given that the secondary dye content was held fixed for all of the wavelength shifted samples shown in Figure 6.21, and that the light yields for the wavelength shifted samples above 5 wt.% depend more strongly on the primary dye loading than does the light yield of samples of only primary dye and polymer matrix, it is presumable that some joint interaction between the primary and secondary dyes is responsible for this anomalous behavior. No significant change could be observed in the transmission and photoluminescence spectra of Figure 6.16

80

for samples of wavelength shifted Meta-Octyl-Dye in poly(vinyl toluene) that varied with primary dye content, and thus no direct evidence was observed to suggest that any chemical degradation or reaction of the DPAVB took place as a result of increased Meta-Octyl-Dye content. As such, another plausible explanation for the decreased light yield would be due to exiplex formation between DPAVB and the primary dye, leading to quenching of the DPAVB excited states and loss of photoluminescence quantum yield for the secondary dye. At present, the role of exiplex formation is merely a conjecture, and would require additional spectroscopic and photophysical investigations to establish in full. However, since the rate of exiplex formation is expected to be first order with respect to the primary dye concentration, DPAVB quenching via such a mechanism would account for the observed decrease in light yield at primary dye concentrations above 5 wt.%, which is effectively a threshold primary dye concentration to allow for an observable rate of exiplex formation and secondary dye quenching. Below this threshold, the normal factors of efficiency in non-radiative energy transfer between matrix and primary dye would still be the predominate factor determining the overall observed light yield for the wavelength shifted samples. In any case, however, the overall light yields for wavelength shifted Meta-Octyl-Dye in poly(vinyl toluene) samples were found to be significantly improved over the corresponding unshifted Meta-Octyl-Dye in poly(vinyl toluene) samples, which indicates that DPAVB is indeed an effective wavelength shifter for the Meta-Octyl-Dye primary dye, at least over these primary dye loading ranges.

Figure 6.22 plots the combined ^{137}Cs light yields as a function of primary dye content for both the Para-Octyl-Dye in poly(vinyl toluene) and wavelength shifted Para-Octyl-Dye in poly(vinyl toluene) scintillator samples, which again are corrected to account for the photomultiplier tube's spectral sensitivity. When compared to the light yield data for samples of Meta-Octyl-Dye (Figure 6.21), the data obtained for the Para-Octyl-Dye in poly(vinyl toluene) samples show some intriguing differences. As compared to Meta-Octyl-Dye in poly(vinyl toluene), the light yields for Para-Octyl-Dye in poly(vinyl toluene) start out as a higher relative fraction of the peak light yield (on the basis of primary dye loading), and the Para-Octyl-Dye in poly(vinyl toluene) system reaches a peak light yield at lower primary dye loading (5 wt.%) than for the Meta-Octyl-Dye in poly(vinyl toluene) system (7.5 wt.%).
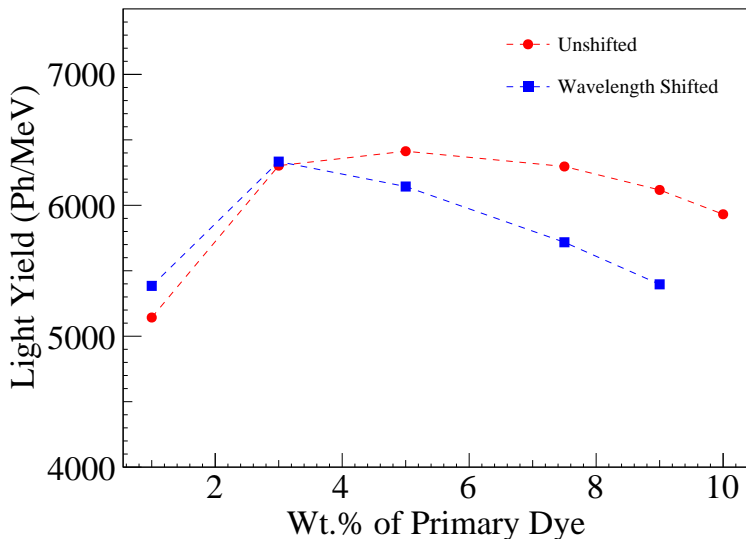
Figure 6.22: Scintillation light yields measured using a ^{137}Cs γ-rays for unshifted and DPAVB shifted Para-Octyl-Dye in poly(vinyl toluene) scintillator samples as a function of primary dye loading.

Above the peak at 5 wt.%, the light yields for Para-Octyl-Dye in poly(vinyl toluene) start to fall off at a faster rate than observed for Meta-Octyl-Dye in poly(vinyl toluene), but this is simply attributable to the rapid loss of transparency for Para-Octyl-Dye loadings above 7.5 wt.%. By far the most notable of these differences is that within the primary dye loading range of 1–9 wt.%, all of the Para-Octyl-Dye in poly(vinyl toluene) samples demonstrated markedly higher light yields, generally ∼105–120% of the light yield their Meta-Octyl-Dye in poly(vinyl toluene) counterparts. At higher loading, the severe loss of transparency in the 10 wt.% Para-Octyl-Dye in poly(vinyl toluene) sample resulted in a decreased light yield approximately equal to its Para-Octyl-Dye in poly(vinyl toluene) counterpart, but direct comparison of these samples is not proper due to their large differences in transparency. What is particularly striking about the higher light yields for the Para-Octyl-Dye samples is that if one takes into account the photoluminescence quantum yields (Table 6.3) of the primary dyes, all things being equal, one would expect the Meta-Octyl-Dye based samples to outperform those based on Para-Octyl-Dye, since the former dye has ∼17% higher photoluminescence quantum yield. This increase in light yield despite a lower photoluminescence

82

quantum yield is a manifestation of the the lower singlet-triplet splitting of Para-Octyl-Dye as compared to Meta-Octyl-Dye, which through the reverse intersystem crossing process is enabling a greater degree of conversion of T_1 to S_1 excited states, thus improving the total light output from the Para-Octyl-Dye in poly(vinyl toluene) scintillators. As will be further addressed in Sections 6.7 and 6.8, this is but one of several instances where the reduced singlet-triplet splitting of Para-Octyl-Dye has demonstrable effects on the scintillation characteristics of samples employing it as a primary dye.

Another striking difference between the Para-Octyl-Dye and Meta-Octyl-Dye samples in the data presented in Figure 6.22 is the lack of any meaningful improvement in the performance of the wavelength shifted Para-Octyl-Dye in poly(vinyl toluene) samples. At primary dye loadings of 3 wt.% and lower, there is a slight improvement in the light yield with the addition of DPAVB, but above 3 wt.% (the peak in light yield with primary dye loading), the wavelength shifted Para-Octyl-Dye in poly(vinyl toluene) samples demonstrated consistently lower yields, and fall off from their peak value at a noticeably faster rate than the unshifted Para-Octyl-Dye in poly(vinyl toluene) samples. This sharp decrease in light yield is actually consistent with the data for wavelength shifted Meta-Octyl-Dye in poly(vinyl toluene) samples presented in Figure 6.21, which again may be due to the effects of quenching via exciplex formation. On the other hand, the lack of overall improvement in the light yield for all but the lowest loaded samples of wavelength shifted Para-Octyl-Dye in poly(vinyl toluene) is attributable to the poorer spectral overlap between Para-Octyl-Dye and DPAVB, as was shown in Figure 6.10(b). With an overall lower efficiency for the radiative energy transfer between primary and secondary dyes, the deleterious effects of the quenching of the secondary dye outweigh any additional gains that would have been obtained through reduction of the effects of self absorption. Moreover, the fact that samples of Para-Octyl-Dye in poly(vinyl toluene) consistently displayed larger Stokes shifts (Figure 6.8) as compared to those of Para-Octyl-Dye (Figure 6.9) further indicate that Para-Octyl-Dye is overall less impacted by self-absorption than Meta-Octyl-Dye, further limiting any gains in light yield that would be attainable via wavelength shifting in the absence of other loss mechanisms. Accordingly, it is likely that with a better choice of wavelength shifting secondary dye,

further improvements in the light yield of Para-Octyl-Dye would be achievable, but the overall performance of any scintillators based on Para-Octyl-Dye as a primary dye will be limited by its lower photoluminescence quantum yield.

6.7 TADF Scintillator Decay Characteristics

A key factor in assessing the degree to which TADF processes are operative in the Meta-Octyl-Dye and Para-Octyl-Dye based scintillator samples is the observed behavior of the decay of the scintillation pulses. In traditional organic scintillators, the slow decay component arises through the annihilation of T_1 states to produce additional and delayed S_1 states according to Equation (3.2). The rate of the annihilation process is considerably slower than the radiative emission from S_1 states, and as such the kinetics of the delayed emission for conventional organic scintillators is completely determined by the rate of formation of delated S_1 states. Since triplet-triplet annihilation is a bimolecular process with respect to the total T_1 concentration, the delayed emission observed for conventional scintillators is characteristically non-exponential in its decay behavior. The TADF phenomenon, on the other hand, is largely governed by the combination of the intersystem crossing and reverse intersystem crossing process described in Section 6.2, the latter of which is directly responsible for the delayed fluorescence via conversion of T_1 to S_1 states according to Equation (6.1b). As such, reverse intersystem crossing is an inherently unimolecular process, and accordingly delayed emission via a TADF mechanism should display completely exponential decay behavior. However, there is nothing about the TADF mechanism that fundamentally prevents additional delayed emission via triplet-triplet annihilation assuming sufficient densities of T_1 states are present. and for scintillation processes in particular, the high density of excited states along the incident particle track necessitates that both mechanisms of delayed fluorescence production be considered when analyzing the decay behavior of a particular TADF capable scintillator.

In the time frame shortly after the incident particle has deposited its energy along its track, i.e., immediately after internal conversion of higher excited states to effectively es-

tablish initial populations of S_1 and T_1 states along the particle track, the rate equations governing the overall population of S_1 and T_1 states can be expressed as:

$$\frac{d[S_1]}{dt} = -(k_F + k_{ISC} + k_{nr}^{S_1})[S_1] + k_{RISC}[T_1] + \frac{1}{2}(k_{TTA}[T_1]^2) \qquad (6.2a)$$

$$\frac{d[T_1]}{dt} = k_{ISC}[S_1] - (k_{Ph} + k_{RISC} + k_{nr}^{T_1})[T_1] - 2(k_{TTA}[T_1]^2) \qquad (6.2b)$$

where k_F, k_{Ph} k_{ISC}, k_{RISC}, k_{TTA}, $k_{nr}^{S_1}$, and $k_{nr}^{T_1}$ are the rate constants for fluorescence, phosphorescence, intersystem crossing, reverse intersystem crossing, triplet-triplet annihilation, and non-radiative recombination from S_1 and T_1 states, respectively. As was discussed in Section 6.2, $k_F \sim k_{nr}^{S_1} \gg k_{ISC} \sim k_{RISC}$, and accordingly, during the prompt emission regime of the overall scintillation decay, the vast majority of the initial population of S_1 states will have been depleted due to the combination of fluorescence, non-radiative relaxation, and conversion to T_1 via intersystem crossing. As such, during the delayed emission regime, the overall population $[S_1]$ is very low, and thus can be neglected from the treatment of $[T_1]$ in Equation (6.2b) (i.e., repopulation of T_1 states from S_1 states can be ignored in this regime), which will also mean that k_{ISC} can be neglected as well from Equation (6.2a). Furthermore, since the rate constants of phosphorescence and non-radiative recombination from T_1 states are typically on the order of ms−1 to s−1 for organic compounds, we can additionally neglect these rate constants (k_{Ph} and $k_{nr}^{T_1}$, respectively), so that Equations (6.2a) and (6.2b) can be re-expressed for the delayed emission regime as:

$$\frac{d[S_1]}{dt} \simeq -(k_F + k_{nr}^{S_1})[S_1] + k_{RISC}[T_1] + \frac{1}{2}(k_{TTA}[T_1]^2) \qquad (6.3a)$$

$$\frac{d[T_1]}{dt} \simeq -k_{RISC}[T_1] - 2(k_{TTA}[T_1]^2) \qquad (6.3b)$$

In reality, a precise treatment of the S_1 and T_1 states in TADF capable scintillators will be further complicated by the fact that expressions for $[S_1]$ and $[T_1]$ will have additional terms that depend on the local concentration of excited states in the vicinity of the incident particle track (which in turn will depend on the specific energy loss of the particle) as well as diffusional terms for S_1 and T_1 states.[5,72] However, as a first-order approximation, we

85

can neglect these terms, and use the expressions in Equations (6.3a) and (6.3b) to make a qualitative assessment of the competition between the TADF and triplet-triplet annihilation mechanisms in determining the behavior of the delayed fluorescence in experimental scintillation decay measurements. Again, because $k_F \sim k_{nr}^{S_1} \gg k_{RISC}$, and if we can further assume that $k_{RISC} \sim k_{TTA}$, then the expression for [S$_1$] in Equation (6.3a) implies that relaxation from S$_1$ states is so fast as to quickly deplete any additional S$_1$ states generated from the T$_1$ population, to give the delayed fluorescence photons that are observed. Accordingly, the kinetics of the observed delayed fluorescence will be totally dominated by the k_{RISC}[T$_1$] and k_{TTA}[T$_1$]^2 terms that appear in both Equations (6.3a) and (6.3b), i.e., the conversion of T$_1$ to S$_1$ states. Moreover, it can be clearly seen from this analysis that both of these processes will be expected to be operative simultaneously during the delayed emission regime, but because of the second order dependency of triplet-triplet annihilation on [T$_1$], conversion of T$_1$ to S$_1$ states via the triplet-triplet annihilation mechanism will be most significant when [T$_1$] is highest, i.e., just after the end of the prompt fluorescence, before diffusional processes and conversion of T$_1$ states have significantly lowered both the local and overall values of [T$_1$]. Over longer timescales, when [T$_1$] has been sufficiently decreased, the k_{RISC}[T$_1$] term should become dominant, where the majority of T$_1$ to S$_1$ conversion is occurring via the TADF mechanism. Therefore, the decay of the delayed emission for TADF capable scintillators, when examined over sufficiently long timescales, should eventually converge toward simple exponential decay characterized entirely by k_{RISC}. The time required before the exponential decay of the reverse intersystem crossing conversion mechanism becomes the dominant decay process will correspondingly depend on the relative magnitudes of the k_{RISC} and k_{TTA} rate constants.

In order to analyze the experimental data obtained from the scintillation decays obtained for the TADF-based plastic scintillators being investigated, scintillation decay curves were obtained via a time-correlated single photon counting (TCSPC) approach (see Appendix B.2 for experimental details) over a 5 µs timescale. Figure 6.23 compares the peak-normalized scintillation decays for Meta-Octyl-Dye in poly(vinyl toluene) samples over the primary dye loading range of 1–15 wt.%, while Figure 6.24 displays the corresponding decay curves for

(a) 1 wt.%

(b) 5 wt.%

(c) 10 wt.%

(d) 15 wt.%

Figure 6.23: Comparison of ^{137}Cs scintillation decays of Meta-Octyl-Dye in poly(vinyl toluene) samples with the respective primary dye loadings indicated; exponential fittings of the slow decay component over the 1–5 µs decay period are overlaid (red and dashed).

the wavelength shifted Meta-Octyl-Dye in poly(vinyl toluene) samples over the primary dye loading range of 1–10 wt.%. Plotted as well in these figures are exponential fittings carried out over the 1–5 µs region of the decay curves. For fluorescence lifetimes in the range of 1–15 ns, after 100–150 ns (a minimum of 10 lifetimes), the delayed fluorescence is the dominant emission process, and as can be seen from the experimental decays, between ~100 ns – 1 µs, the observed decays are completely non exponential, but after 1 µs, begin to be more closely described by the exponential fitting carried out over this time-span. Furthermore, it can be seen simply from visual inspection that for increasing primary dye content, the deviation of the experimental curve from the exponential fit is further reduced,

(a) 1 wt.%

(b) 5 wt.%

(c) 10 wt.%
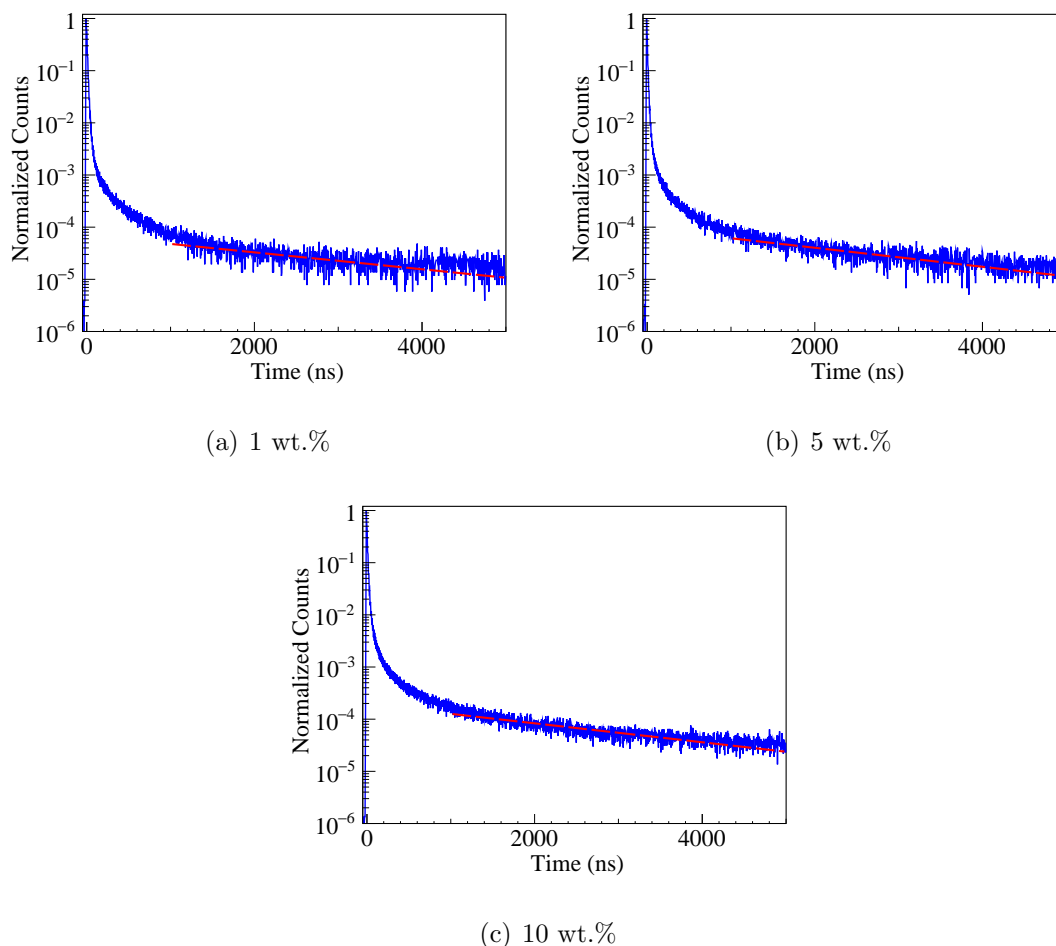
Figure 6.24: Comparison of ^{137}Cs scintillation decays of wavelength shifted Meta-Octyl-Dye in poly(vinyl toluene) samples with the respective primary dye loadings indicated; exponential fittings of the slow decay component over the 1–5 μs decay period are overlaid (red and dashed).

an observation that provides direct evidence of the increasing degree of T_1 to S_1 conversion with primary dye content due to the reverse intersystem crossing process of the overall TADF mechanism. At lower dye loadings, where the matrix to primary dye energy transfer is less efficient, the lifetime of T_1 states on the matrix polymer could be sufficiently long (i.e., before being transferred to the primary dye) to allow for some degree of triplet-triplet annihilation occuring between matrix T_1 states, to S_1 matrix states that are either radiatively emitted directly by the matrix polymer, or ultimately transfered to the primary dye for radiative emission, but since the photoluminescent efficiency of poly(vinyl toluene) is very

low ($\Phi_{\text{PL}} = 0.07$),[55] the latter outcome is far more probable. Since T_1 to S_1 conversion via a TADF mechanism can only occur on the primary dye, for low primary dye loadings with inefficient matrix to primary dye energy transfer, there will be a lower degree of T_1 conversion via reverse intersystem crossing, as compared to a higher primary dye loading such that the energy transfer from the matrix is highly efficient. The practical consequence of these differences due to primary dye loading is that at low loadings, triplet-triplet annihilation will continue to dominate the delayed emission behavior at longer time scales as compared to higher primary dye loadings, the latter of which will correspondingly display more ideally exponential behavior in the decay of the delayed emission during these time scales.

Another notable feature of the decay curves in Figures 6.23 and 6.24 is that the total fraction of the delayed emission over the observed timescale is steadily increasing with increased primary dye loadings. Similar behavior was noted and discussed in Section 5.7 for the DPA-DHS based scintillators, being attributable to increased ease of triplet-triplet annihilation for higher primary dye loading, especially when considering that at low loadings, the primary dye will act like a trap-state impeding the diffusion of T_1 states, thus inhibiting the overall triplet-triplet annihilation process. In the present case of TADF-capable scintillators, both cases of either triplet-triplet annihilation or TADF mediated T_1 to S_1 conversion should be enhanced by increased primary dye loading, and for TADF in particular, this is more simply attributable to the increased efficiency in the energy transfer from the matrix to the primary dye, especially given the unimolecular nature of the reverse intersystem crossing process.

As was already mentioned, the balance between T_1 to S_1 conversion via the reverse intersystem crossing or triplet-triplet annihilation mechanism is mediated by the relative magnitudes of their rate constants, k_{RISC} and k_{TTA}, respectively. For the TADF mechanism, the magnitude of k_{RISC} (and correspondingly k_{ISC}) depends on the singlet-triplet splitting of the primary dye according to a Boltzmann relation:[51]

$$k_{RISC} \propto \exp\left(-\frac{\Delta E_{\text{ST}}}{k_B T}\right) \tag{6.4}$$

The effects of the singlet-triplet splitting on the kinetics of the delayed emission processes of TADF-based scintillators is well illustrated through comparison of the decay curves of Para-

(a) 1 wt.%

(b) 5 wt.%

(c) 7.5 wt.%

(d) 9 wt.%
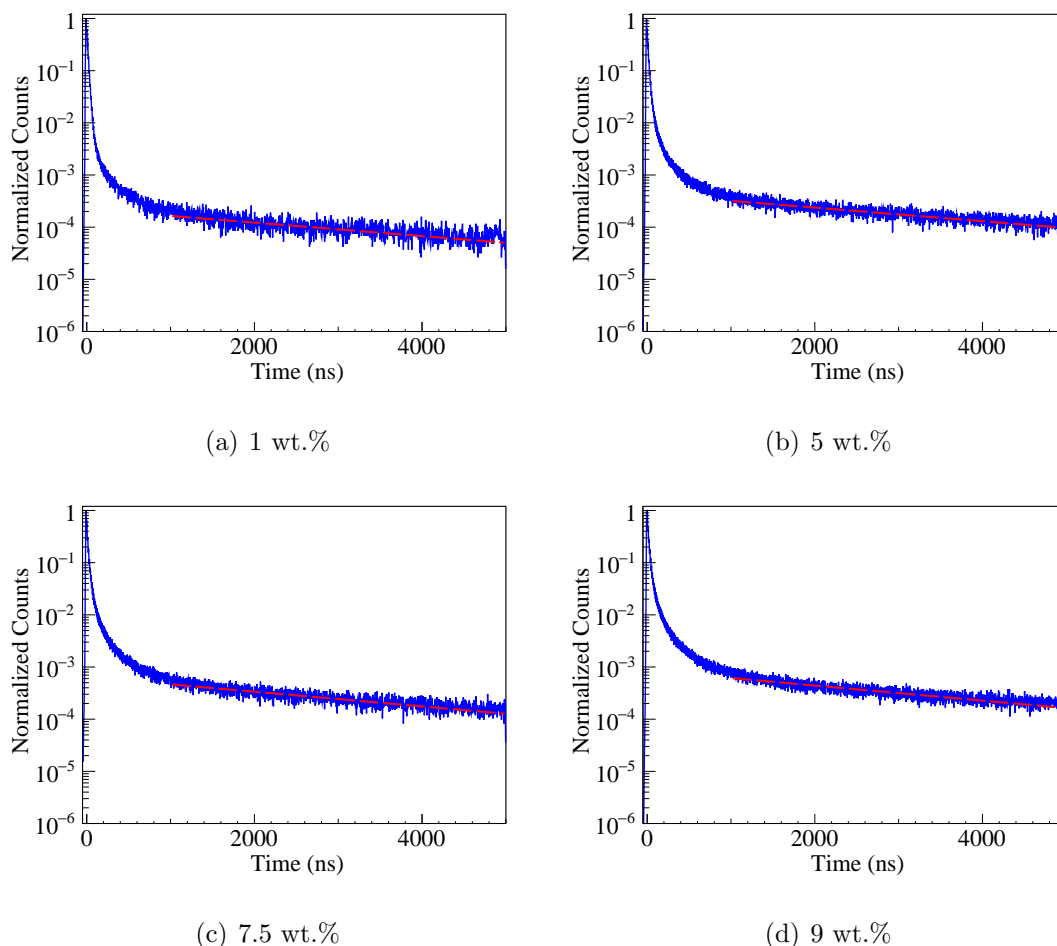
Figure 6.25: Comparison of ^{137}Cs scintillation decays of Para-Octyl-Dye in poly(vinyl toluene) samples with the respective primary dye loadings indicated; exponential fittings of the slow decay component over the 1–5 μs decay period are overlaid (red and dashed).

Octyl-Dye based scintillator samples with the aforementioned samples based on the Meta-Octyl-Dye primary dye. Figures 6.25 and 6.26 compare the peak-normalized scintillation decays of of Para-Octyl-Dye in poly(vinyl toluene) and wavelength shifted Para-Octyl-Dye in poly(vinyl toluene) samples, respectively, both the primary dye loading range of 1–9 wt.%. Like the decay curves for Meta-Octyl-Dye based samples shown in Figures 6.23 and 6.24, the decays curves for Para-Octyl-Dye based samples are fitted to an exponential over the 1–5 μs timespan. Also like the Meta-Octyl-Dye based samples, the slow decay of these curves show improved quality of the fit to their exponential descriptors with increased primary dye content, again indicating that the increased role of the reverse intersystem

(a) 1 wt.%

(b) 5 wt.%
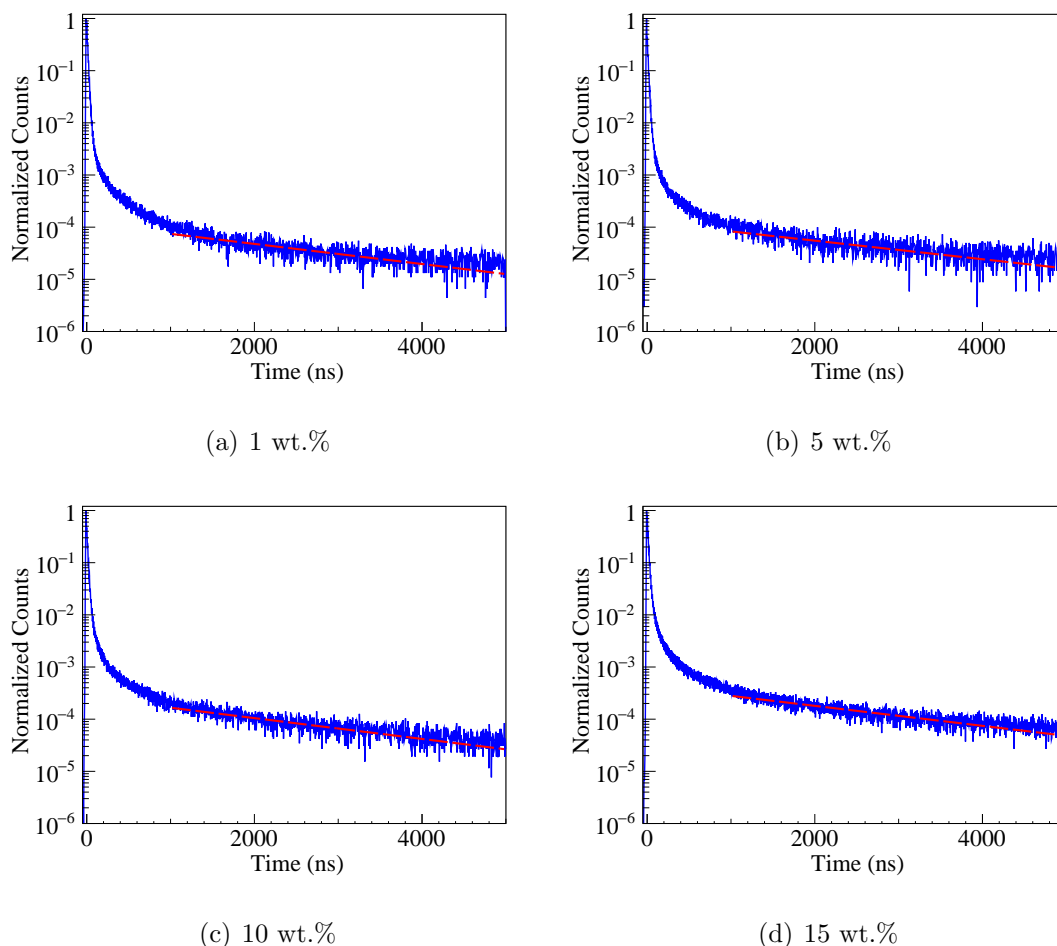
(c) 7.5 wt.%

(d) 9 wt.%
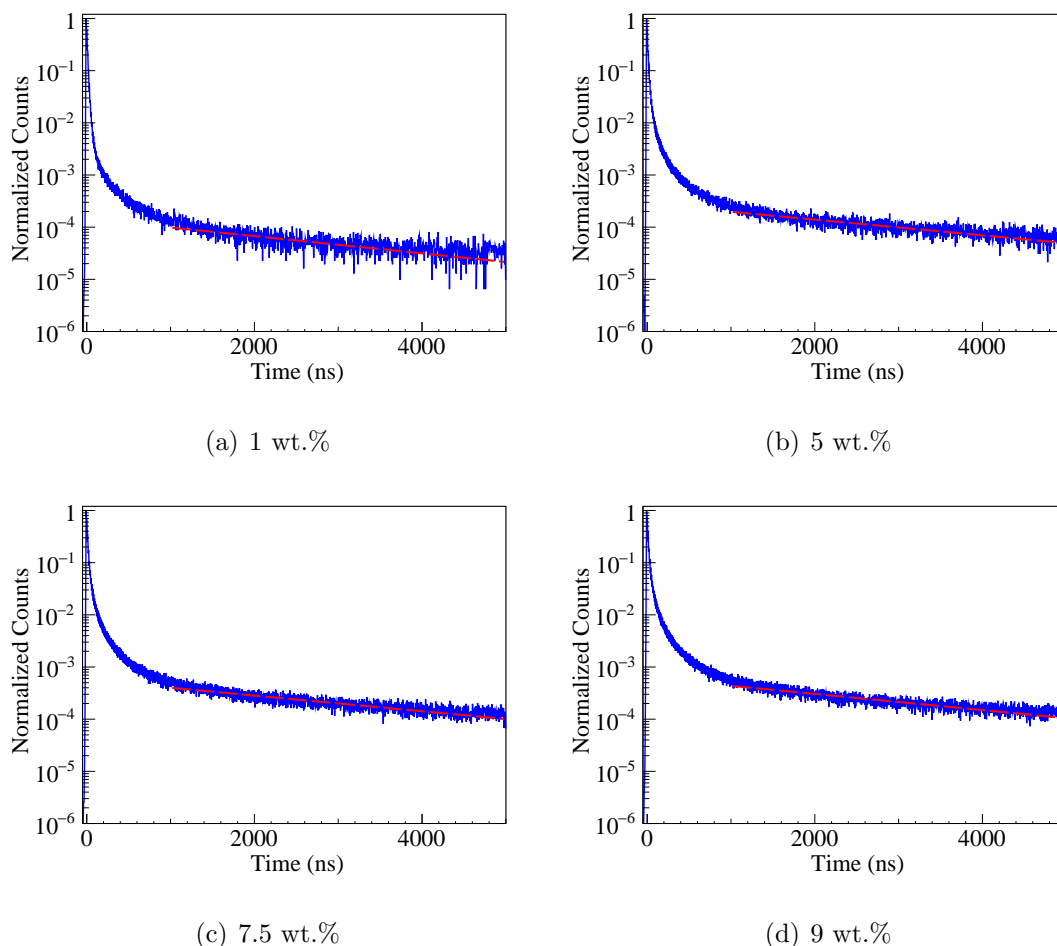
Figure 6.26: Comparison of ^{137}Cs scintillation decays of wavelength shifted Para-Octyl-Dye in poly(vinyl toluene) samples with the respective primary dye loadings indicated; exponential fittings of the slow decay component over the 1–5 µs decay period are overlaid (red and dashed).

crossing process in T_1 to S_1 conversion as the primary dye content is increased. Moreover, the overall quality of the exponential fits could easily be seen through visual inspection to be consistently better descriptors of the delayed emission behavior over this timescale as compared to the Meta-Octyl-Dye samples, which is indicative of the enhanced k_{RISC} due to the lower singlet-triplet splitting of Para-Octyl-Dye. The total fraction of delayed emission for the Para-Octyl-Dye samples was also found to be increasing with increased primary dye content, and furthermore, the decay curves in Figures 6.25 and 6.26 also display delayed emissions that make up markedly greater fractions of the total emission intensity, as

compared to Meta-Octyl-Dye based samples, at any given primary dye loading. Again, this is a direct consequence of Para-Octyl-Dye's reduced singlet-triplet splitting, and offers direct evidence to suggest that overall, Para-Octyl-Dye is significantly better at facilitating T_1 to S_1 conversion. This gives further insight into the observations of higher light yields for the Para-Octyl-Dye in poly(vinyl toluene) samples as compared to Meta-Octyl-Dye in poly(vinyl toluene), as was mentioned in Section 6.6, as the increased ability to convert triplet states originating from the primary ion-recombination processes along the incident particle track results in enhanced S_1 populations and a greater absolute number of scintillation photons, despite the reduced photoluminescence quantum yield of Para-Octyl-Dye as compared to Meta-Octyl-Dye. In particular, these findings suggest that TADF-capable scintillating dyes, when properly designed and engineered to have all of the optimal properties for scintillation applications (photoluminescence quantum yield in particular), could be a viable approach to achieving dramatic improvement in the light yields of organic scintillators, beyond what is currently capable with existing materials based on traditional fluorescent dyes.

Taken from the decay curve data displayed in Figures 6.23 to 6.26, Table 6.4 lists the experimental lifetimes obtained from exponential fittings of both the fast and slow components of the scintillation decay curves. For the exponential fits of the delayed emission, Table 6.4 also includes the calculated symmetric mean absolute percentage errors (SMAPEs), which are calculated from the decay curve data over the fitting interval according to the following formula:[73,74]

$$\text{SMAPE} = \frac{100\%}{n} \sum_{i=1}^{n} \frac{|f_i - a_i|}{(|a_i| + |f_i|)/2}, \tag{6.5}$$

where a_i and f_i are the measured and fitted data points, respectively. These numerical values of the total error of the exponential fits provide a quantitative counterpart to the visual inspection of the fit qualities that was mentioned for the data in Figures 6.23 to 6.26. What is particularly noteworthy about these error estimates is they confirm the prior assessment that in general, the delayed emissions for the Para-Octyl-Dye samples are more closely approximated by their exponential fittings than the Meta-Octyl-Dye samples, which again is a direct consequence of the reduced singlet-triplet splitting for the former primary dye.

Material	Primary Dye Loading (wt.%)	Fast Decay (ns)	Slow Decay (µs)	SMAPE of Slow Decay Fit (%)
Meta-Octyl-Dye in poly(vinyl toluene)	1	13.3	2.25	5.6
	5	12.1	2.44	5.7
	10	13.2	2.18	5.3
	15	14.1	2.27	5.0
wavelength shifted Meta-Octyl-Dye in poly(vinyl toluene)	1	9.2	2.68	5.8
	5	7.6	2.38	5.4
	10	8.0	2.39	4.8
Para-Octyl-Dye in poly(vinyl toluene)	1	16.6	3.37	5.2
	5	16.3	3.34	4.6
	7.5	16.4	3.09	4.7
	9	16.4	3.01	4.6
wavelength shifted Para-Octyl-Dye in poly(vinyl toluene)	1	11.2	2.63	5.5
	5	10.2	2.89	4.8
	7.5	11.4	2.89	4.7
	9	11.1	2.80	4.6

Table 6.4: ^{137}Cs decay lifetimes for TADF-based plastic scintillator samples.

6.8 TADF Scintillator α/γ Pulse Shape Discrimination Performance

Figure 6.27 plots the 2-dimensional α/γ PSD histograms for of (Q_{tail}/Q_{total}) versus energy for representative samples of Meta-Octyl-Dye in poly(vinyl toluene), while Figure 6.28 and Figure 6.29 display the corresponding data obtained for representative samples of Meta-Octyl-Dye in crosslinked poly(vinyl toluene) and wavelength shifted Meta-Octyl-Dye in poly(vinyl toluene), respectively. Using the data shown in these and additional PSD plots obtained over the full range of primary dye loadings for each material system, PSD figure-of-merits
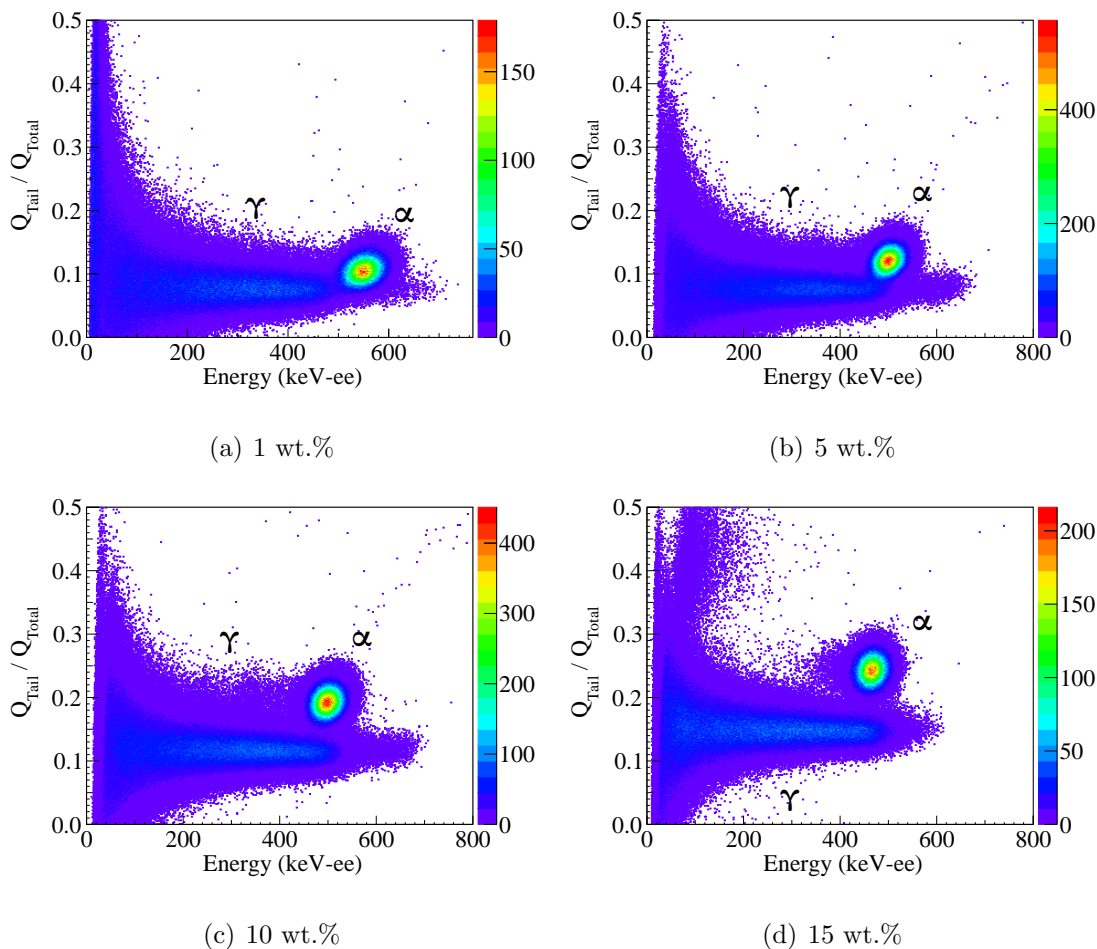
Figure 6.27: Representative ^{210}Po/^{137}Cs PSD plots of Meta-Octyl-Dye in poly(vinyl toluene) scintillator samples with the respective primary dye loadings indicated.

(FOMs) were determined according to Equation (4.2), using a 100 keV threshold energy, and the combined FOM results are plotted in Figure 6.30 as a function of primary dye loading. Generally speaking, at or below 7.5 wt.% loading of Meta-Octyl-Dye, the PSD FOMs for all three materials systems was found to be reasonably similar to one another, with the general trend of increasing FOM with increased primary dye content. Interestingly, in this region, and continued up to 10 wt.%, no additional performance gains were observed for the wavelength shifted Meta-Octyl-Dye in poly(vinyl toluene) system (Figure 6.29), as compared to the unshifted Meta-Octyl-Dye in poly(vinyl toluene) performance, and because of this lack of overall improvement in performance for the wavelength shifted Meta-Octyl-Dye in poly(vinyl toluene) samples, no further attempts were made to prepare samples with primary dye load-
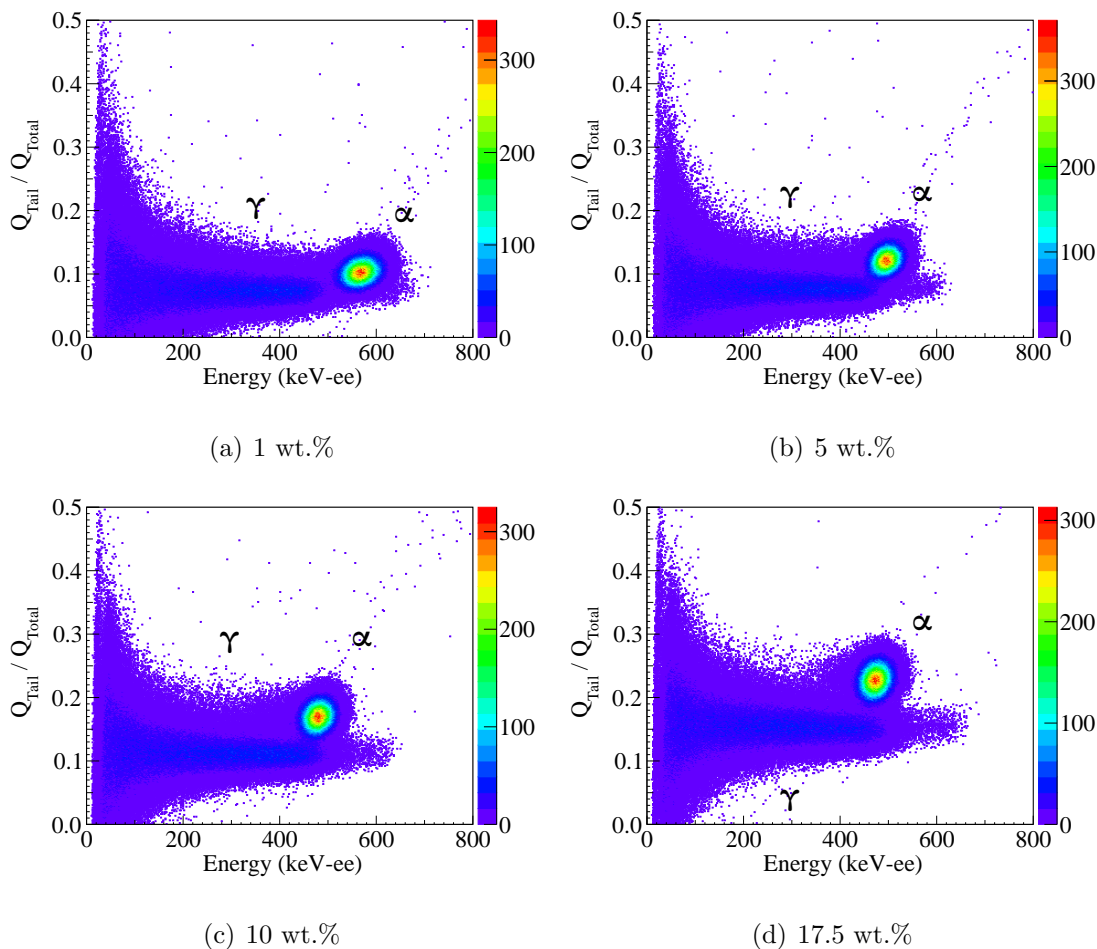
Figure 6.28: Representative ^{210}Po/^{137}Cs PSD plots of Meta-Octyl-Dye in crosslinked poly(vinyl toluene) scintillator samples with the respective primary dye loadings indicated.

ings beyond 10 wt.%. While this is seemingly contradictory to the fact that the wavelength shifted Meta-Octyl-Dye in poly(vinyl toluene) samples did display in Figure 6.21 notably improved light yields over Meta-Octyl-Dye in poly(vinyl toluene) samples, it should be again noted that the light yields presented in Figure 6.21 have been corrected to account for the emission and quantum yield spectra of the sample and photomultiplier tube photocathode, respectively. As such, these corrected light yield values are not directly indicative of the potential PSD performance of a given material, and thus the relation between the emission spectrum of the sample and the quantum efficiency spectrum of the photodetector must be explicitly considered. Given that the emission spectrum of the DPAVB shifted samples is pushed further towards longer wavelengths outside of the peak photomultiplier tube photo-
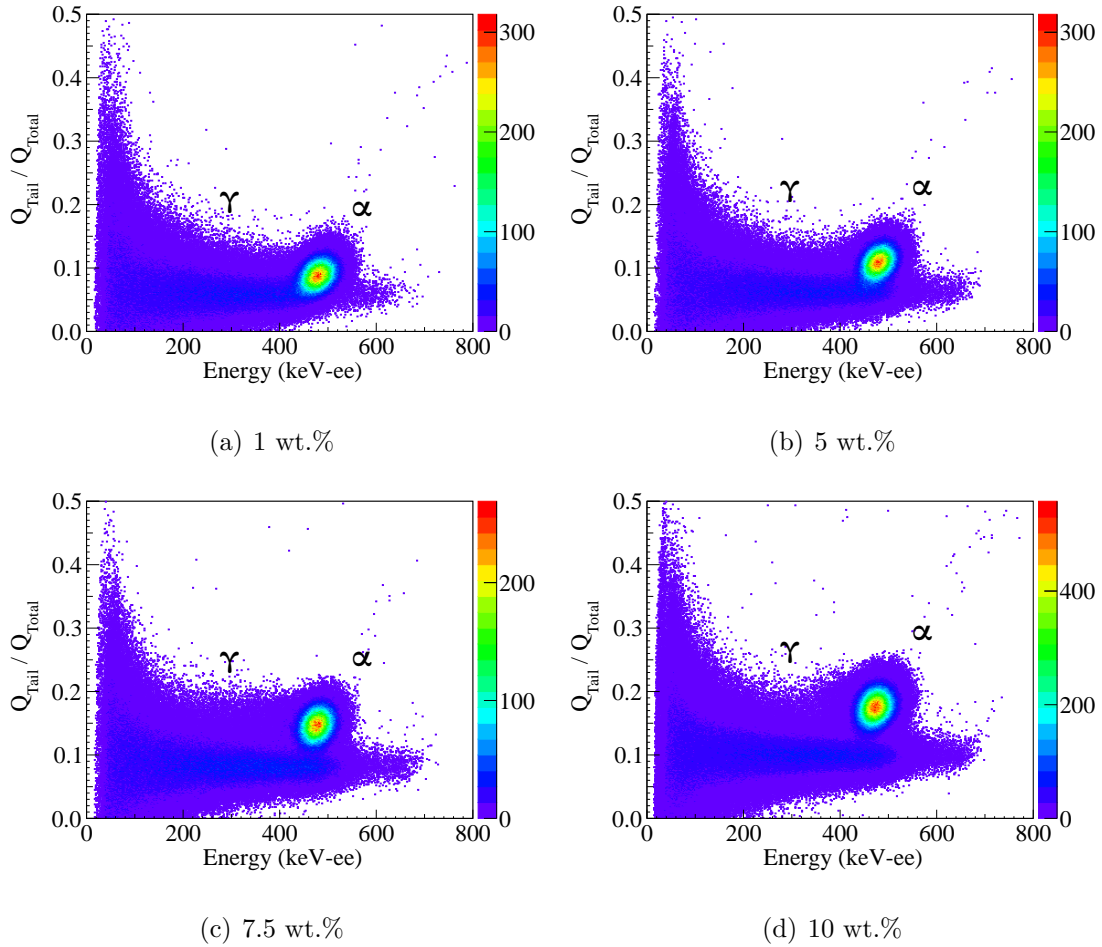
Figure 6.29: Representative ^{210}Po/^{137}Cs PSD plots of wavelength shifted Meta-Octyl-Dye in poly(vinyl toluene) scintillator samples with the respective primary dye loadings indicated.

cathode quantum efficiency, it would appear to be the case that any gains in the raw number of photons generated by the use of the wavelength shifting secondary dye DPAVB is totally offset by the losses in the photocathode's quantum efficiency, resulting in no net gain in the number of *detected* photons, and correspondingly no discernible increase in the overall PSD performance. Furthermore, as the corrected light yields shown in Figure 6.21 for wavelength shifted Meta-Octyl-Dye in poly(vinyl toluene) samples were found to be steadily decreasing with primary dye loadings above 5 wt.%, any additional gains in the PSD performance to be expected from the reduction of self absorption (due to increasing primary dye content) would again be counteracted by the overall light yield losses in this loading region.

Unlike the case for the wavelength shifted Meta-Octyl-Dye in poly(vinyl toluene) system,
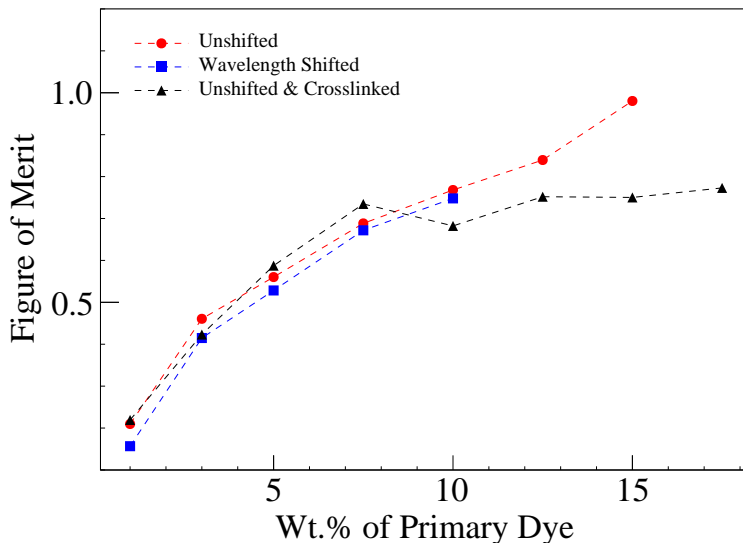
Figure 6.30: Comparison of PSD figure-of-merits obtained using a 100 keV threshold energy for Meta-Octyl-Dye in poly(vinyl toluene), wavelength shifted Meta-Octyl-Dye in poly(vinyl toluene), and Meta-Octyl-Dye in crosslinked poly(vinyl toluene) scintillator samples as a function of primary dye loading.

the crosslinked Meta-Octyl-Dye in crosslinked poly(vinyl toluene) samples showed significant departure from the behavior of the uncrosslinked Meta-Octyl-Dye in poly(vinyl toluene) at primary dye loading above 7.5 wt.%, with the crosslinked Meta-Octyl-Dye in crosslinked poly(vinyl toluene) samples displaying a relatively unchanged FOM for all samples at or above 7.5 wt.%. In contrast, Meta-Octyl-Dye in poly(vinyl toluene) samples displayed a steady monotonic increase in FOM with primary dye loading, up to a maximum value of 0.98 at primary dye content of 15 wt.%, the highest Meta-Octyl-Dye loading that was achieved for uncrosslinked samples that did not result in a total loss of sample transparency. Again, the likely cause of the discrepancy in PSD performance between these two systems relates to the light yield data presented in Figure 6.21, although in this case the corrected light yield data is directly applicable, since the emission spectra of Meta-Octyl-Dye in poly(vinyl toluene) and Meta-Octyl-Dye in crosslinked poly(vinyl toluene) (Figures 6.12(b) and 6.14(b), respectively) show no readily discernible differences for any particular primary dye loading. As such, the decreased PSD performance observed for the crosslinked Meta-Octyl-Dye in

crosslinked poly(vinyl toluene) samples at higher primary dye loadings is directly attributable to their reduced light yield, which as was mentioned in Section 6.6 is likely attributable to quenching by residual vinyl groups of partially or unreacted monomers. The lack of any significant improvement in the PSD performance of the crosslinked Meta-Octyl-Dye in crosslinked poly(vinyl toluene) samples for primary dye loadings above 7.5 wt.% resulted in no loadings in excess of 17.5 wt.% being examined during the course of this work.

In light of the observation that of the three material systems presented in Figures 6.27 to 6.30, Meta-Octyl-Dye in poly(vinyl toluene) (and to a slightly lesser extent wavelength shifted Meta-Octyl-Dye in poly(vinyl toluene)) showed overall the best and most consistent PSD performance, additional consideration was given to the assessing how the observed performances relate to plastic scintillators based on conventional fluorescent dyes. Moreover, given that Meta-Octyl-Dye and Para-Octyl-Dye have a relatively high molecular weight (compared to typical scintillating dyes), it is important to determine how the PSD performance relates to typical fluorescent dyes not only in terms of the best FOM attainable, but also how the FOMs for the primary loading range shown in Figure 6.30 compares to equivalent loading ranges for typical fluorescent scintillating dyes when expressed over the same *concentration* range, to account for the differences in dye molecular weight. To make such a comparison, α/γ PSD measurements were obtained for two series of plastic scintillators using either 2,5-Diphenyloxazole or 9,10-Diphenylanthracene in poly(vinyl toluene), the results of which are presented along with the α/γ PSD data obtained for Meta-Octyl-Dye in poly(vinyl toluene) in Figure 6.31. 2,5-Diphenyloxazole and 9,10-Diphenylanthracene based plastic scintillators were chosen for this comparison, and 2,5-Diphenyloxazole in particular, due to its high solubility in poly(vinyl toluene) forms the basis of the current generation of PSD capable plastics, and is essentially a *de facto* reference material for PSD plastics.[21] Primary dye loadings for 2,5-Diphenyloxazole in poly(vinyl toluene) ranged from 0.2–2.0 wt.%, and 0.3–2.9 wt.% for 9,10-Diphenylanthracene in poly(vinyl toluene), which on a concentration basis equates to ∼10–90 µmol/g. At these loadings, the effects of self absorption are relatively minor in comparison to the self absorption effects in highly loaded PSD-capable plastics, and no additional wavelength shifter was employed for these materials, further keeping them in
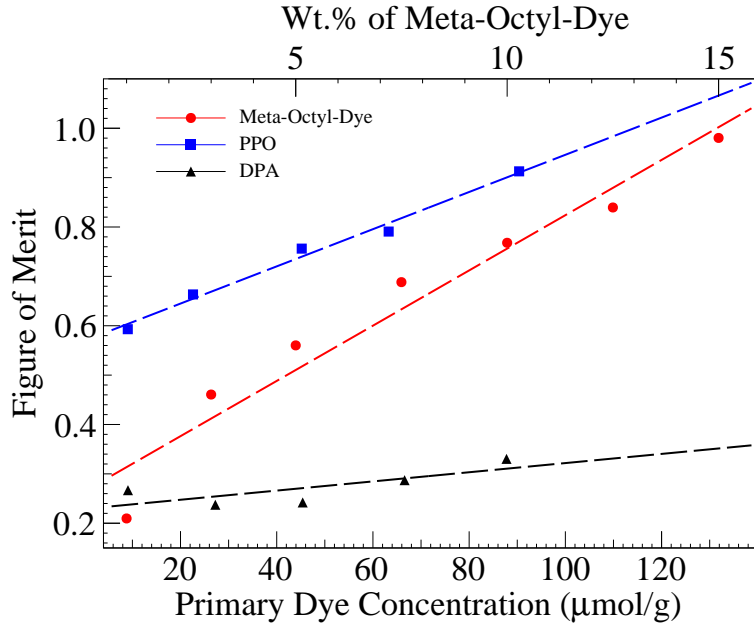
Figure 6.31: Comparison based on primary dye concentration of PSD figure-of-merits for Meta-Octyl-Dye in poly(vinyl toluene), 2,5-Diphenyloxazole in poly(vinyl toluene) (PPO), and 9,10-Diphenylanthracene in poly(vinyl toluene) (DPA) scintillator samples.

accordance with the unshifted Meta-Octyl-Dye in poly(vinyl toluene) under examination. For Meta-Octyl-Dye in poly(vinyl toluene), this concentration range corresponds to primary dye loadings in the range from 1–10 wt.%, which is accordingly ~3.5 times higher than 9,10-Diphenylanthracene in poly(vinyl toluene) and ~5 times higher than 2,5-Diphenyloxazole in poly(vinyl toluene) when expressed on a weight percentage basis. This again is a consequence of the high molecular weight of both Meta-Octyl-Dye and Para-Octyl-Dye, and it is interesting to note that on a concentration basis, the TADF dye loadings explored in this work are very much within the range of conventional plastic scintillators (i.e., not highly loaded for PSD capability). What is quite notable about the data presented in Figure 6.31 is that both Meta-Octyl-Dye in poly(vinyl toluene) and 2,5-Diphenyloxazole in poly(vinyl toluene) show strong monotonic trends of increasing FOM with increased primary dye concentration. While the 2,5-Diphenyloxazole in poly(vinyl toluene) samples were observed to outperform the Meta-Octyl-Dye in poly(vinyl toluene) samples over the concentration range tested, the performance of Meta-Octyl-Dye can be seen to be increasing at a faster

rate with increased concentration, so presumably there would be primary dye concentration where the Meta-Octyl-Dye in poly(vinyl toluene) performance would become higher, if not for the fact that such a concentration lies outside the Meta-Octyl-Dye solubility range. On the other hand, it should be noted that for 2,5-Diphenyloxazole, both its emission spectrum and quantum yield (peak emission $\sim$355 nm, $\Phi_{PL} = 1.00$)[55] make it a much more ideal scintillating dye than Meta-Octyl-Dye, which is less than ideal in terms of emission wavelength and quantum yield (Table 6.3). As such, the fact that Meta-Octyl-Dye in poly(vinyl toluene) samples demonstrated only moderately lower overall PSD performance is a clear validation of the efficacy of the TADF approach to achieving PSD behavior, and with the expense of sufficient effort to design new TADF dyes with photophysical properties (especially emission wavelength and photoluminescence quantum yield) ideally suited towards scintillator applications, TADF dyes could become ideal candidates for the next generation of scintillating dyes in high performance PSD-capable plastics.

Another quite striking observation about the data presented in Figure 6.31 is that the performance of the 9,10-Diphenylanthracene in poly(vinyl toluene) samples over this primary dye loading range was found to be considerably worse than either the Meta-Octyl-Dye in poly(vinyl toluene) or 2,5-Diphenyloxazole in poly(vinyl toluene) samples, which is quite striking, given that 9,10-Diphenylanthracene has been demonstrated to have good PSD performance in single crystal form.[32–34] Furthermore, these observations offer a further degree of explanation of the poorer performance of the DPA-DHS based plastic scintillator samples that were discussed in detail in Chapter 5. In particular, light yield measurements performed on 9,10-Diphenylanthracene in poly(vinyl toluene) samples over a similar primary dye loading range (Figure 5.6) showed tight agreement with the light yield data for the DPA-DHS/PVT scintillators under investigation, suggesting that at least at low primary dye concentration, 9,10-Diphenylanthracene and DPA-DHS possess essentially the same basic scintillation performance. If the same holds true at higher concentrations, then the data for 9,10-Diphenylanthracene in poly(vinyl toluene) in Figure 6.31, along with the PSD performance of DPA-DHS scintillators in Figure 5.12, would suggest that 9,10-Diphenylanthracene (and similar derivatives) has fundamentally poorer PSD performance in plastic media, in a

rather striking departure from its behavior in the single crystal phase. This would actually offer additional support to the overall strategy of highly-loaded PSD capable plastics stabilized via dye compolymerization (the overarching focus of Chapter 5), and suggests that with a better choice of scintillating dye, practical PSD-capable plastics would be readily achievable.

In contrast to the Meta-Octyl-Dye based samples, plastic scintillators prepared using the Para-Octyl-Dye dye generally displayed inferior PSD performance, and Figures 6.33 and 6.33 plot the 2-dimensional α/γ PSD histograms for representative samples of Para-Octyl-Dye in poly(vinyl toluene) and wavelength shifted Para-Octyl-Dye in poly(vinyl toluene), respectively, while Figure 6.34 plots the combined FOM results for the entire primary lye loading ranges using the same 100 keV threshold energy used for the results displayed in Figure 6.30. In Figure 6.34, only modest change in the overall PSD performance is observable over the range of primary dye loadings tested, with the Para-Octyl-Dye in poly(vinyl toluene) FOMs rising from 0.42 at 1 wt.% of primary dye to a maximum of 0.59 at 9 wt.%. Higher than 9 wt.%, a slight drop-off in the FOMs is observed, which is easily attributable to the total loss of transparency of 10 wt.% Para-Octyl-Dye that can be seen in Figure 6.17. Somewhat lower PSD performance was observed for the wavelength shifted Para-Octyl-Dye in poly(vinyl toluene) samples, which increased in FOM with primary dye loading from 0.34 at 1 wt.% to 0.54 at 5 wt.%, and remained at relatively unchanged upon increasing primary dye content up to 9 wt.%, the highest loading tested for this material system. Overall, the trends in PSD performance for both Para-Octyl-Dye based scintillator systems shows reasonable agreement with the light yield data shown in Figure 6.22, in particular the lower PSD performance of the wavelength shifted Para-Octyl-Dye in poly(vinyl toluene) samples, for which lower light yields as compared to the unshifted Para-Octyl-Dye in poly(vinyl toluene) samples were observed for primary dye loadings above 3 wt.%. As such, the combination of both the lower light yields and longer wavelength emission spectra (Figure 6.20) of the wavelength shifted Meta-Octyl-Dye in poly(vinyl toluene) samples is a plainly attributable explanation for the reduced PSD performance, as compared to the unshifted Para-Octyl-Dye in poly(vinyl toluene) samples.
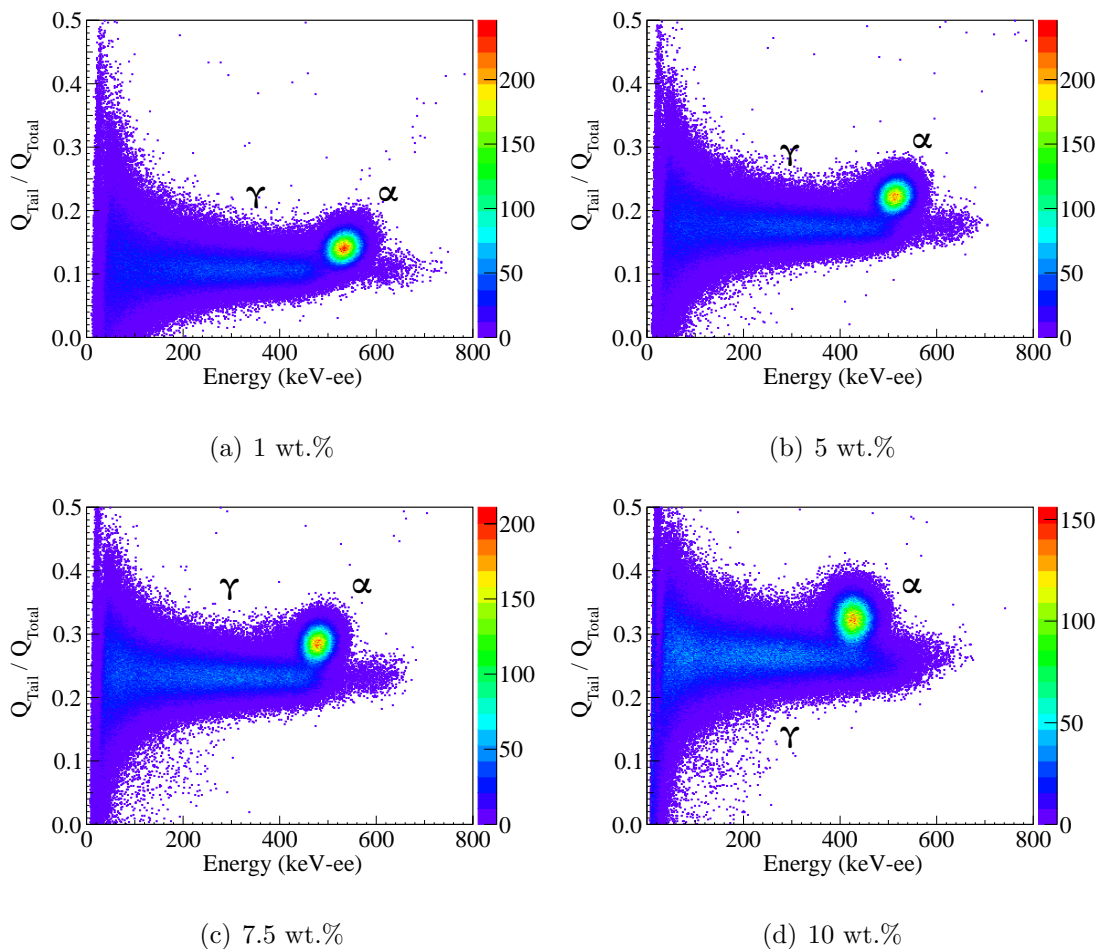
Figure 6.32: Representative ^{210}Po/^{137}Cs PSD plots of Para-Octyl-Dye in poly(vinyl toluene) scintillator samples with the respective primary dye loadings indicated.

What is less straight forward about the FOM data in Figure 6.34 is any explanation for the relative lack of overall PSD performance for Para-Octyl-Dye based scintillators, at least when compared directly to those based on Meta-Octyl-Dye (Figure 6.30). Presumably, one might predict that Para-Octyl-Dye should have better PSD capability than Meta-Octyl-Dye, especially when considering the fact that Para-Octyl-Dye has a lower singlet-triplet splitting, and thus possess a greater ease in T_1 to S_1 conversion, as was discussed in detail in Section 6.7. However, because of the fact that that the intersystem crossing rate constant (k_{ISC}), which governs the rate of S_1 to T_1 conversion, is (along with k_{RISC}) inversely related to the singlet-triplet splitting, in the early time-frame of the scintillation pulse (when the S_1 population is highest), there is a certain amount of S_1 to T_1 conversion that occurs,
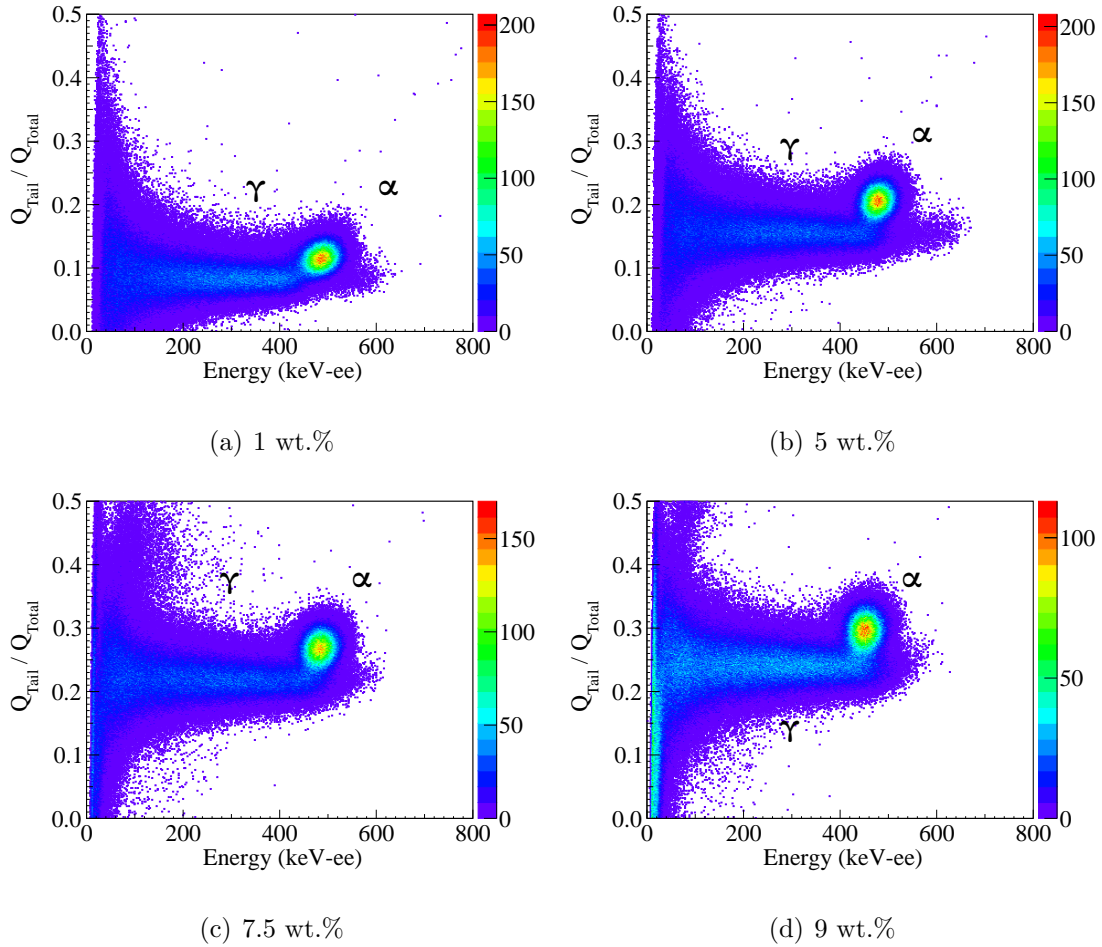
Figure 6.33: Representative ^{210}Po/^{137}Cs PSD plots of wavelength shifted Para-Octyl-Dye in poly(vinyl toluene) scintillator samples with the respective primary dye loadings indicated.

regardless of the number of additional T_1 states that are generated through the conventional scintillation processes such as ion recombination. The magnitude of this S_1 to T_1 conversion will correspondingly depend on the magnitude of the singlet-triplet splitting, and thus for TADF scintillators, the initial population of T_1 states in the early pulse time-frame will depend not only on the specific energy loss of the incident particle, but also on the singlet-triplet splitting of the primary dye. A consequence of these factors is that for a fixed primary dye loading and incident particle, samples based on Para-Octyl-Dye should exhibit delayed emissions that make up a greater fraction of the total emission as compared to samples based on Meta-Octyl-Dye, due to their higher initial T_1 populations, which is plainly observable in the scintillation decay shown in Figures 6.23 to 6.26. This increase of
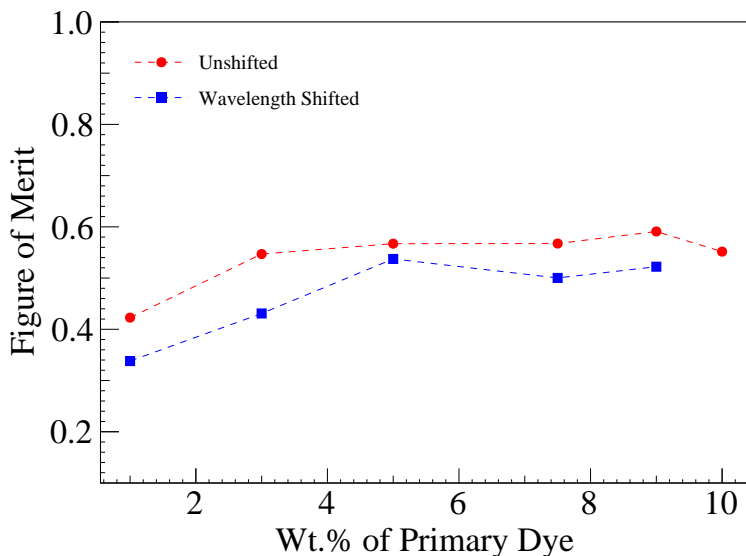
Figure 6.34: Comparison of PSD figure-of-merits obtained using a 100 keV threshold energy for Para-Octyl-Dye in poly(vinyl toluene) and wavelength shifted Para-Octyl-Dye in poly(vinyl toluene) scintillator samples as a function of primary dye loading.

delayed emission with decreased singlet-triplet splitting is occurring independent of the type of incident particle, and thus the observed change in delayed emission with changing specific energy loss becomes a smaller relative change. This increase in total delayed emission is further reflected in the PSD histograms, through careful examination of the change in the position of the centroids (with respect to the PSD result, Q_{tail}/Q_{total}, on the ordinate axis) of the the α- and γ-distributions, which show both small but steady increase in Q_{tail}/Q_{total} with increased primary dye loadings, and a much stronger increase in Q_{tail}/Q_{total} going from Meta-Octyl-Dye to Para-Octyl-Dye for identical primary dye loadings. Since Q_{tail}/Q_{total} is a direct measure of the the total fraction of delayed emission observed in the detector during actual PSD measurements, it is an excellent indicator of this particular behavior with regards to both changing singlet-triplet splitting and primary dye loading. It should be further noted that even at the highest loadings of Para-Octyl-Dye for the samples shown in the scintillation decay data in Figures 6.25 and 6.26, the actual rate of photon production in the delayed emission regime is still fairly low compared to the peak of the prompt emission, and thus a smaller relative change in the delayed emission intensity due to changing specific energy

loss would correspondingly be more difficult to measure when the total number of photons generated in a single pulse is ~6000 photons/MeV. As such, despite even the somewhat higher light yield of Para-Octyl-Dye based scintillators as compared to Meta-Octyl-Dye in poly(vinyl toluene), this reduced ability to detect subtle changes in delayed emission is ultimately a direct consequence of the reduced singlet-triplet splitting of Para-Octyl-Dye, and thus these observations imply that in order to achieve good PSD behavior in TADF-based scintillators, one must strike a particular balance in terms of the singlet-triplet splitting, such that excessive conversion of S_1 to T_1 states early in the scintillation process is avoided. On the other hand, while k_{ISC} is inversely related to singlet-triplet splitting, one would presume that other quantum mechanical factors must be operative in determining the exact value of k_{ISC} for a given material, and that with better understanding of these phenomenon, and with judicious design and engineering of the photophysical processes involved, TADF dyes with both low singlet-triplet splitting *and* low k_{ISC} may someday be achievable, which naturally would be prime candidates for PSD-capable TADF scintillators.

6.9   Conclusions

A pair of blue TADF dyes (Meta-Octyl-Dye and Para-Octyl-Dye) were structurally modified from literature TADF dyes (Meta-*t*Butyl-Dye and Para-*t*Butyl-Dye, respectively) for enhanced solubility in aromatic plastics, and the overall photophysical properties and corresponding effects of the structural modifications of all these dyes were extensively characterized. Highest loadings for Meta-Octyl-Dye and Para-Octyl-Dye in poly(vinyl toluene) were found to be 15 wt.% and 9 wt.%, respectively, before total loss of transparency of the bulk samples was observed, although these loadings could be enhanced through crosslinking of the poly(vinyl toluene) plastics. Plastic scintillator samples were fabricated from the Meta-Octyl-Dye and Para-Octyl-Dye TADF dyes, including wavelength shifted variants, and these scintillators were characterized via measurements of their light yields, scintillation decays, and α/γ-PSD performances. From these results, several key observations about the potential and efficacy of TADF dyes as novel organic scintillators were made, including a demonstra-

tion of the profound effects that the TADF dye's singlet-triplet splitting — which controls the degree of T_1 to S_1 conversion in the scintillator — can have on the scintillation properties. In particular, while having a low singlet-triplet splitting was found to be beneficial in terms of achieving maximal scintillation light yield, it can simultaneously degrade the PSD performance of the material in the absence of other balancing factors. Of the specific material systems investigated, wavelength shifted Meta-Octyl-Dye in poly(vinyl toluene) with a primary dye loading of 5 wt.% produced the highest light yield ($\sim$6825 photons/MeV), and was closely followed by unshifted Para-Octyl-Dye in poly(vinyl toluene) with a primary dye loading of 7.5 wt.% ($\sim$6300 photons/MeV). For PSD measurements, unshifted Meta-Octyl-Dye in poly(vinyl toluene) displayed very promising performance, with a peak figure-of-merit of 0.98, and overall its performance was found to be of comparable measure to 2,5-Diphenyloxazole in poly(vinyl toluene) samples, despite the significantly lower photoluminescence quantum yield and longer wavelength emission of the TADF based scintilators. As such, with additional efforts to improve and design dyes to meet the specific requirements for scintillation, TADF dyes could enable a new generation of high performance organic scintilators.

APPENDIX A

Synthetic Procedures

A.1   General Remarks

All starting materials for synthetic procedures were purchased from commercial sources and used as received. Anhydrous THF was obtained via distillation over Na/benzophenone. Anhydrous DCM, DMF, DMSO, and 1,4-dioxane were purchased predried over molecular sieves. ^{1}H and ^{13}C NMR spectra were obtained using either a Bruker DRX500 spectrometer using a 5 mm broadband probe or a Bruker AV500 spectrometer with a 5 mm cryoprobe. Melting points were obtained using a microscope fitted with an Instec HC621V-F8 hot stage and mK1000 temperature controller.

A.2   Synthesis of the DPA-DHS Monomer

The synthetic scheme for the synthesis of the DPA-DHS monomer is shown in fig. A.1. There are five discreet steps in total with a four-step sequence being the longest linear branch with an overall yield of 55%. The synthesis includes as one of its intermediates the dimethoxy-functionalized DMPA, which was additionally utilized as a model compound to investigate the impacts to the photoluminescence properties of DPA-DHS by the introduction of the polymerizable side chains.

A.2.1   Synthesis of 9,10-Bis(4-methoxyphenyl)anthracene-9,10-diol (2)

To a solution of 3.76 mL (30.0 mmol; 2.5 eq.) of 4-bromoanisole (**1**) in 60 mL of dry THF at -78 °C under Ar was dropwise added 12.0 mL (30.0 mmol; 2.5 eq.) of 2.5 M n-butyllithium in
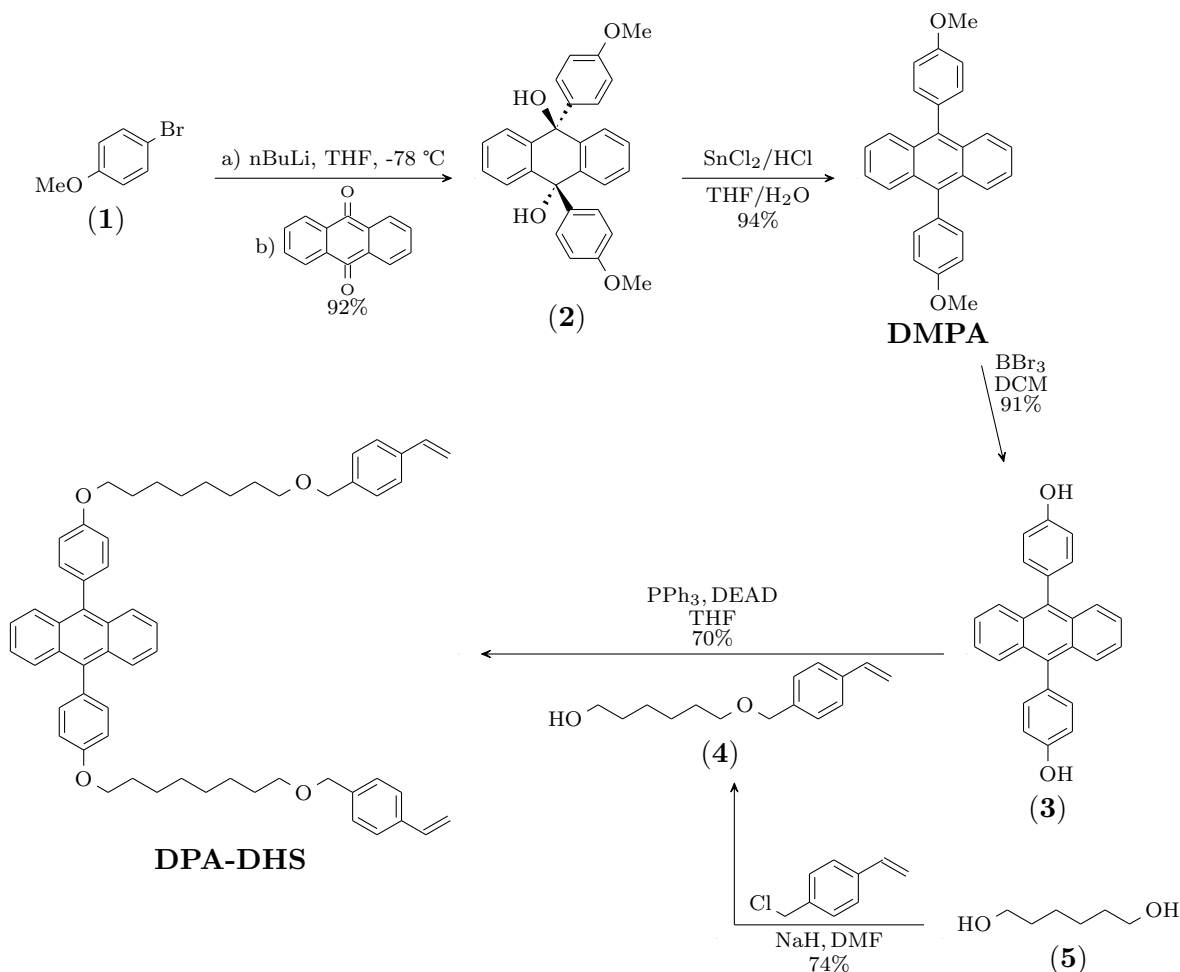
Figure A.1: Synthetic scheme for the synthesis of DPA-DHS.

hexanes. After stirring at -78 ℃ for 1 hour, the solution was transferred dropwise via cannula to a suspension of 2.50 g (12.0 mmol; 1 eq.) of anthraquinone in 50 mL of dry THF at -78 ℃. The resulting solution was warmed to room temperature and stirred for 18.5 hours, then cooled to 0 ℃ and quenched with 20 mL of sat. NH_4Cl. The reaction contents were poured into 250 mL of H_2O, and the resulting mixture was extracted with 3×125 mL of Et_2O. The combined organic layers were washed with 2×250 mL of sat. NaCl and dried over $MgSO_4$. After removal of the solvent under vacuum, the crude product was preadsorbed onto silica gel before flash chromatography with 3:1 Hexane:EtOAc followed by 1:1 Hexane:EtOAc to give 4.69 g (92.0% yield) of (2).

^{1}H-NMR (500 MHz, CDCl3) δ = 7.78-7.73 (m, 4H), 7.40-7.35 (m, 4H), 6.81-6.77 (m, 4H), 6.46-6.42 (m, 4H), 3.64 (s, 6H), 2.97 (s, 2H).

^{13}C-NMR (125 MHz, CDCl$_3$) δ = 158.28, 141.27, 136.83, 128.69, 127.91, 126.71, 112.93, 74.67, 55.20.

A.2.2 Synthesis of 9,10-Bis(4-methoxyphenyl)-anthracene (DMPA)

To a room temperature solution of 2.96 g (6.97 mmol; 1 eq.) of (**2**) in 75 mL of THF that was sparged with Ar for 15 minutes was added a solution of 15.73 g (69.7 mmol; 10 eq.) of SnCl$_2$·2H$_2$O in 60 mL of 10% (wt/v) HCl. The reaction was sparged with Ar for an additional 10 minutes, and after stirring at room temperature for 4.75 hours, the contents were diluted with 75 mL of H$_2$O and filtered. The collected product was washed with H$_2$O and MeOH, dried under vacuum, and recrystallized from CHCl$_3$/cyclohexane to give 2.46 g (90.4% yield) of **DMPA**.

^{1}H-NMR (500 MHz, CDCl$_3$) δ = 7.76-7.71 (m, 4H), 7.42-7.37 (m, 4H), 7.35-7.31 (m, 4H), 7.17-7.12 (m, 4H), 4.00-3.94 (s, 6H).

^{13}C-NMR (125 MHz, CDCl$_3$) δ = 159.15, 136.89, 132.53, 131.29, 130.40, 127.18, 125.03, 114.00, 55.55.

A.2.3 Synthesis of 9,10-Bis(4-hydroxyphenyl)-anthracene (3)

To a suspension of 3.11 g (7.96 mmol; 1 eq.) of **DMPA** in 150 mL of dry DCM at 0 °C under Ar was dropwise added 17.5 mL (17.5 mmol; 2.2 eq.) of 1M BBr$_3$ in DCM. The reaction was slowly warmed to room temperature and stirred for 16 hours, then cooled again to 0 °C before quenching with 30 mL of 10% (wt/v) HCl. The resulting mixture was warmed to room temperature, poured into 150 mL of H$_2$O, and extracted with 3 × 175 mL of EtOAc. The combined organic layers were washed with 300 mL of H$_2$O, 300 mL of sat. NaHCO$_3$, and 300 mL of sat. NaCl, then dried over MgSO$_4$. After removal of the solvent under vacuum, the crude product was preadsorbed onto silica gel before flash chromatography with 2:1 Hexane:EtOAc to give 2.61 g (90.7% yield) of (**3**).

^{1}H-NMR (500 MHz, THF-d_8) δ = 8.51 (s, 2H), 7.75-7.70 (m, 4H), 7.29-7.25 (m, 4H), 7.24-

7.20 (m, 4H), 7.00-6.97 (m, 4H).

^{13}C-NMR (125 MHz, THF-d_8) $\delta = 158.25, 137.89, 133.06, 131.34, 130.46, 127.84, 125.38, 116.08$.

A.2.4   Synthesis of 6-[(4-Ethenylphenyl)methoxy]-1-hexanol (4)

To a suspension of 2.00 g (50.0 mmol; 1 eq.) of 60% NaH in 100 mL of dry DMF at 0 ℃ under Ar was carefully added 17.73 g (150.0 mmol; 3 eq.) of 1,6-hexanediol (5) against a counterflow of Ar. The mixture was warmed to room temperature and stirred for 1 hour, then cooled to 0 ℃ before dropwise adding 7.75 mL (55.0 mmol; 1.1 eq.) of 4-vinylbenzyl chloride. The reaction was warmed to room temperature and stirred for 17.5 hours, then poured into 500 mL of H_2O and extracted with 3×200 mL of Et_2O. The combined organic layers were washed with 2×400 mL of H_2O and 400 mL of sat. NaCl, then dried over $MgSO_4$. After removal of the solvent under vacuum, the crude product was purified via flash chromatography on silica gel with 3:1 Hexane:EtOAc to give 8.72 g (74.4% yield) of (4).

^{1}H-NMR (500 MHz, CDCl$_3$) $\delta = 7.39$ (d, $J = 8.0$ Hz, 2H), 7.29 (d, $J = 8.0$ Hz, 2H), 6.71 (dd, $J = 17.6, 10.9$ Hz, 1H), 5.74 (dd, $J = 17.6, 0.9$ Hz, 1H), 5.23 (dd, $J = 10.9, 0.9$ Hz, 1H), 4.48 (s, 2H), 3.60 (t, $J = 6.6$ Hz, 2H), 3.46 (t, $J = 6.6$ Hz, 2H), 1.82 (s, 1H), 1.62 (quin, $J = 6.9$ Hz, 2H), 1.56 (t, $J = 6.9$ Hz, 2H), 1.43-1.32 (m, 4H).

^{13}C-NMR (125 MHz, CDCl$_3$) $\delta = 138.29, 136.95, 136.64, 127.92, 126.28, 113.77, 72.66, 70.37, 62.86, 32.74, 29.77, 26.07, 25.66$.

A.2.5   Synthesis of 9,10-Bis[4-({6-[(4-ethenylphenyl)methoxy]hexyl}oxy)phen-
yl]anthracene (DPA-DHS)

To a solution of 1.33 g (3.67 mmol; 1 eq.) of (3), 2.58 g (11.0 mmol; 3 eq.) of (4), and 1.73 mL (11.0 mmol; 3 eq.) of diethylazodicarboxylate in 70 mL of dry THF at 0 ℃ under Ar was dropwise added a solution of 2.89 g (11.0 mmol; 3 eq.) of triphenylphosphine in 25 mL of dry THF with the formation of a precipitate. The reaction was warmed to room temperature and

stirred for 24 hours, after which all of the precipitate had redissolved. The reaction solvent was removed under vacuum, and the crude mixture was purified via flash chromatography on silica gel with 1:3 Hexane:DCM to give 2.39 g (81.9% yield) of **DPA-DHS** as a pale yellow solid (m.p. 119-123 ℃).

^{1}H-NMR (500 MHz, CDCl$_3$) δ = 7.78-7.73 (m, 4H), 7.42-7.40 (m, 4H), 7.39-7.36 (m, 4H), 7.36-7.31 (m, 8H), 7.15-7.11 (m, 4H), 6.72 (dd, $J = 17.6, 10.9$ Hz, 2H), 5.75 (dd, $J = 17.6, 0.9$ Hz, 2H), 5.23 (dd, $J = 10.9, 0.9$ Hz, 2H), 4.52 (s, 4H), 4.11 (t, $J = 6.5$ Hz, 4H), 3.52 (t, $J = 6.5$ Hz, 4H), 1.91 (quin, $J = 6.9$ Hz, 4H), 1.72 (quin, $J = 6.9$ Hz, 4H), 1.63-1.49 (m, 8H).

^{13}C-NMR (125 MHz, CDCl$_3$) δ = 158.45, 138.20, 136.80, 136.70, 136.48, 132.26, 130.85, 130.17, 127.76, 126.96, 126.14, 124.74, 114.28, 113.61, 72.55, 70.21, 67.88, 29.67, 29.28, 25.99, 25.95.

A.3 Synthesis of the TADF Dyes
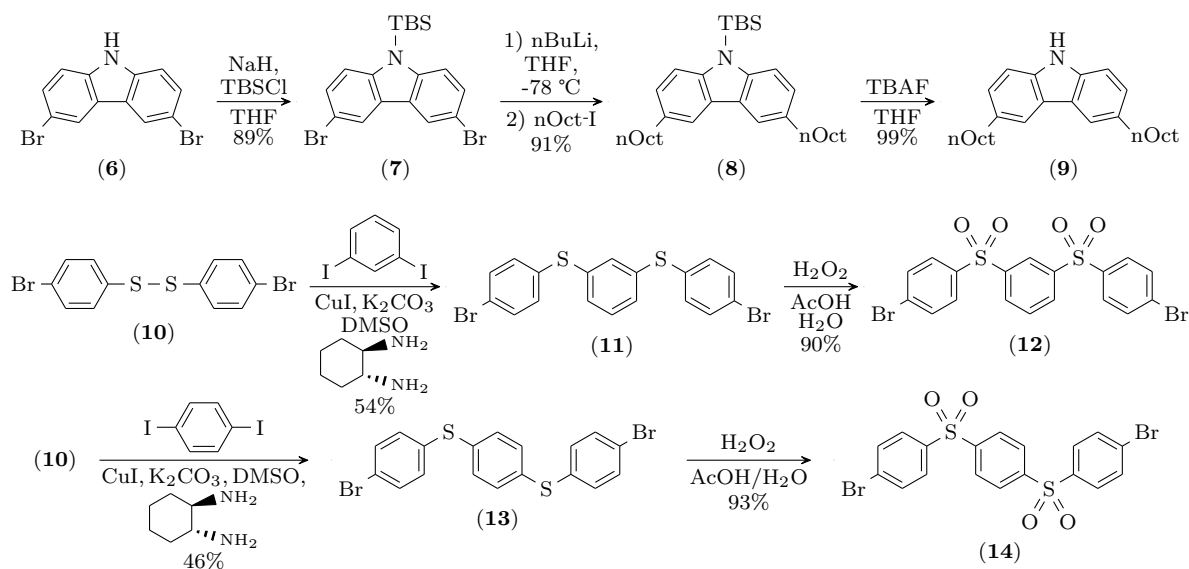
Figure A.2: Synthetic scheme for the synthesis of TADF dye precursors.
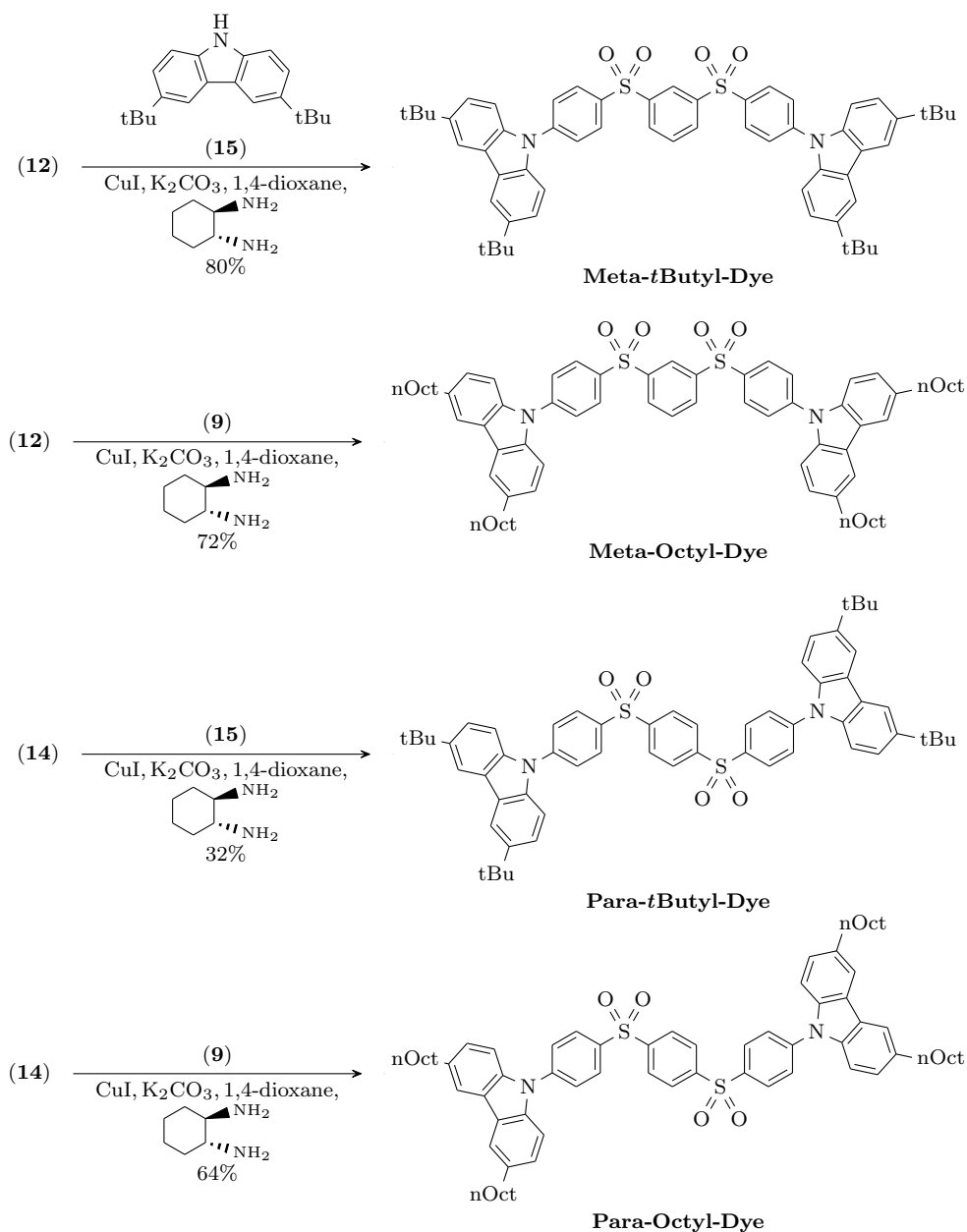
Figure A.3: Synthetic scheme for the synthesis of TADF dyes.

A.3.1 Synthesis of 3,6-Dibromo-9-(*tert*-butyldimethylsilyl)-9H-carbazole (7)

To a suspension of 0.738 g (18.5 mmol; 1.2 eq.) of 60% NaH in 100 mL of dry THF at 0 °C under argon was dropwise added a solution of 5.00 g (15.4 mmol; 1.0 eq.) of 3,6-dibromocarbazole (6) in 15 mL of dry THF, after which the resulting mixture was warmed to room temperature and stirred for 30 minutes before 2.55 g (16.9 mmol; 1.1 eq.) of TBSCl were carefully added against a counterflow of Ar. The reaction was stirred for an additional

1 hour before carefully quenching with 5 mL of H_2O, and the resulting mixture was poured into an additional 250 mL of H_2O and extracted with 3×175 mL of Et_2O. The combined organic layers were washed with 250 mL of sat. NaCl and dried over $MgSO_4$ before removal of the solvent under vacuum. The crude product was preadsorbed onto silica gel before flash chromatography with 20:1 Hexane:DCM to give 5.98 g (88.5% yield) of (**7**) as a colorless solid.

^{1}H-NMR (500 MHz, $CDCl_3$) $\delta = 8.11$ (s, 2H), 7.46 (s, 2H), 7.46 (s, 2H), 1.01 (s, 9H), 0.74 (s, 6H).

^{13}C-NMR (125 MHz, $CDCl_3$) $\delta = 143.95, 128.55, 127.00, 122.62, 115.43, 112/76, 26.34, 20.42, -1.42$.

A.3.2 Synthesis of 9-(*tert*-Butyldimethylsilyl)-3,6-dioctyl-9H-carbazole (8)

To a mixture of 5.00 g (11.4 mmol; 1.0 eq.) of (**7**) in 150 mL of dry THF at -78 ℃ under Ar was dropwise added 10.0 mL (25.0 mmol; 2.2 eq.) of 2.5M n-BuLi in Hexane, and the resulting mixture was stirred at -78 ℃ for 1 hour before dropwise adding 4.52 mL (25.0 mmol; 2.2 eq.) of 1-iodooctane. The reaction was allowed to slowly warm to room temperature and stirred over night, then quenched with 10 mL of sat. NH_4Cl. The resulting mixture was poured into 300 mL of H_2O, and extracted with 3×200 mL of Et_2O. The combined organic layers were washed with 300 mL of sat. $Na_2S_2O_3$ and 300 mL of sat. NaCl, then dried over $MgSO_4$. After removal of the solvent under vacuum, the crude product was purified via flash chromatography with Hexane to give 5.22 g (90.6% yield) of (**8**) as a colorless oil.

^{1}H-NMR (500 MHz, $CDCl_3$) $\delta = 7.86$ (s, 2H), 7.50 (d, $J = 8.51$ Hz, 2H), 7.18 (d, $J = 8.51$ Hz, 2H), 2.78 (t, $J = 7.78$ Hz, 4H, 1.74 (quint, $J = 7.39$ Hz, 4H), 1.42-1.31 (m, 20H), 1.07 (s, 9H), 0.92 (t, $J = 6.70$ Hz, 6H), 0.75 (s, 6H).

^{13}C-NMR (125 MHz, $CDCl_3$) $\delta = 143.55, 133.79, 126.23, 125.69, 118.91, 113.55, 35.75, 32.12, 31.86, 29.50, 29.37, 29.24, 26.53, 22.62, 20.50, 14.05, -1.47$.

A.3.3 Synthesis of 3,6-Dioctyl-9H-carbazole (9)

To a solution of 5.24 g (10.4 mmol; 1.0 eq.) of (**8**) in 100 mL of THF was added 12.4 mL (12.4 mmol; 1.2 eq.) of 1.0M TBAF in THF, and the reaction was stirred at room temperature for 1 hour. The reaction contents were concentrated under vacuum, and the remaining residue was dissolved in 250 mL of Et_2O before washing with 2×250 mL of H_2O and 250 mL of sat. NaCl, then dried over $MgSO_4$. After removal of the solvent under vacuum, the crude product was purified via flash chromatography with 3:1 Hexane:DCM to give 4.01 g (98.9% yield) of (**9**) as a foamy white solid.

^{1}H-NMR (500 MHz, CDCl$_3$) δ = 7.86 (s, 2H), 7.30 (d, J = 8.21 Hz, 2H), 7.22 (d, J = 8.21 Hz, 2H), 2.77 (t, J = 7.78 Hz, 4H), 1.71 (quint, J = 7.40 Hz, 4H), 1.39-1.28 (m, 20H), 0.89 (t, J = 6.65 Hz, 6H).

^{13}C-NMR (125 MHz, CDCl$_3$) δ = 138.12, 133.73, 126.30, 123.30, 119.42, 110.47, 35.96, 32.26, 31.82, 29.47, 29.29, 29.21, 22.59, 14.02.

A.3.4 Synthesis of 1,3-Bis[(4-bromophenyl)sulfanyl]benzene (11)

A mixture of 5.00 g (13.3 mmol; 1.1 eq.) of 4-bromophenyl disulfide (**10**), 3.99 g (12.1 mmol; 1.0 eq.) of 1,3-diiodobenzene, 0.230 g (1.21 mmol; 0.1 eq.) of CuI, 4.18 g (30.2 mmol; 2.5 eq.) of K_2CO_3, and 0.58 mL (4.8 mmol; 0.4 eq.) of (±)-*trans*-1,2-diaminocyclohexane in 75 mL of dry DMSO under Ar was heated at 120 ℃ for 4 hours, then cooled to room temperature and poured into 375 mL of H_2O. The resulting mixture was extracted with 3×225 mL of Et_2O, and the combined organic layers were washed with 300 mL of sat. $Na_2S_2O_3$, 2×300 mL of H_2O, and 300 mL of sat. NaCl, then dried over $MgSO_4$. After removal of the solvent under vacuum, the crude product was preadsorbed onto silica gel before flash chromatography with Hexane to give 2.95 g (54.0% yield) of (**11**) as a white solid.

^{1}H-NMR (500 MHz, CDCl$_3$) δ = 7.43 (d, J = 8.56 Hz, 4H), 7.24-7.21 (m, 1H), 7.19 (d, J = 8.56 Hz, 4H), 7.16-7.14 (m, 3H).

^{13}C-NMR (125 MHz, CDCl$_3$) δ = 137.39, 133.92, 133.42, 132.58, 131.66, 130.03, 128.93, 121.96.

A.3.5 Synthesis of 1,3-Bis(4-bromobenzenesulfonyl)benzene (12)

To a solution of 2.92 g (6.46 mmol; 1.0 eq.) of (11) in 75 mL of acetic acid at 100 ℃ was dropwise added 6.49 mL (63.0 mmol; 9.75 eq.) of 30% H$_2$O$_2$, and after stirring at 100 ℃ for an additional 1 hour, the reaction was cooled to room temperature and poured into 525 mL of H$_2$O. The resulting precipitate was filtered and washed with copious H$_2$O, then dried under vacuum to give 3.01 g (90.3% yield) of (12) which was used without further purification.

^{1}H-NMR (500 MHz, CDCl$_3$) δ = 8.48 (t, J = 1.78 Hz, 1H), 8.09 (dd, J = 7.91, 1.80 Hz, 2H), 7.80 (d, J = 8.71 Hz, 4H), 7.70-7.66 (m, 5H).

^{13}C-NMR (125 MHz, CDCl$_3$) δ = 143.41, 139.42, 133.16, 132.31, 131.02, 6, 126.89.

A.3.6 Synthesis of 1,4-Bis[(4-bromophenyl)sulfanyl]benzene (13)

A mixture of 3.00 g (7.98 mmol; 1.1 eq.) of 4-bromophenyl disulfide (10), 2.39 g (7.25 mmol; 1.0 eq.) of 1,4-diiodobenzene, 0.138 g (0.725 mmol; 0.1 eq.) of CuI, 2.51 g (18.1 mmol; 2.5 eq.) of K$_2$CO$_3$, and 0.35 mL (2.9 mmol; 0.4 eq.) of ($\pm$)-*trans*-1,2-diaminocyclohexane in 45 mL of dry DMSO under Ar was heated at 120 ℃ for 4 hours, then cooled to room temperature and poured into 225 mL of H$_2$O. The resulting mixture was extracted with 3 × 135 mL of Et$_2$O, and the combined organic layers were washed with 180 mL of sat. Na$_2$S$_2$O$_3$, 2 × 180 mL of H$_2$O, and 180 mL of sat. NaCl, then dried over MgSO$_4$. After removal of the solvent under vacuum, the crude product was preadsorbed onto silica gel before flash chromatography with Hexane to give 2.95 g (54.0% yield) of (11). After removal of the solvent under vacuum, the crude product was preadsorbed onto silica gel before flash chromatography with 1:0 then 10:1 Hexane:DCM to give 1.65 g (45.7% yield) of (13) as a white solid.

^{1}H-NMR (500 MHz, CDCl$_3$) δ = 7.43 (dt, J = 9.21, 2.25 Hz, 4H), 7.23 (s, 4H), 7.21 (dt, J = 9.26, 2.28 Hz, 4H).

^{13}C-NMR (125 MHz, CDCl$_3$) δ = 134.56, 134.23, 132.69, 132.31, 131.36, 121.43.

A.3.7   Synthesis of 1,4-Bis(4-bromobenzenesulfonyl)benzene (14)

To a suspension of 1.64 g (3.63 mmol; 1.0 eq.) of (**13**) in 75 mL of acetic acid at 100 ℃ was dropwise added 3.64 mL (35.4 mmol; 9.75 eq.) of 30% H$_2$O$_2$, and after stirring at 100 ℃ for an additional 1 hour, the reaction was cooled to room temperature before dropwise adding 75 mL of H$_2$O. The resulting mixture was poured into 450 mL of H$_2$O, and the precipitate was filtered and washed with copious H$_2$O, then dried under vacuum to give 1.74 g (93.0% yield) of (**14**) which was used without further purification.

^{1}H-NMR (500 MHz, CDCl$_3$) δ = 8.04 (s, 4H), 7.78 (dt, J = 9.10, 2.15 Hz, 4H), 7.67 (dt, J = 9.05, 2.18 Hz, 4H).

^{13}C-NMR (125 MHz, CDCl$_3$) δ = 146.07, 139.31, 133.13, 129.63, 128.85, 125.41.

A.3.8   Synthesis of 3,6-di-tert-butyl-9-(4-3-[4-(3,6-di-tert-butyl-9H-carbazol-9-yl)-benzenesulfonyl]benzenesulfonylphenyl)-9H-carbazole (Meta-*t*Butyl-Dye)

A mixture of 0.50 g (0.969 mmol; 1.0 eq.) of (**12**), 0.60 g (2.13 mmol; 2.2 eq.) of 3,6-di-*tert*-butylcarbazole (**15**), 0.90 g (4.26 mmol; 2.2 eq.) of K$_3$PO$_4$, 18.4 mg (96.9 µmol; 0.1 eq.) of CuI, and 0.05 mL (0.387 mmol; 0.4 eq.) of (±)-*trans*-1,2-diaminocyclohexane in 15 mL of dry 1,4-dioxane under Ar was heated at reflux for 24 hours, then cooled to room temperature and poured into 50 mL of H$_2$O and 50 mL of Et$_2$O. The resulting mixture was extracted with 3 × 50 mL of DCM, and the combined organic layers were washed with 100 mL of H$_2$O and 100 mL of sat. NaCl, then dried over MgSO$_4$. After removal of the solvent under vacuum, the crude product was purified via flash chromatography with DCM to give 0.71 g (80.3% yield) of Meta-*t*Butyl-Dye as a faintly yellow solid.

^{1}H-NMR (500 MHz, CDCl$_3$) δ = 8.71 (s, 1H), 8.26 (dt, J = 7.93, 0.81 Hz, 2H), 8.19 (d, J = 8.56 Hz, 4H), 8.12 (s, 4H), 7.82-7.78 (m, 5H), 7.46 (dd, J = 8.66, 1.20 Hz, 4H), 7.42 (d, J = 8.61 Hz, 4H), 1.45 (s, 36H).

¹³C-NMR (125 MHz, CDCl₃) δ = 144.13, 143.72, 143.48, 138.02, 137.23, 132.16, 130.83, 129.74, 126.87, 126.53, 124.07, 123.93, 116.42, 109.04, 34.67, 31.80.

A.3.9 Synthesis of 9-(4-3-[4-(3,6-dioctyl-9H-carbazol-9-yl)benzenesulfonyl]benzenesulfonylphenyl)-3,6-dioctyl-9H-carbazole (Meta-Octyl-Dye)

A mixture of 2.00 g (3.87 mmol; 1.0 eq.) of (**12**), 3.34 g (8.52 mmol; 2.2 eq.) of (**9**), 3.62 g (17.1 mmol; 4.4 eq.) of K₃PO₄, 73.8 mg (0.387 mmol; 0.1 eq.) of CuI, and 0.19 mL (1.6 mmol; 0.4 eq.) of (±)-*trans*-1,2-diaminocyclohexane in 60 mL of dry 1,4-dioxane under Ar was heated at reflux for 24 hours, then cooled to room temperature and poured into 200 mL of H₂O. The resulting mixture was extracted with 3 × 150 mL of Et₂O, and the combined organic layers were washed with 2 × 200 mL of H₂O and 200 mL of sat. NaCl, then dried over MgSO₄. After removal of the solvent under vacuum, the crude product was purified via flash chromatography with 1:4 Hexane:DCM to give 3.17 g (71.8% yield) of Meta-Octyl-Dye as a foamy pale yellow solid.

¹H-NMR (500 MHz, CDCl₃) δ = 8.70 (t, J = 1.68 Hz, 1H), 8.26 (dd, J = 7.90, 1.80 Hz, 2H), 8.18 (dt, J = 9.15, 2.15 Hz, 4H), 7.89 (d, J = 1.10 Hz, 4H), 7.81-7.78 (m, 5H), 7.38 (d, J = 8.35 Hz, 4H), 7.20 (dd, J = 8.43, 1.63 Hz, 4H), 2.77 (t, J = 7.68 Hz, 8H), 1.70 (quint, J = 7.45 Hz, 8H), 1.42-1.24 (m, 40H), 0.89 (t, J = 6.95 Hz, 12H).

¹³C-NMR (125 MHz, CDCl₃) δ = 143.93, 143.72, 138.49, 137.52, 135.96, 132.39, 131.07, 129.96, 127.16, 127.06, 126.90, 124.38, 119.94, 109.43, 36.09, 32.37, 32.05, 29.69, 29.50, 29.45, 22.82, 14.26.

A.3.10 Synthesis of 3,6-Di-*tert*-butyl-9-(4-4-[4-(3,6-di-*tert*-butyl-9H-carbazol-9-yl)benzenesulfonyl]benzenesulfonylphenyl)-9H-carbazole (Para-*t*Butyl-Dye)

A mixture of 0.500 g (0.969 mmol; 1.0 eq.) of (**14**), 0.595 g (2.13 mmol; 2.2 eq.) of 3,6-di-*tert*-butylcarbazole (**15**), 0.905 g (4.26 mmol; 2.2 eq.) of K₃PO₄, 18.4 mg (96.9 µmol;

^{13}C-NMR (125 MHz, CDCl$_3$) δ = 144.13, 143.72, 143.48, 138.02, 137.23, 132.16, 130.83, 129.74, 126.87, 126.53, 124.07, 123.93, 116.42, 109.04, 34.67, 31.80.

A.3.9 Synthesis of 9-(4-3-[4-(3,6-dioctyl-9H-carbazol-9-yl)benzenesulfonyl]benzenesulfonylphenyl)-3,6-dioctyl-9H-carbazole (Meta-Octyl-Dye)

A mixture of 2.00 g (3.87 mmol; 1.0 eq.) of (**12**), 3.34 g (8.52 mmol; 2.2 eq.) of (**9**), 3.62 g (17.1 mmol; 4.4 eq.) of K$_3$PO$_4$, 73.8 mg (0.387 mmol; 0.1 eq.) of CuI, and 0.19 mL (1.6 mmol; 0.4 eq.) of (±)-*trans*-1,2-diaminocyclohexane in 60 mL of dry 1,4-dioxane under Ar was heated at reflux for 24 hours, then cooled to room temperature and poured into 200 mL of H$_2$O. The resulting mixture was extracted with 3 × 150 mL of Et$_2$O, and the combined organic layers were washed with 2 × 200 mL of H$_2$O and 200 mL of sat. NaCl, then dried over MgSO$_4$. After removal of the solvent under vacuum, the crude product was purified via flash chromatography with 1:4 Hexane:DCM to give 3.17 g (71.8% yield) of Meta-Octyl-Dye as a foamy pale yellow solid.

^{1}H-NMR (500 MHz, CDCl$_3$) δ = 8.70 (t, J = 1.68 Hz, 1H), 8.26 (dd, J = 7.90, 1.80 Hz, 2H), 8.18 (dt, J = 9.15, 2.15 Hz, 4H), 7.89 (d, J = 1.10 Hz, 4H), 7.81-7.78 (m, 5H), 7.38 (d, J = 8.35 Hz, 4H), 7.20 (dd, J = 8.43, 1.63 Hz, 4H), 2.77 (t, J = 7.68 Hz, 8H), 1.70 (quint, J = 7.45 Hz, 8H), 1.42-1.24 (m, 40H), 0.89 (t, J = 6.95 Hz, 12H).

^{13}C-NMR (125 MHz, CDCl$_3$) δ = 143.93, 143.72, 138.49, 137.52, 135.96, 132.39, 131.07, 129.96, 127.16, 127.06, 126.90, 124.38, 119.94, 109.43, 36.09, 32.37, 32.05, 29.69, 29.50, 29.45, 22.82, 14.26.

A.3.10 Synthesis of 3,6-Di-*tert*-butyl-9-(4-4-[4-(3,6-di-*tert*-butyl-9H-carbazol-9-yl)benzenesulfonyl]benzenesulfonylphenyl)-9H-carbazole (Para-*t*Butyl-Dye)

A mixture of 0.500 g (0.969 mmol; 1.0 eq.) of (**14**), 0.595 g (2.13 mmol; 2.2 eq.) of 3,6-di-*tert*-butylcarbazole (**15**), 0.905 g (4.26 mmol; 2.2 eq.) of K$_3$PO$_4$, 18.4 mg (96.9 µmol;

0.1 eq.) of CuI, and 0.05 mL (0.387 mmol; 0.4 eq.) of ($\pm$)-*trans*-1,2-diaminocyclohexane in 15 mL of dry 1,4-dioxane under Ar was heated at reflux for 24 hours, then cooled to room temperature and poured into 50 mL of H_2O. The resulting mixture was extracted with 3×60 mL of DCM, and the combined organic layers were washed with 125 mL of H_2O and 125 mL of sat. NaCl, then dried over $MgSO_4$. After removal of the solvent under vacuum, the crude product was purified via flash chromatography with 1:4 Hexane:DCM to give 0.283 g (32.0% yield) of Para-*t*Butyl-Dye as a faintly yellow solid.

^{1}H-NMR (500 MHz, CDCl$_3$) δ = 8.21 (s, 4H), 8.16 (dt, J = 9.15, 2.18 Hz, 4H), 8.11 (d, J = 1.45 Hz, 4H), 7.79 (dt, J = 9.18, 2.19 Hz, 4H), 7.46 (dd, J = 8.70, 1.95 Hz, 4H), 7.40 (dd, J = 8.70, 0.45 Hz, 4H), 1.45 (s, 36H).

^{13}C-NMR (125 MHz, CDCl$_3$) δ = 146.33, 144.44, 144.01, 138.24, 137.31, 130.06, 129.01, 126.72, 124.33, 124.19, 116.70, 109.26, 34.93, 32.05.

A.3.11   Synthesis of 9-(4-4-[4-(3,6-Dioctyl-9H-carbazol-9-yl)benzenesulfonyl]benzenesulfonylphenyl)-3,6-dioctyl-9H-carbazole (Para-Octyl-Dye)

A mixture of 0.500 g (0.969 mmol; 1.0 eq.) of (**14**), 0.835 g (2.13 mmol; 2.2 eq.) of (**9**), 0.905 g (17.1 mmol; 4.4 eq.) of K_3PO_4, 18.4 mg (96.9 µmol; 0.1 eq.) of CuI, and 0.05 mL (0.39 mmol; 0.4 eq.) of ($\pm$)-*trans*-1,2-diaminocyclohexane in 15 mL of dry 1,4-dioxane under Ar was heated at reflux for 24 hours, then cooled to room temperature and poured into 50 mL of H_2O. The resulting mixture was extracted with 3×35 mL of Et_2O, and the combined organic layers were washed with 2×50 mL of H_2O and 50 mL of sat. NaCl, then dried over $MgSO_4$. After removal of the solvent under vacuum, the crude product was purified via flash chromatography with 1:3 Hexane:DCM to give 0.71 g (64.4% yield) of Para-Octyl-Dye as a foamy light yellow solid.

^{1}H-NMR (500 MHz, CDCl$_3$) δ = 8.21 (s, 4H), 8.16 (d, J = 8.66 Hz, 4H), 7.90 (s, 4H), 7.79 (d, J = 8.61 Hz, 4H), 7.37 (d, J = 8.36 Hz, 4H), 7.21 (dd, J = 8.43, 1.53 Hz, 4H), 2.78 (t, J = 7.68 Hz, 8H), 1.70 (quint, J = 7.39 Hz, 8H), 1.42-1.28 (m, 40H), 0.88 (t, J = 7.00 Hz,

12H).

^{13}C-NMR (125 MHz, CDCl$_3$) δ = 146.33, 143.98, 138.49, 137.38, 136.01, 130.03, 129.00, 127.07, 126.86, 124.40, 119.98, 109.41, 36.09, 32.37, 32.05, 29.68, 29.49, 29.44, 22.82, 14.25.

APPENDIX B

Characterization Methods

B.1   Scintillator Sample Fabrication

Coumarin 6 (Sigma-Aldrich), 1,4-bis[4-(di-p-tolylamino)styryl]benzene (DPAVB; TCI America) and 1,1-di-(tert-butylperoxy)-3,3,5-trimethylcyclohexane (initiator; Acros) were used as received. Methystyrene (60% meta, 40% para, & 1% ortho mixture of isomers; Sigma-Aldrich) and divinylbenzene (DVB, technical grade, 80%, Sigma-Aldrich) were degassed via freeze-pump-thaw and passed through a short column of inhibitor remover under N_2 (Sigma-Aldrich) prior to use. Glass shell vials with internal diameters of 10 mm were cleaned in piranha solution immediately before vapor treatment under house vacuum with (tridecafluoro-1,1,2,2-tetrahydrooctyl)trichlorosilane (Gelest). All samples were prepared by mixing each component along with 0.5 wt.% of initiator and heating at 80 ℃ for 24 hours under N_2. After cooling to room temperature, the vials were broken to remove the cured samples, which were further ground and polished to the desired thickness. Thin film samples were prepared by dropcasting at 120 ℃ chlorobenzene solutions of the respective dye components and poly(vinyl toluene) (mixed isomers, 60% meta, 40% para, M_w ∼80,000; Scientific Polymer Products) onto glass coverslips.

B.2   Scintillator Characterization

Absorbance spectra were acquired using a Shimadzu UV-1700 UV-Visible Spectrophotometer and were referenced against a solvent blank. Solution spectra were referenced against a solvent blank, while spectra acquired for plastic films and bulk scintillator samples were

referenced against the glass substrate and air, respectively. Photoluminescence spectra under right-angle geometry were acquired using a QuantaMaster QM-4/SE (Photon Technology Inc.) fluorometer. Emission spectra for solutions and thin-films were acquired in the standard right-angle spectrometer geometry, using 10mm quartz cells and an adjustable angle thin-film sample holder, respectively, while spectra for plastic samples (Chapter 5) were acquired using a right angle geometry specially offset to avoid collection of light emitted directly from the sample surface, in order to best represent the technical emission spectrum of the scintillator samples as viewed by a PMT during actual detection tests. Photoluminescence quantum yields (Φ_{PL}) of solutions were measured in right-angle geometry via the absorbance and fluorescence spectra of a series of concentrations for degassed (freeze-pump-thaw) samples using DPA in cyclohexane ($\Phi_{PL} = 1$)[55] as the reference standard, and the concentration of all solutions were kept sufficiently low as to achieve absorbances no greater than 0.1 AU over the range of concentrations. Photoluminescence spectra of plastic samples under transmission-mode geometry (Chapter 6) were acquired using a Thorlabs M365FP1 Fiber-Coupled LED (365 nm) as an excitation source, and a Ocean-Optics USB2000 Fiber Optic Spectrometer for recording the emission spectra, both of which were coupled to a pair of Ocean-Optics 74-UV Collimating Lenses via Thorlabs M112L02 Fiber Optic Patch Cables (200 µm).

Gamma-ray spectra under ^{137}Cs irradiation were recorded using a Canberra Lynx Digital Signal Processor; a custom machined PTFE sample holder was used to ensure placement accuracy and optical grease was used to couple the sample to the window of a Hamamatsu R878 PMT, which itself was plugged into a Canberra Model 2007P Photomultiplier Tube Base/Preamplifier. All spectra were recorded using a trapezoidal shaping filter with a 1.0 µs rise time and a 0.5 µs flat-top time. The relative Compton edge positions were compared to identically sized specimens of EJ-212 (Eljen Technology, Inc.) that were machined and polished from larger pieces of sheet stock. The acquired photoluminescence data was used along with the quantum efficiency curve for the PMT photocathode to correct the relative Compton edge positions for the emission spectrum of each sample. In this manner, absolute light yields were obtained from the manufacturer's specification for the light yield of EJ-212 (10,000 photons/MeV).

Time resolved radioluminescence decay curves were measured using a time-correlated single photon counting (TCSPC) based approach utilizing a Hamamatsu H2431-50 assembly as the start PMT and a Hamamatsu H10721P-110 module fitted with an E5776-51 SMA fiber optic adapter as the stop PMT. A bare terminated 800 µm multi-mode fiber was used along with a custom machined PTFE sample holder to allow the stop PMT to collect single photons from the sample; under ^{137}Cs irradiation, the sample was directly coupled using optical grease to the window of the start PMT, but under [210]Po irradiation, the PTFE sample holder and source were placed inside a specially constructed vacuum chamber with a quartz disk end-window, onto which the start PMT was coupled. The signal from the stop PMT was fed into a Ortec Model 9326 Fast Preamplifier, and the resulting output along with the signal from the start PMT was digitized using a PicoScope Model 5244B Oscilloscope (Pico Technology, Inc.) operated in 8-bit mode with a digitization rate of 500 MS/sec. The differences in arrival times between single photon pulses detected by the stop PMT and the main pulse detected by the start PMT were histogrammed to obtain the scintillation decay curves over the measurement interval.

Pulse-shape discrimination tests were performed under simultaneous α/γ irradiation, which was done in lieu of the more commonplace n/γ PSD testing on account of the fact that NRC exempt quantities of both γ and α (specifically [210]Po) emitters are readily available, inexpensive, and can be purchased and handled without special precautions or license (no such NRC exempt quantity is currently available for neutron emitting sources). Pulses from samples under irradiation were acquired using a Hamamatsu R6321-100 PMT that was coupled to the quartz disk end-window of a specially constructed vacuum chamber. The sample under test was coupled to the vacuum side of the end-window using optical grease, and was held in place using a custom machined PTFE sample holder, which also held in place the mixed source assembled from separate [210]Po and ^{137}Cs sources. Raw pulses obtained from the PMT anode were digitized using the Picoscope Model 5244B Oscilloscope operated in 12-bit mode with a digitization rate of 500 MS/sec and were saved directly to disk for off-line analysis. Energy calibration of the resulting data sets was performed by histogramming the total integral of each pulse and finding the position of the Compton edge of the gamma

distribution. Two-dimensional plots representing the PSD performance were obtained using a digital charge comparison method to give a plot of (Q_{tail}/Q_{total}) versus equivalent particle energy (keV-ee). [13–15,17,18]

Bibliography

[1] G. F. Knoll, Radiation Detection and Measurement, 4th Edition, John Wiley & Sons, Hoboken, NJ, USA, 2010.

[2] J. B. Birks, The Theory and Practice of Scintillation Counting, International series of monographs on electronics and instrumentation, v. 27, Pergamon Press, London, U.K., 1964.

[3] A. Pla-Dalmau, A. D. Bross, K. L. Mellott, Low-cost extruded plastic scintillator, Nuclear Instruments and Methods in Physics Research Section A: Accelerators, Spectrometers, Detectors and Associated Equipment 466 (3) (2001) 482–491.

[4] F. D. Brooks, Development of organic scintillators, Nuclear Instruments and Methods 162 (1) (1979) 477–505.

[5] G. Laustriat, The luminescence decay of organic scintillators, Molecular Crystals 4 (1-4) (1968) 127–145.

[6] R. Voltz, J. L. Da Silva, G. Laustriat, A. Coche, Influence of the nature of ionizing particles on the specific luminescence of organic scintillators, The Journal of Chemical Physics 45 (9) (1966) 3306–3311.

[7] J. B. Birks, The scintillation process in organic systems, IRE Transactions on Nuclear Science 7 (2-3) (1960) 2–11.

[8] N. J. Turro, V. Ramamurthy, J. C. Scaiano, Principles of Molecular Photochemistry: An Introduction, University Science Books, Sausalito, CA, USA, 2009.

[9] P. S. Lee, C. S. Lee, J. H. Lee, Development of fpga-based digital signal processing system for radiation spectroscopy, Radiation Measurements 48 (2013) 12–17.

[10] M. L. Roush, M. A. Wilson, W. F. Hornyak, Pulse shape discrimination, Nuclear Instruments and Methods 31 (1) (1964) 112–124.

[11] F. T. Kuchnir, F. J. Lynch, Time dependence of scintillations and the effect on pulse-shape discrimination, IEEE Transactions on Nuclear Science 15 (3) (1968) 107–113.

[12] Z. W. Bell, Tests on a digital neutron-gamma pulse shape discriminator with ne213, Nuclear Instruments and Methods in Physics Research 188 (1) (1981) 105–109.

[13] N. V. Kornilov, V. A. Khriatchkov, M. Dunaev, A. B. Kagalenko, N. N. Semenova, V. G. Demenkov, A. J. M. Plompen, Neutron spectroscopy with fast waveform digitizer, Nuclear Instruments and Methods in Physics Research Section A: Accelerators, Spectrometers, Detectors and Associated Equipment 497 (2) (2003) 467–478.

[14] P. J. Sellin, G. Jaffar, S. D. Jastaniah, Performance of digital algorithms for n/γ pulse shape discrimination using a liquid scintillation detector, in: Nuclear Science Symposium Conference Record, 2003 IEEE, Vol. 2, IEEE, Piscataway, NJ, USA, 2003, pp. 1057–1060.

[15] R. Aryaeinejad, J. K. Hartwell, D. F. Spencer, Comparison between digital and analog pulse shape discrimination techniques for neutron and gamma ray separation, in: Nuclear Science Symposium Conference Record, 2005 IEEE, Vol. 1, IEEE, Piscataway, NJ, USA, 2005, pp. 500–504.

[16] K. A. A. Gamage, M. J. Joyce, N. P. Hawkes, A comparison of four different digital algorithms for pulse-shape discrimination in fast scintillators, Nuclear Instruments and Methods in Physics Research Section A: Accelerators, Spectrometers, Detectors and Associated Equipment 642 (1) (2011) 78–83.

[17] Y. Kaschuck, B. Esposito, Neutron/γ-ray digital pulse shape discrimination with organic scintillators, Nuclear Instruments and Methods in Physics Research Section A: Accelerators, Spectrometers, Detectors and Associated Equipment 551 (2) (2005) 420–428.

[18] M. Flaska, S. Pozzi, et al., Offline pulse-shape discrimination algorithms for neutron spectrum unfolding, in: Nuclear Science Symposium Conference Record, 2006. IEEE, Vol. 2, IEEE, Piscataway, NJ, USA, 2006, pp. 752–758.

[19] R. T. Schiffer, M. Flaska, S. A. Pozzi, S. Carney, D. D. Wentzloff, A scalable fpga-based digitizing platform for radiation data acquisition, Nuclear Instruments and Methods in Physics Research Section A: Accelerators, Spectrometers, Detectors and Associated Equipment 652 (1) (2011) 491–493.

[20] A. Jančář, Z. Kopeckỳ, J. Dressler, M. Veškrna, Z. Matěj, C. Granja, M. Solar, Pulse-shape discrimination of the new plastic scintillators in neutron–gamma mixed field using fast digitizer card, Radiation Physics and Chemistry 116 (2015) 60–64.

[21] N. Zaitseva, B. L. Rupert, I. Pawełczak, A. Glenn, H. P. Martinez, L. Carman, M. Faust, N. Cherepy, S. Payne, Plastic scintillators with efficient neutron/gamma pulse shape discrimination, Nuclear Instruments and Methods in Physics Research Section A: Accelerators, Spectrometers, Detectors and Associated Equipment 668 (2012) 88–93.

[22] T. J. Hajagos, D. Kishpaugh, Q. Pei, Pulse shape discrimination properties of plastic scintillators incorporating a rationally designed highly soluble and polymerizable derivative of 9,10-diphenylanthracene, Nuclear Instruments and Methods in Physics Research Section A: Accelerators, Spectrometers, Detectors and Associated Equipment 825 (2016) 40–50.

[23] N. Zaitseva, A. Glenn, L. Carman, H. P. Martinez, R. Hatarik, H. Klapper, S. Payne, Scintillation properties of solution-grown trans-stilbene single crystals, Nuclear Instruments and Methods in Physics Research Section A: Accelerators, Spectrometers, Detectors and Associated Equipment 789 (2015) 8–15.

[24] F. D. Brooks, R. W. Pringle, B. L. Funt, Pulse shape discrimination in a plastic scintillator, Nuclear Science, IRE Transactions on 7 (2-3) (1960) 35–38.

[25] G. H. V. Bertrand, M. Hamel, S. Normand, F. Sguerra, Pulse shape discrimination between (fast or thermal) neutrons and gamma rays with plastic scintillators: state of the art, Nuclear Instruments and Methods in Physics Research Section A: Accelerators, Spectrometers, Detectors and Associated Equipment 776 (2015) 114–128.

[26] N. Zaitseva, A. Glenn, L. Carman, R. Hatarik, S. Hamel, M. Faust, B. Schabes, N. Cherepy, S. Payne, Pulse shape discrimination in impure and mixed single-crystal organic scintillators, IEEE Transactions on Nuclear Science 58 (6) (2011) 3411–3420.

[27] E. T. Inc., Ej-299-34, http://www.eljentechnology.com/index.php/products/plastic-scintillators/114-ej-299-33, online; accessed 05-17-2016.

[28] H. P. Martinez, I. Pawelczak, A. M. Glenn, M. L. Carman, N. Zaitseva, S. Payne, Pulse shape discrimination in non-aromatic plastics, Nuclear Instruments and Methods in Physics Research Section A: Accelerators, Spectrometers, Detectors and Associated Equipment 771 (2015) 28–31.

[29] P. Blanc, M. Hamel, C. Dehé-Pittance, L. Rocha, R. B. Pansu, S. Normand, Neutron/gamma pulse shape discrimination in plastic scintillators: Preparation and characterization of various compositions, Nuclear Instruments and Methods in Physics Research Section A: Accelerators, Spectrometers, Detectors and Associated Equipment 750 (2014) 1–11.

[30] P. N. Zhmurin, V. N. Lebedev, V. D. Titskaya, A. F. Adadurov, D. A. Elyseev, V. N. Pereymak, Polystyrene-based scintillator with pulse-shape discrimination capability, Nuclear Instruments and Methods in Physics Research Section A: Accelerators, Spectrometers, Detectors and Associated Equipment 761 (2014) 92–98.

[31] A. L. Vance, N. Mascarenhas, G. O'Bryan, S. Mrowka, Final ldrd report: Advanced plastic scintillators for neutron detection., Tech. rep., Sandia National Laboratories (2010).

[32] Y. Scolnik, G. Shani, Z. B. Alfassi, Scintillation properties of crystalline 9,10-diphenylanthracene: A proof for triplet-triplet annihilation, Nuclear Instruments and Methods in Physics Research Section A: Accelerators, Spectrometers, Detectors and Associated Equipment 254 (2) (1987) 389–392.

[33] E. V. van Loef, K. Markosyan, S. Mukhopadhyay, U. Shirwadkar, N. Zaitseva, S. Payne,

K. S. Shah, Fast-neutron detection and pulse shape discrimination with diphenylanthracene and tetraphenylbutadiene, in: 2011 IEEE Nuclear Science Symposium Conference Record, IEEE, Piscataway, NJ, USA, 2011.

[34] E. V. van Loef, S. Mukhopadhyay, N. Zaitseva, S. Payne, K. S. Shah, Crystal growth and characterization of 9,10-diphenylanthracene, Journal of Crystal Growth 352 (1) (2012) 103–105.

[35] J. Zhang, Z. C. Smith, S. W. Thomas III, Electronic effects of ring fusion and alkyne substitution on acene properties and reactivity, The Journal of organic chemistry 79 (21) (2014) 10081–10093.

[36] R. Young, P. Lovell, Introduction to Polymers, Third Edition, Polymer science, Taylor & Francis, Boca Raton, FL, USA, 2011.

[37] P. Araújo, C. Sayer, R. Giudici, J. Poço, Techniques for reducing residual monomer content in polymers: a review, Polymer Engineering & Science 42 (7) (2002) 1442–1468.

[38] E. J. Bowen, Fluorescence quenching in solution and in the vapour state, Transactions of the Faraday Society 50 (1954) 97–102.

[39] E. J. Bowen, D. W. Tanner, The photochemistry of anthracenes. part 3.inter-relations between fluorescence quenching, dimerization, and photo-oxidation, Transactions of the Faraday Society 51 (1955) 475–481.

[40] J. B. Birks, J. B. Aladekomo, The photo-dimerization and excimer fluorescence of 9-methyl anthracene, Photochemistry and Photobiology 2 (4) (1963) 415–418.

[41] I. B. Berlman, Fluorescence of azulene and 9,10-diphenylanthracene a reply to criticism, Chemical Physics Letters 21 (2) (1973) 344–345.

[42] J. B. Birks, W. A. Little, Photo-fluorescence decay times of organic phosphors, Proceedings of the Physical Society. Section A 66 (10) (1953) 921.

[43] S. Nyibule, E. Henry, W. Schröder, J. Tõke, L. Acosta, L. Auditore, G. Cardella, E. De Filippo, L. Francalanza, S. Gìani, et al., Radioluminescent characteristics of the ej 299-33 plastic scintillator, Nuclear Instruments and Methods in Physics Research Section A: Accelerators, Spectrometers, Detectors and Associated Equipment 728 (2013) 36–39.

[44] J. B. Birks, Energy transfer in organic systems vi. fluorescence response functions and scintillation pulse shapes, Journal of Physics B: Atomic and Molecular Physics 1 (5) (1968) 946.

[45] M. A. Baldo, D. F. O'Brien, Y. You, A. Shoustikov, S. Sibley, M. E. Thompson, S. R. Forrest, Highly efficient phosphorescent emission from organic electroluminescent devices, Nature 395 (6698) (1998) 151–154.

[46] C. Adachi, M. A. Baldo, M. E. Thompson, S. R. Forrest, Nearly 100% internal phosphorescence efficiency in an organic light-emitting device, Journal of Applied Physics 90 (2001) 5048–5051.

[47] B. L. Rupert, N. J. Cherepy, B. W. Sturm, R. D. Sanner, S. A. Payne, Bismuth-loaded plastic scintillators for gamma-ray spectroscopy, EPL (Europhysics Letters) 97 (2) (2012) 22002.

[48] P. L. Feng, J. Villone, K. Hattar, S. Mrowka, B. M. Wong, M. D. Allendorf, F. P. Doty, Spectral- and pulse-shape discrimination in triplet-harvesting plastic scintillators, IEEE Transactions on Nuclear Science 59 (6) (2012) 3312–3319.

[49] E. V. van Loef, P. Feng, G. Markosyan, U. Shirwadkar, P. Doty, K. Shah, Triplet harvesting plastic scintillators with neutron-gamma pulse shape discrimination, in: SPIE Proceedings, Vol. 9213, 2014, pp. 921306–1–921306–9.

[50] C. Adachi, Third-generation organic electroluminescence materials, Japanese Journal of Applied Physics 53 (6) (2014) 060101.

[51] Y. Tao, K. Yuan, T. Chen, P. Xu, H. Li, R. Chen, C. Zheng, L. Zhang, W. Huang, Thermally activated delayed fluorescence materials towards the breakthrough of organoelectronics, Advanced Materials 26 (47) (2014) 7931–7958.

[52] H. Nakanotani, T. Higuchi, T. Furukawa, K. Masui, K. Morimoto, M. Numata, H. Tanaka, Y. Sagara, T. Yasuda, C. Adachi, High-efficiency organic light-emitting diodes with fluorescent emitters, Nature Communications 5.

[53] T. Higuchi, H. Nakanotani, C. Adachi, High-efficiency white organic light-emitting diodes based on a blue thermally activated delayed fluorescent emitter combined with green and red fluorescent emitters, Advanced Materials 27 (12) (2015) 2019–2023.

[54] H. Uoyama, K. Goushi, K. Shizu, H. Nomura, C. Adachi, Highly efficient organic light-emitting diodes from delayed fluorescence, Nature 492 (7428) (2012) 234–238.

[55] I. Berlman, Handbook of Fluorescence Spectra of Aromatic Molecules, 2nd Edition, Academic Press, New York, NY, USA, 1971.

[56] Q. Zhang, J. Li, K. Shizu, S. Huang, S. Hirata, H. Miyazaki, C. Adachi, Design of efficient thermally activated delayed fluorescence materials for pure blue organic light emitting diodes, Journal of the American Chemical Society 134 (36) (2012) 14706–14709.

[57] N. Lin, J. Qiao, L. Duan, L. Wang, Y. Qiu, Molecular understanding of the chemical stability of organic materials for oleds: a comparative study on sulfonyl, phosphine-oxide, and carbonyl-containing host materials, The Journal of Physical Chemistry C 118 (14) (2014) 7569–7578.

[58] Z. Xie, C. Chen, S. Xu, J. Li, Y. Zhang, S. Liu, J. Xu, Z. Chi, White-light emission strategy of a single organic compound with aggregation-induced emission and delayed fluorescence properties, Angewandte Chemie International Edition 54 (24) (2015) 7181–7184.

[59] B. Huang, Q. Qi, W. Jiang, J. Tang, Y. Liu, W. Fan, Z. Yin, F. Shi, X. Ban, H. Xu,

et al., Thermally activated delayed fluorescence materials based on 3, 6-di-tert-butyl-9-((phenylsulfonyl) phenyl)-9h-carbazoles, Dyes and Pigments 111 (2014) 135–144.

[60] S. Wu, M. Aonuma, Q. Zhang, S. Huang, T. Nakagawa, K. Kuwabara, C. Adachi, High-efficiency deep-blue organic light-emitting diodes based on a thermally activated delayed fluorescence emitter, Journal of Materials Chemistry C 2 (3) (2014) 421–424.

[61] Q. Zhang, B. Li, S. Huang, H. Nomura, H. Tanaka, C. Adachi, Efficient blue organic light-emitting diodes employing thermally activated delayed fluorescence, Nature Photonics 8 (4) (2014) 326–332.

[62] M. Liu, Y. Seino, D. Chen, S. Inomata, S.-J. Su, H. Sasabe, J. Kido, Blue thermally activated delayed fluorescence materials based on bis (phenylsulfonyl) benzene derivatives, Chemical Communications 51 (91) (2015) 16353–16356.

[63] M. Ichikawa, T. Tachi, M. Satsuki, S. Suga, T. Koyama, Y. Taniguchi, Gain-narrowing characteristics of fluorescent organic molecules with symmetrical or asymmetrical structures in a neat thin-film optical waveguide, Journal of Photochemistry and Photobiology A: Chemistry 158 (2) (2003) 219–221.

[64] T. Riedl, T. Rabe, H.-H. Johannes, W. Kowalsky, J. Wang, T. Weimann, P. Hinze, B. Nehls, T. Farrell, U. Scherf, Tunable organic thin-film laser pumped by an inorganic violet diode laser, Applied Physics Letters 88 (24) (2006) 241116.

[65] C.-H. Liao, M.-T. Lee, C.-H. Tsai, C. H. Chen, Highly efficient blue organic light-emitting devices incorporating a composite hole transport layer, Applied Physics Letters 86 (20) (2005) 203507.

[66] W. Cai, Q. Chen, N. Cherepy, A. Dooraghi, D. Kishpaugh, A. Chatziioannou, S. Payne, W. Xiang, Q. Pei, Synthesis of bulk-size transparent gadolinium oxide–polymer nanocomposites for gamma ray spectroscopy, Journal of Materials Chemistry C 1 (10) (2013) 1970–1976.

[67] C. Liu, T. J. Hajagos, D. Kishpaugh, Y. Jin, W. Hu, Q. Chen, Q. Pei, Facile single-precursor synthesis and surface modification of hafnium oxide nanoparticles for nanocomposite γ-ray scintillators, Advanced Functional Materials 25 (29) (2015) 4607–4616.

[68] Y. Chen, C. Liu, Y. Jin, T. J. Hajagos, D. Kishpaugh, Q. Zhuang, Q. Pei, Ytterbium fluoride loaded plastic scintillators for γ-ray spectroscopy, in: SPIE Optical Engineering+ Applications, International Society for Optics and Photonics, 2016, pp. 99680N–99680N.

[69] L. J. Basile, Characteristics of plastic scintillators, The Journal of Chemical Physics 27 (3) (1957) 801–806.

[70] L. J. Basile, Effect of styrene monomer on the fluorescence properties of polystyrene, The Journal of Chemical Physics 36 (8) (1962) 2204–2210.

[71] F. Hirayama, L. Basile, C. Klkuchi, Energy transfer and quenching in plastic scintillators, Molecular Crystals 4 (1-4) (1968) 83–108.

[72] T. King, R. Voltz, The time dependence of scintillation intensity in aromatic materials, in: Proceedings of the Royal Society of London A: Mathematical, Physical and Engineering Sciences, Vol. 289, The Royal Society, 1966, pp. 424–439.

[73] J. S. Armstrong, Long-range forecasting, Wiley New York ETC., 1985.

[74] S. Makridakis, Accuracy measures: theoretical and practical concerns, International Journal of Forecasting 9 (4) (1993) 527–529.